New approaches to reduce friction in turbulent pipe flow

by

Davide Scarselli

January, 2020

A thesis presented to the
Graduate School
of the
Institute of Science and Technology Austria, Klosterneuburg, Austria
in partial fulfillment of the requirements
for the degree of
Doctor of Philosophy

I|S|T AUSTRIA

Institute of Science and Technology

The thesis of Davide Scarselli, titled *New approaches to reduce friction in turbulent pipe flow*, is approved by:

Supervisor: Prof. Björn Hof, IST Austria, Klosterneuburg, Austria

Signature: _____

Committee Member: Prof. Maurizio Quadrio, Politecnico di Milano, Milano, Italy

Signature: _____

Committee Member: Prof. Hendrik Kuhlmann, TU Wien, Wien, Austria

Signature: _____

Defense Chair: Prof. Christopher John Wojtan, IST Austria, Klosterneuburg, Austria

Signature: _____

signed page is on file

I hereby declare that this thesis is my own work and that it does not contain other people's work without this being so stated; this thesis does not contain my previous work without this being stated, and the bibliography contains all the literature that I used in writing the dissertation.

I declare that this is a true copy of my thesis, including any final revisions, as approved by my thesis committee, and that this thesis has not been submitted for a higher degree to any other university or institution.

I certify that any republication of materials presented in this thesis has been approved by the relevant publishers and co–authors.

Signature: _____

Davide Scarselli

January, 2020

signed page is on file

Abstract

Many flows encountered in nature and applications are characterized by a chaotic motion known as turbulence. Turbulent flows generate intense friction with pipe walls and are responsible for considerable amounts of energy losses at world scale. The nature of turbulent friction and techniques aimed at reducing it have been subject of extensive research over the last century, but no definite answer has been found yet. In this thesis we show that in pipes at moderate turbulent Reynolds numbers friction is better described by the power law first introduced by Blasius and not by the Prandtl–von Kármán formula. At higher Reynolds numbers, large scale motions gradually become more important in the flow and can be related to the change in scaling of friction. Next, we present a series of new techniques that can relaminarize turbulence by suppressing a key mechanism that regenerates it at walls, the lift–up effect. In addition, we investigate the process of turbulence decay in several experiments and discuss the drag reduction potential. Finally, we examine the behavior of friction under pulsating conditions inspired by the human heart cycle and we show that under such circumstances turbulent friction can be reduced to produce energy savings.

Acknowledgments

First and foremost, I would like to express my sincere gratitude to my supervisor Prof. Björn Hof for his wise guidance, patience and for teaching me what it means to be a scientist. I am really grateful that I had the chance to work with him creatively to push forward the boundaries of knowledge.

I would like to extend my thanks to the members of my thesis committee, Prof. Maurizio Quadrio and Prof. Hendrik Kuhlmann for the encouragement, solid advice and constructive criticism to my research.

Without the support of the entire Hof Group here at IST Austria my work might have probably never seen light. Special thanks to Dr. Jakob Kühnen for his teachings and the fruitful collaboration, to Dr. George Choueiri, Dr. Grégoire Lemoult, Dr. Vasudevan Mukund and Dr. Nazmi Burak Budanur for the many stimulating discussions, and to Dr. José Lopez, Dr. Atul Varshney, Markus Schaner, Michael Riedl, Dr. Balachandra Suri, Nishchal Agrawal and Dr. Łukasz Klotz for their precious inputs and help.

I am particularly indebted to our former group technician Philipp Maier and the people of the Machine Shop, especially Dr. Todor Asenov and Astrit Arslani, for their outstanding support and patience. Many experiments would have been impossible without their passionate dedication and expertise.

Last but not least, I owe a huge debt of gratitude to Linda Seghezzi, my father Claudio Scarselli and my mother Anna Maria Algisi, my brothers Diego Scarselli and Dario Scarselli. Their sincere belief in me and unwavering emotional support gave me the strength and the courage to pursue my goals till the end.

About the Author

Davide Scarselli earned a MSc in Aeronautical Engineering at Politecnico di Milano in 2013 with a major in aerodynamics. He later collaborated with the Department of Aerospace Engineering at Politecnico di Milano as research assistant in a project where he developed and tested a shape memory alloy actuator for flow control. He joined IST Austria in 2015 for an internship and then as graduate student. His research focuses mainly on turbulent flows in pipes and the development of strategies to reduce turbulent friction. He tested experimentally numerous devices to control turbulence and theoretically interpreted the results. He presented his work at the APS–DFD meeting in 2016 and 2019, at EFMC in 2018 and at GAMM in 2019. His research has been published among others in Nature Physics and the Journal of Fluid Mechanics.

List of Publications

1. J. Kühnen, B. Song, D. Scarselli, N. B. Budanur, M. Riedl, A. P. Willis, M. Avila, and B. Hof 2018. Destabilizing turbulence in pipe flow. *Nature Physics*, 14(4):386–390

2. J. Kühnen, D. Scarselli, M. Schaner and B. Hof 2018. Relaminarization by steady modification of the streamwise velocity profile in a pipe. *Flow, Turbulence and Combustion*, 100(4):919–943

3. D. Scarselli, J. Kühnen and B. Hof 2019. Relaminarising pipe flow by wall movement. *Journal of Fluid Mechanics*, 867:934–948

4. J. Kühnen, D. Scarselli and B. Hof 2019. Relaminarization of pipe flow by means of 3D–printed shaped honeycombs. *Journal of Fluids Engineering*. 141(11):111105

Table of Contents

List of Tables

List of Figures

1   Introduction

Turbulent flows are characterized by a highly disordered eddying motion, as opposed to the ordered and streamlined state of laminar flows. Turbulence is ubiquitous in flows in nature, such as rivers, clouds and the blood flow through arteries, as well in industrial applications with examples ranging from oil pipelines to hydraulic circuits for heat exchange. Turbulence sets in spontaneously at sufficiently high flow speeds when the fluid's inertia outweighs the viscous forces and it is associated with higher energetic losses and mixing with respect to laminar flow conditions. Since the first systematic experimental investigation of turbulence in pipes performed by Reynolds in 1883, the physical mechanisms governing the chaotic motion and ways to suppress turbulence have been subject of extensive research. Despite the efforts, a thorough understanding of turbulent phenomena remains elusive and a number of questions still remain unanswered.

Flows through pipes belong to the broad class of wall–bounded flows, which for example comprises flows in ducts, over ship hulls and aerodynamic bodies. In this setting the flow velocity vanishes in the proximity of an impenetrable surface, independently of the intensity of the flow current elsewhere. Thus, intense velocity gradients are generated and hence a strong shear stress due to viscosity. This results in a net force on the fluid which opposes to the fluid motion, typically referred to as friction or drag. Contrary to the laminar flow, turbulent whorls greatly enhance the momentum transfer between fluid layers leading to much steeper velocity gradients and friction. To put this in perspective, in moderately turbulent flows such as those found in household water pipelines, turbulence accounts for approximately 90% of the pressure losses induced by friction. On a industrial scale, turbulence is responsible for 99% of the losses in oil pipelines and roughly 50% of the total

drag found in a commercial airliner [Gad-el-Hak, 1994]. In addition, it has been estimated that 20% of the world electricity demand is utilized by pumping systems to overcome turbulent drag [Frenning, 2001]. The lack of understanding of the physical processes which determine turbulent friction and finding ways to reduce it have driven fluid mechanics research from the beginning and still remain an open problem despite several decades of research. Nowadays more than ever, controlling turbulence would have profound implications not only on a global economical scale, but more importantly on the ever growing human footprint on the environment.

In this work we consider the fluid motion through a pipe of cylindrical cross section with straight and smooth walls, typically referred to as pipe flow. The geometry is representative of several applications and due to its simplicity can be investigated theoretically, experimentally and numerically. For future reference, we denote with D and L the pipe diameter and length. The medium is a Newtonian fluid characterized by a kinematic viscosity ν and density ρ. Using the mean velocity U_m, the Reynolds number is defined as $Re = U_m D / \nu$.

1.1   The scaling of turbulent friction

The nature of turbulent friction has been a major subject of study since the origins of fluid mechanics in the late 19th century. Numerous investigations of flow resistance in pipes were already available when Blasius first proposed a scaling law for friction [Blasius, 1913; Bodenschatz and Eckert, 2011]. The novelty consisted in reducing all the available data to Re and the Darcy–Weisbach friction factor $f = 2\Delta p D / (\rho U_m^2 L)$, where Δp is the pressure drop across the considered pipe length. Multiple data sets were found to collapse in these units and an empirical power law emerged, $f = 0.316 Re^{-1/4}$ for $3000 \lesssim Re \lesssim 100\,000$. Starting from 1926, a newer data set at higher flow rates was progressively made available (the full dataset was published later by Nikuradse [1933]) and it made it clear that the empirical scaling suggested by Blasius was inappropriate at larger Re. In parallel, the seminal work of Prandtl and von Kármán was laying the basis for understanding turbulent velocity profiles, culminating with the derivation of the well known logarithmic velocity profile and

universal friction formula for smooth pipes, $f^{-\frac{1}{2}} = 2.0 \log_{10}(Re f^{\frac{1}{2}}) - 0.8$ [Kármán, von, 1930].

Although over the years a few arguments have been advanced against the Prandtl–von Kármán model [Barenblatt, 1993; Barenblatt and Prostokishin, 1993], the logarithmic velocity profile and friction law have enjoyed widespread consensus among the community and have been extensively validated at increasingly higher Re (currently up to $Re \approx 4 \cdot 10^7$), with only minor adjustments to the constants [Zagarola and Smits, 1998; Swanson *et al.*, 2002; Furuichi *et al.*, 2015]. Recently, it has also been shown that the constants are universal and do not depend on the specific flow geometry, when the effects of the pressure gradient are taken into account [Luchini, 2017]. However, little to no attention has been dedicated to the Blasius regime, often considered only as a local empirical fit of the true friction law [Kármán, von, 1930; McKeon *et al.*, 2005]. The work presented in Chapter 2 aims to clarify this issue by investigating accurately friction up to $Re = 140\,000$. Experiments are carried out to measure precisely f in tightly controlled conditions. A feedback driven syringe pump is used to maintain a constant mass flux condition, while water temperature oscillations are compensated for by a heat exchanger. Results show that f is indeed consistent with a power law up to $Re \approx 70\,000$ and in this regime deviates from the Prandtl–von Kármán scaling. In addition, the results are confirmed by highly resolved direct numerical simulations up to $Re = 100\,000$. A rationale for the $-1/4$ exponent has been already advanced [Gioia and Chakraborty, 2006], however we here show a simpler argument based on the balance between mean turbulent kinetic energy production and viscous dissipation rate and further support it with numerical evidence.

To uncover the physical mechanism responsible for the deviation of f from the power law scaling, we focus on how turbulence features evolve as Re grows. At low and moderate Re ($3000 \lesssim Re \lesssim 60\,000$), turbulent kinetic energy is produced in a well defined region in the proximity of the wall, the inner peak. Here, turbulent structures are continuously regenerated by the intense velocity shear [Hamilton *et al.*, 1995; Jiménez and Pinelli, 1999]. Patches of low velocity fluid adjacent to the wall and elongated along the pipe axis (normally referred to as low–speed streaks) undergo

an instability and generate streamwise oriented vortices via non–linear interaction. In turn, these vortices eject fluid away from the wall and create new low–speed streaks. The flow structures (commonly known as small scale motions, or SSM) involved in the turbulence regeneration cycle are relatively short and scale in viscous units $\delta_\nu = \nu / \sqrt{\tau_w / \rho}$, where τ_w is the mean wall shear stress. At higher Re, the flow undergoes a structural transition as turbulence is generated additionally further away from the wall and it is associated with long streamwise wavelengths, the so called large scale motions (LSM) [Kim and Adrian, 1999; Hutchins and Marusic, 2007b; Monty *et al.*, 2007; Smits *et al.*, 2011]. These long structures can be several pipe diameters long and consist of regions of low or high flow momentum that can meander azimuthally. Differently from the structures found in the inner peak, the LSM do not scale in viscous units and their extent grows with Re. In Chapter 2, a new analysis of turbulent friction is proposed, where the contribution of the LSM to f is separated from the one of the SSM. By using data from direct numerical simulations (DNS), it is shown that at $Re \approx 70\,000$ the friction contribution of the LSM surpasses the one of the SSM. Surprisingly, the near wall turbulence regeneration cycle assumes a more and more marginal role in determining friction when Re grows large. To further support the findings, it is also shown how large departures of f from the Blasius scaling correlate with the velocity fluctuations characterizing the LSM.

1.2   Flow relaminarization

Although flows in pipes at sufficiently high Re are virtually always turbulent, laminar conditions are also possible. The laminar Hagen–Poiseuille flow has been verified to be linearly stable, *i.e.* stable with respect to infinitesimal perturbations, up to $Re = 10^7$ [Meseguer and Trefethen, 2003]. However, finite amplitude perturbations can give rise to statistically self–sustained localized turbulence from $Re = 2040$ [Avila *et al.*, 2011] and fully turbulent conditions from $Re \approx 3000$ [Avila and Hof, 2013; Barkley *et al.*, 2015]. Laminar conditions thus need in practice straight and smooth pipes with a carefully designed inlet. As both the laminar and turbulent state can coexist at the

same Re, it is only natural to wonder whether it is possible to revert a fully turbulent flow into a laminar one, a process known as relaminarization. The process is believed to be non–spontaneous and requires some form of control. Relaminarization has been reported at low Re after a sudden duct expansion [Sibulkin, 1962; Narayanan, 1968; Sreenivasan, 1982; Selvam *et al.*, 2015], or in flows subjected to strong curvature or heating [Sreenivasan, 1982], peristaltic waves [Nakanishi *et al.*, 2012] or wall transpiration controlled in feedback [Bewley *et al.*, 2001].

A novel strategy for relaminarization has been demonstrated in simulations and experiments for spatially intermittent turbulence ($2000 \lesssim Re \lesssim 3000$) [Hof *et al.*, 2010]. A strong perturbation is introduced at a fixed spatial position to disturb the laminar flow trailing an upcoming turbulent spot. As a result, the mean axial velocity profile of the trailing edge of the turbulent spot is flattened and the turbulence downstream decays. The method is suspected to work by interfering with the streak–vortex cycle. The mechanism, commonly known as lift–up, relies on the velocity shear dU/dy to couple wall–normal velocity fluctuations v with streamwise ones u, namely $u(t) \propto v \, dU/dy \, t$ [Ellingsen and Palm, 1975; Landahl, 1975; Schmid and Henningson, 2001; Brandt, 2014]. In the absence of shear ($dU/dy = 0$, flattened velocity profile) the lift–up breaks down and turbulence regeneration is interrupted.

The idea of suppressing turbulence by disrupting the turbulence regeneration cycle is successfully extended to a fully turbulent flow in Chapter 3. Here, it is shown in DNS and experiments how a flatter, plug–like velocity profile can initiate a complete collapse of turbulence, eventually leading to a laminar flow and energy savings. To achieve such a profile modification, we add an appropriate radially dependent body force term to the equation of motion in our numerical simulations. In the experiments, we employ four different active techniques. In the first technique four coplanar rotors are used to stir a turbulent flow and induce a momentum redistribution that ultimately flattens the profile. The second and third techniques respectively employ radial and streamwise oriented jets to deform the velocity profile. In the last approach a movable pipe segment is used to locally accelerate the flow at the wall to impose a plug profile. In all cases turbulence is shown to decay

and the flow eventually relaminarizes completely.

We proceed further and test whether the physical mechanism responsible for turbulence decay proposed in Hof *et al.* [2010] applies also to fully turbulent flow. As mentioned before, turbulence is regenerated continuously in the streak–vortex cycle. During the lift–up phase, streamwise vortices induce low–speed streaks that later undergo an instability and in turn regenerate new vortices. Key to the success of the mechanism is the presence of a velocity shear that couples wall–normal and streamwise velocity perturbations. While the process is purely inviscid, the flow viscosity determines the intensity of the effect. In order to quantify the lift–up, transient growth (TG) is used as proxy. TG measures the maximum possible amplification of the kinetic energy of infinitesimal perturbations applied to a base flow [Schmid and Henningson, 2001; Meseguer and Trefethen, 2003; Brandt, 2014]. Normally, TG is computed using a laminar base flow to determine its stability properties. In the context of turbulent flows, the axial mean velocity profile has been used in plane channel flow as base flow to estimate the spanwise separation between low–speed streaks [Butler and Farrell, 1993; del Álamo and Jiménez, 2006; Pujals *et al.*, 2009]. In the experiments described in Chapter 3 it is shown how the flattened velocity profiles of relaminarizing flows possess a much lower TG (and hence lift–up potential) with respect to the uncontrolled flow. Moreover, a theoretical level for self–sustaining turbulence is identified in simulations and it is shown to be consistent with the experiments.

A complete relaminarization offers a great potential for energy savings. At $Re \approx 20\,000$ the laminar friction is only about one tenth of the turbulent one and rapidly becomes much smaller. However, an external energy input is required to force the velocity profile, and trigger turbulence decay. This aspect is also considered in Chapter 3 by evaluating the net energy savings associated with the two laminarization devices that utilize jets to control the flow. To this end, the kinetic energy of the injected flow rate is evaluated and subtracted from the one saved by the laminar flow. When the actual parameters of the set–up are used, the energy savings are estimated to be $\approx 31\%$ for the wall–normal jets at $Re = 3100$ and $\approx 55\%$ for the streamwise injection at $Re = 5000$.

Chapter 4 investigates more in detail the features and properties of the flow during the process of relaminarization. In addition to the streamwise injection device introduced in Chapter 3, a new turbulence control device that does not require an external energy input is presented. The new method operates by slowing down the flow in the core of the pipe by means of a perforated obstacle disc and at the same time bypassing part of the flow through an annular region close to the wall. When the two streams meet downstream of the device, an unusually flat velocity profile is generated and turbulence collapses up to $Re = 3800$.

Stereoscopic particle-image velocimetry (PIV) is used to characterize the evolution of the flow during the relaminarization. Fluctuations levels comparable to the ones found in the uncontrolled flow are found at distances as close as two diameters to the control device. Nevertheless, the flatter velocity profile evolves gradually into the parabolic laminar solution, and the residual perturbations quickly decay exponentially. At higher Re the flow develops towards laminar for about $30D$, and then residual fluctuations trigger transition to turbulence. However, pressure drop measurements over the initial relaminarizing region show still a moderate drag reduction ($\approx 15\%$ at $Re = 11\,000$).

Chapter 5 elaborates further the technique of the moving wall presented in Chapter 3 and explores in detail the exact circumstances and conditions that lead to a full turbulence collapse. The study is motivated by the remarkable simplicity and performance of the method, as it was shown to relaminarize the flow up to $Re = 40\,000$. Here, a layer of fluid close to the wall is rapidly accelerated by means of a movable pipe segment. After the wall stops, the velocity profile is flat and the flow relaminarizes. The control method shows similarities with other drag reduction studies that employ superhydrophobic surfaces to generate a slip boundary condition [Watanabe *et al.*, 1999; Ou and Rothstein, 2005; Daniello *et al.*, 2009; Saranadhi *et al.*, 2016]. However, while typically the slip velocity induced by water repellent surfaces is only a fraction of the mean velocity, the wall shift speed necessary to flatten the velocity profile can be comparable to or larger than the mean flow velocity.

For a wide range of Re ($5000 < Re < 22\,000$), the wall shift length and velocity

are systematically varied to find the optimal conditions that lead to turbulence decay. When the wall velocity is held constant (usually equal to the mean or centerline velocity), a linear dependence between Re and the minimum shift required for relaminarization is found. A simple dimensional analysis argument is given to show that the linear scaling follows from the gradual viscous diffusion of the slip boundary conditions into the flow.

The temporal evolution of the relaminarization is also revisited in the lights of the transient growth argument given in Chapter 3. Planar PIV measurements are used to monitor the flow during the actuation and afterwards. As the profile becomes flatter while the wall is shifted, TG drastically reduces by more than one order of magnitude. At the same time, wall–normal fluctuations comparable to the undisturbed flow are still present. The unusually flat profile has a severely reduced lift–up potential and remaining disturbances decay exponentially while the flow becomes laminar. Moreover, it is found that the relaminarizing flow closely resembles a laminar flow developing from a pipe entrance.

The experimental strategies discussed in Chapters 3, 4 and 5 require either a rather complicated actuation mechanism (rotors, wall motion, flow injection) or perform only modestly (passive obstacle, up to $Re = 3800$). Chapter 6 addresses the problem and focuses on designing a passive device with improved relaminarization performance and at the same time assesses the energetic impact of such device. A series of 3D–printed honeycomb–shaped obstacles is developed to flatten the velocity profile and hence suppress turbulence. The idea of conditioning the flow with honeycombs is not new. Together with meshes and screens, honeycombs have been used to control turbulence levels by suppressing cross–stream fluctuations [Lumley and McMahon, 1967; Loehrke and Nagib, 1976; Mikhailova *et al.*, 1994; Groth and Johansson, 1988] or to create surrogates of free shear flows in wind tunnels [Kotansky, 1966; Karnik and Tavoularis, 1987; Ahmed and Lee, 1997]. However, honeycombs are here used with the primary purpose of flattening the mean velocity profile to reduce the lift–up and suppress turbulence. A shape optimization process is used to increase the relaminarization capability of the honeycombs up to $Re = 9600$. Chapter 6 investigates also the energetic cost of the control. While the laminar

friction factor is much lower than the turbulent one, the presence of an obstacle also introduces a concentrated pressure loss. Depending on how long the flow downstream the control is held laminar, the energetic gain can change. The efficiency of the honeycombs is then measured in the minimum pipe length necessary to achieve an energetic break–even, provided that the pipe is sufficiently smooth and straight to avoid transition to turbulence.

1.3   Techniques for drag reduction

The drag reduction potential offered by laminarized flows is large and increases sensibly with Re. Despite the intrinsic advantage offered, laminar flows are highly susceptible to disturbances that can revert back to the turbulent state. The fact is aggravated at higher Re, when the flow becomes even more sensitive [Hof $et\ al.$, 2003; Durst and Ünsal, 2006; Nishi $et\ al.$, 2008]. In practice, surface roughness, thermal gradients or geometric imperfections in the pipeline are sufficient to trigger turbulence at large flow rates.

During the last decades numerous solutions to reduce turbulent drag have been explored both numerically and experimentally. While these techniques do not necessarily aim at relaminarizing the flow, they seek alternative control strategies which can reduce the amount of turbulent friction. Passive techniques aim at interfering with the turbulence production without an energy input. An important class of techniques is represented by fluid additives such as polymers and surfactants which work by altering the rheological properties of the medium [Zakin $et\ al.$, 1998; Hellsten, 2002; Virk $et\ al.$, 1970; White and Mungal, 2008; Choueiri $et\ al.$, 2018]. The additives typically respond to the flow's shear viscous–elastically and interfere with streamwise vortices near the wall. Additives offer a good drag reduction potential (for polymers, 80% at $Re = 100\,000$). However, they are expensive and need constant replacement because of degradation and in addition, they alter the chemical properties of the medium. An alternative to fluid additives consists in confining the control mechanism to the wall, in the form of passive textured surfaces. These can have the form of flow–aligned grooves, small regular protrusions, structured

roughness or bio–inspired surfaces and are designed to hamper the turbulence regeneration cycle [Walsh, 1983; Sirovich and Karlsson, 1997; Bechert *et al.*, 2000; Peet *et al.*, 2008; Dean and Bhushan, 2010; Garcia-Mayoral and Jiménez, 2011]. While these techniques are attractive for their simplicity, they only offer a mild drag reduction (at most $\approx 10\%$) and are not suitable for internal flows in ducts as they suffer from surface degradation due to corrosion or dirt deposition.

Active strategies require an external energy input and allow for a much larger variety of control options. On the one hand, closed–loop control of turbulence has been shown in numerical simulations to completely suppress turbulence [Bewley *et al.*, 2001; Brunton and Noack, 2015], however, very little progress has been made in experiments because of practical limitations in the physical dimension and number of sensors and actuators [Kasagi *et al.*, 2009b]. On the other hand, open–loop control is based on simpler actuation schemes where the control has the form of a spatial or temporal forcing at the wall. Several strategies have been tested, such as spanwise wall oscillations and traveling waves [Jung *et al.*, 1992; Karniadakis and Choi, 2003; Quadrio *et al.*, 2009; Quadrio, 2011], traveling waves of wall blowing and suction [Min *et al.*, 2006; Hœpffner and Fukagata, 2009] and peristaltic waves [Nakanishi *et al.*, 2012]. These methods typically work by interfering with the turbulence regeneration cycle (spanwise oscillations) or by directly acting on turbulent stresses (blowing and suction, wall–normal deformation). Such techniques show moderate energy saving potentials and in some cases have also been validated by experiments [Auteri *et al.*, 2010]. However, the practical implementation of a distributed wall actuation poses serious challenges. Realizing a continuous wall deformation would require several actuators distributed along the duct length and operating continuously. Besides the technological shortcomings, manufacturing and maintenance costs can quickly erode the energy savings granted by such techniques.

In spite of decades of research aimed at reducing turbulent friction, only few techniques have been validated experimentally and even fewer implemented in real applications. Examples of the latter include the usage of dilute polymers in the Trans Alaska Pipeline [Burger *et al.*, 1982] and riblets covering the hull of a sail boat in the 1987 America's Cup [Vukoslavcevic *et al.*, 1992]. High costs and technological

limitations prevent widespread usage of known drag reduction methods and motivate the need for a radically new approach to the problem.

1.4   Drag reduction in pulsating flows

Chapter 7 presents a novel approach to drag reduction based on a specific pulsating modulation of the flow rate which can perturb turbulence and reduce the average friction. The technique is inspired by the pulsating conditions that are encountered in the human circulatory system, where Re can reach values well beyond transition (in the aorta max $Re \approx 4000$, [Bürk *et al.*, 2012]). As high shear levels associated with turbulence can potentially damage the inner cell layer of arteries [Davies *et al.*, 1986; DePaola *et al.*, 1992; Davies, 2009; Gimbrone and García–Cardeña, 2016], the study begins by testing the response of perturbations under pulsating conditions. For a pumping cycle modeled after the human heart, it is found that fluctuations are short lived and the flow appears laminar even when the flow reaches the maximum speed. If the same experiment is performed with a cycle lacking the diastolic phase (a period during which the minimum flow rate is held constant), the perturbations instead evolve in self–sustaining localized turbulence structures.

This simple experiment shows that in unsteady conditions, Re alone does not determine the ultimate fate of flow disturbances. The form of the pulsation plays an equivalently important role. The study takes the idea further and applies a periodic modulation of the flow rate to a fully turbulent flow ($Re > 3200$ at all times). The role of mean speed acceleration and deceleration in turbulent flows has been extensively studied over the last two decades with experiments and numerical simulations [He and Jackson, 2000; Greenblatt and Moss, 2004; Ariyaratne *et al.*, 2010; He and Seddighi, 2013; He *et al.*, 2016a; Mathur *et al.*, 2018]. These studies consider a steady turbulent flow subjected to a linear increase or decrease of flow rate and assess how turbulence reacts by analyzing flow statistics. Findings show how acceleration can induce a delayed response in the turbulence kinetic energy production and redistribution. At the same time the wall shear stress τ_w first briefly increases and then decreases with respect to the quasi–steady value. Conversely, the delayed

response in decelerating flows induces higher turbulent fluctuations and friction with respect to the quasi–steady value.

The idea of investigating the average drag of a pulsating flow is not new. Mao and Hanratty [1986] conducted one of the first experimental investigations of wall shear stress under turbulent sinusoidal conditions and showed no substantial change in drag for the parameters investigated. Experimental evidence for drag reduction has been shown in pulsating pipe flow under certain conditions in the so called wave dominated regime [Lodahl *et al.*, 1998]. In such flows the oscillatory part is greater or equal than the steady component and a complete flow reversal occurs. Moreover, a more recent numerical study showed that the average pumping power associated with these flows is larger than the steady flow alone, even in presence of drag reduction [Manna *et al.*, 2012].

Combining intuition from the heart cycle experiment and the potential friction reduction observed during flow acceleration, Chapter 7 investigates experimentally and numerically the response of a turbulent flow to a pulsating control, with Re oscillating between 3200 and 18 800. While τ_w is observed to reduce temporary during flow acceleration, overall the average drag associated to the cycle is larger than one found under steady conditions (here Re is held constant and equal to the mean Re of the cycle). When a rest phase analogous to the heart diastole is instead inserted after the flow deceleration, τ_w drops to considerably lower levels during the subsequent increase of Re. As a results, the modified cycle is found to reduce drag by 27% and energy losses by 8% with respect to steady conditions. Finally, a parametric study is performed to assess the effects of different accelerations rates and rest phase durations. The results show that a shorter, more intense increase of Re can generate larger savings, while the rest phase must be selected optimally to avoid energy losses.

2 Large scale motions and friction scaling in pipes

Turbulence dictates the frictional drag at high velocities; this applies to flows through pipes and ducts just as it does to flows around vehicles. In all these situations, the standard procedure to determine skin friction is to resort to the "law of the wall" [Kármán, von, 1930; Prandtl, 1932], which infers a logarithmic dependence on the Reynolds number Re. Here we show that starting from turbulence at onset and for over a decade in Re, friction does not comply with standard theory but instead follows a power law (the Blasius relation). The eventual break down of the power law and the approach to the logarithm is caused by a structural transition of turbulence. As shown, this transition is dominated by streamwise elongated streaks, *i.e.* large scale motions, which appear close to the wall and subsequently dominate turbulent drag.

J. Lopez, D. Scarselli, B. Suri and B. Hof. Manuscript in preparation for submission.

2.1   Letter

Fluids adhere to surfaces and relative motion results in velocity gradients and friction. In turbulent flow, the adjustment between the zero velocity at the boundary and the free–stream velocity of the fluid takes place across a thin layer. This sharp adjustment in flow speed results in a substantial drag force opposing the fluid motion. Lacking an analytical expression for turbulent mean velocity profiles, estimates of these friction losses rely on semi–empirical models and experiments. Based on an analysis of experimental data, Blasius proposed that the friction factor, f, for smooth pipes, depends on the Reynolds number following a power law with an exponent of $-1/4$ (the Reynolds number is defined as $Re = U(2R)/\nu$, where U is the mean velocity, R the pipe radius and ν is the fluid's kinematic viscosity) [Blasius, 1913]. However, more extensive experiments showed that this simple scaling failed for $Re \gtrsim 100\,000$ (see Fig. 2.1 (a) for state of the art experiments on friction factor scaling). In part based on these observations, von Kármán and Prandtl proposed the so called law of the wall, where the mean turbulent velocity profile varies logarithmically with the distance from the solid boundary [Kármán, von, 1930; Prandtl, 1932]. Integrating this velocity profile over the a pipe section yields a logarithmic dependence of f on Re. For appropriate fit parameters, this logarithmic relation was found to be in agreement with all available data, small and large Re. The seeming power law dependence at low Re consequently was considered a local approximation to the true logarithmic law [Kármán, von, 1930]. Since then, numerous studies have been carried out trying to establish universality at high Re (see e.g. [Luchini, 2017]), but much less attention has been paid to the scaling of f at lower Re. While a number of studies noted that for $Re < 100\,000$ the logarithm appears less accurate than the Blasius scaling, *e.g.* [Yakhot *et al.*, 2010], the available data are inconclusive (see Fig. 2.1 (b)). Starting from the lowest Re where pipe flow is fully turbulent ($Re > 3000$), we show that f precisely follows a power law as Re increases. At intermediate Re ($Re \approx 65\,000$) large scale motions enter the logarithmic layer, elevate friction levels and lead to a slower (logarithmic) decrease of the friction factor with Re.
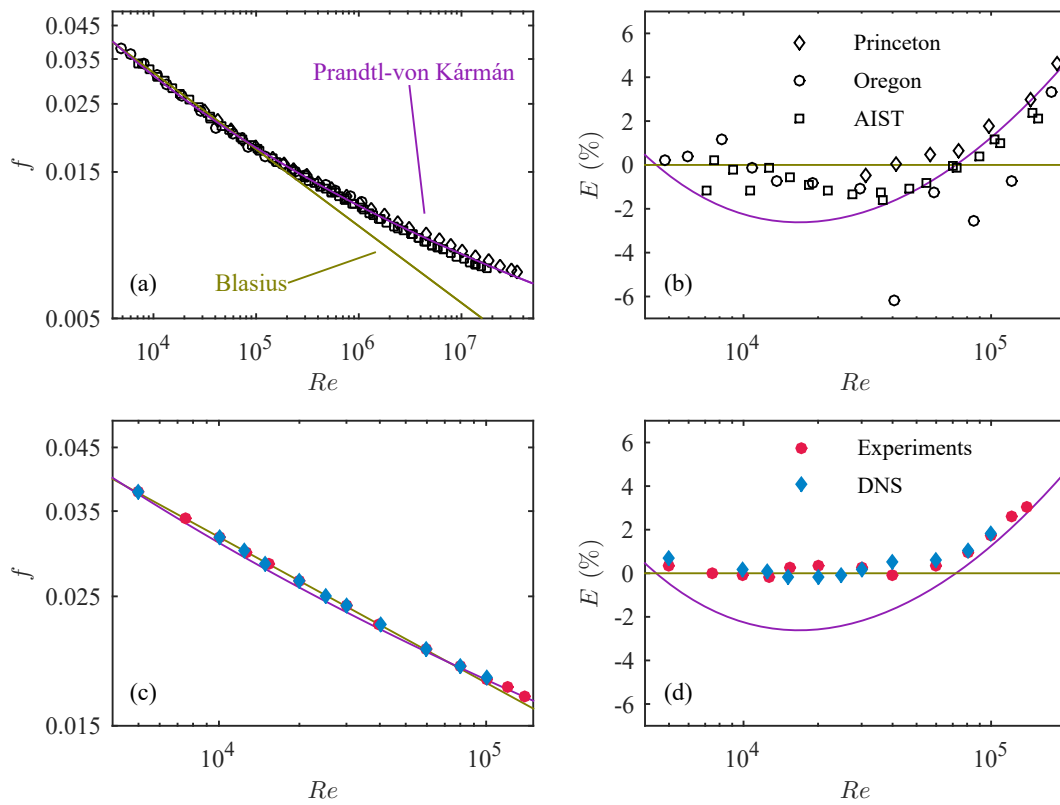
Figure 2.1: Darcy–Weisbach friction factor f as a function of the Reynolds number Re. The green and purple lines correspond to friction factors calculated using the Blasius correlation ($f = 0.316Re^{-0.25}$) and the Prandtl–von Kármán formula ($1/\sqrt{f} = 2\log_{10}(Re\sqrt{f}) - 0.8$), respectively. (a) Data collection of recent pipe flow experiments [Furuichi *et al.*, 2015; Zagarola and Smits, 1998; Swanson *et al.*, 2002] (b) Relative error $E = (f - f_{\text{Blasius}})/f_{\text{Blasius}}$ between friction factors in (a) and those calculated using the Blasius correlation. (c) Friction factors measured (computed) in our experiments (simulations) (d) Same as in (b) for the data in (c).

Experiments were carried out in a pipe of circular cross section with an inner diameter of 10 ± 0.01 mm and a total length of $720R$. Turbulence is triggered at the entrance and left to develop over the first $240R$. Pressure drop measurements are then carried out over the subsequent $240R$. By precise control of the water flow rate, its temperature and careful calibration of the pressure sensors, an accuracy of $\pm 0.2\%$ and $\pm 0.4\%$ on Re and f, respectively, has been achieved (see details in Supplementary Information, Section 2.2.1). As shown in Figs. 2.1 (c) and (d) (circles), up to $Re \approx 65\,000$ the measured friction factors clearly deviate from the Prandtl–von Kármán law and instead follow the Blasius law.

To verify these measurements, direct numerical simulations of the Navier Stokes equations (DNS) were carried out. These were performed using a highly scalable solver based on the open source software *openPipeFlow* [Willis, 2017] and *NSCouette* [Shi *et al.*, 2015]. Pipes larger than $10R$ in the streamwise direction were used to minimize periodicity effects and capture large scale features. Pipe sizes and spatial resolution were increased until the friction factor values were found to converge (further details about the code and the simulations are given in Supplementary Information, Section 2.2.2). As seen in Figs. 2.1 (c) and (d), the average friction factors obtained in the simulations are in excellent agreement with those measured in the experiments. Also here, friction factors up to $Re \approx 65\,000$ clearly deviate from the presumed more accurate Prandtl–von Kármán theory and instead they precisely follow the Blasius relation.

It is noteworthy that the associated $-1/4$ exponent arises from a dimensional analysis of the turbulent kinetic energy balance. As shown in Supplementary Information, Section 2.2.3, the validity of the power law however hinges on a proportionality between the shear stress and the ratio of the mean velocity and a mean dissipation scale. This proportionality holds for moderate Re and it begins to fail at $Re \approx 65\,000$ (see Supplementary Information, Fig. 2.6). Alternative theoretical derivations of the power law based on related arguments have been suggested [Gioia and Chakraborty, 2006; Tran *et al.*, 2010]. In the following we investigate the transformation turbulence undergoes at $Re \approx 65\,000$ and we identify the structures responsible for the friction increase.
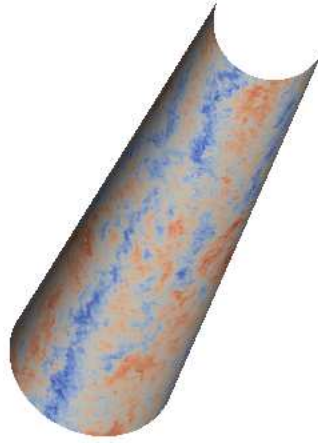
Figure 2.2: Visualization of large scale motions in the log–layer. Data from DNS at $r^+ = 150$ and $Re = 80\,000$. Red and blue areas correspond to positive and negative streamwise velocity fluctuations, respectively. The pipe length is $10R$ and the flow goes from top to bottom.

In the Re regime investigated the maximum production occurs at the so called inner peak, situated in the near wall buffer layer (see Supplementary Information, Fig. 2.7). A distinctive feature of high Re wall turbulence is the emergence of a second peak. This peak, known as the outer peak, takes place further away from the wall, in the so called log–layer, and it is associated with structures having large streamwise wavelengths, *i.e.* large scale motions [Kim and Adrian, 1999; Smits *et al.*, 2011] (see Fig. 2.2 for an example of these structures). While the outer peak occurs at Re larger than those investigated here [Hultmark *et al.*, 2012], as shown in Supplementary Information, Fig. 2.7, it becomes progressively larger as Re increases and the first signs of its associated dynamics are observable at Re similar to those at which f departs from the Blasius scaling [Smits *et al.*, 2011].

In order to explore how the large scale motions associated to this outer peak influence the friction scaling, we first decompose f into its laminar and turbulent contributions, as proposed by Fukagata *et al.* [2002],

$$f = \underbrace{64/Re}_{\text{laminar}} + \underbrace{128 \int_0^1 r^2 \langle -u'v' \rangle dr}_{\text{turbulent}}, \qquad (2.1)$$

where $\langle -u'v' \rangle$ denotes the Reynolds shear stress averaged over the pipe axis and time. Next, the integral on the RHS can be decomposed into contributions from
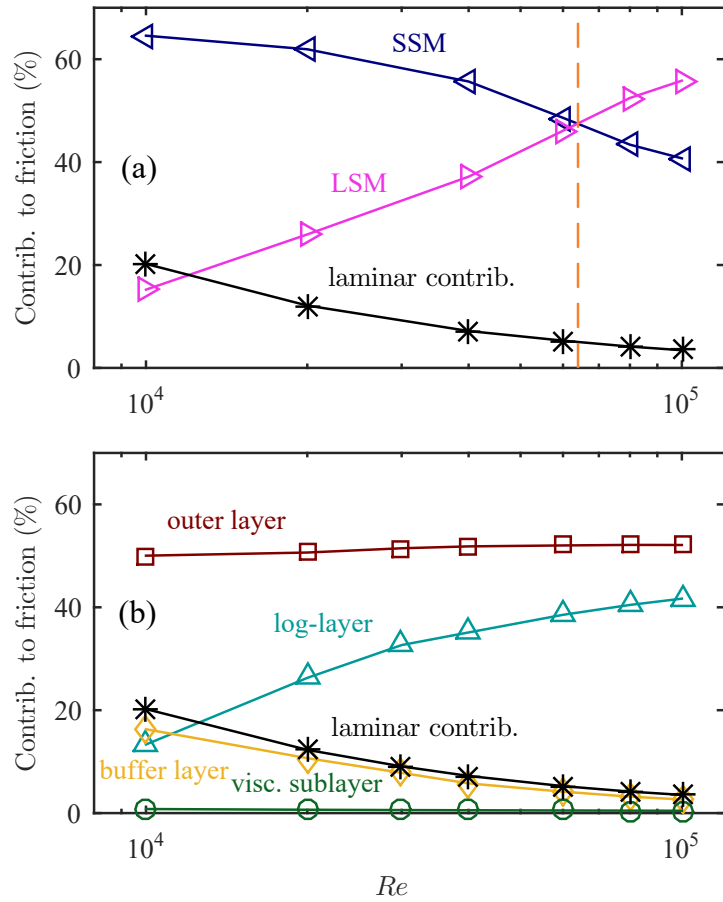
Figure 2.3: Reynolds number dependence of the laminar and turbulent contributions to the friction factor. The turbulent contribution is in turn separated into (a), the contribution of LSM and SSM using $\lambda_z^+ = 3000$ as cutoff wavelength and (b), the contribution of the distinct layers making up the wall normal direction. The yellow dashed line in (a) indicates the Reynolds number at which the contribution of the LSM becomes dominant ($Re \approx 65\,000$).

small and large scale motions, respectively SSM and LSM, (see Supplementary Information, Section 2.2.5 for details),

$$f = 64/Re + 128 \int_0^1 r^2 \langle -u'v' \rangle_{\text{LSM}} dr$$
$$+ 128 \int_0^1 r^2 \langle -u'v' \rangle_{\text{SSM}} dr. \tag{2.2}$$

Fig. 2.3 (a) shows the Re dependence of the three terms on the right hand side of equation (2.2). As Re increases, the contribution of the large scale motions to f increases progressively, whereas conversely, the contribution of the small scale motions decreases. For $Re > 65\,000$, the contribution of the large scale motions becomes dominant, coinciding with the deviation of f from the power law and its approach towards the Prandtl–von Kármán friction law.

Equation (2.1) can also be used to investigate how the turbulent contribution to f varies with the distance from the wall. Here, $\langle -u'v' \rangle$ is split into four terms corresponding to each of the layers that make up the wall normal direction, *i.e.* viscous sublayer, buffer, logarithmic and outer layers. This results in four integrals, namely

$$f = 64/Re + 128 \left(\int_0^{0.85} r^2 \langle -u'v' \rangle_{\text{outer}} dr + \int_{0.85}^{r^+=30} r^2 \langle -u'v' \rangle_{\text{log}} dr + \right.$$
$$\left. + \int_{r^+=30}^{r^+=5} r^2 \langle -u'v' \rangle_{\text{buffer}} dr + \int_{r^+=5}^{r^+=0} r^2 \langle -u'v' \rangle_{\text{viscous}} dr \right), \tag{2.3}$$

As shown in Fig. 2.3 (b), the biggest contribution to friction (nearly 50%) occurs in the outer layer. This outer layer contribution remains nearly constant as Re increases, suggesting that the dynamics in this region is not directly related to the transition taking place at $Re \approx 65\,000$. Instead, the change in the friction contribution takes place in the log–layer. It increases from small values at low Re to almost 40% at $Re = 65\,000$. These observations (Figs. 2.3 (a) and (b)) infer that the large scale motions and their modification of the log–layer are responsible for the transition in the friction scaling. To further test this link, we next compute the correlation between velocity fluctuations in the log–layer and friction. To this end, instantaneous friction factors, f_{inst}, were calculated at each streamwise location. At the same locations, the streamwise velocity was decomposed into fluctuations that are associated with

large scale motions and those that are of small streamwise extent, u'_{LSM} and u'_{SSM} respectively (see Supplementary Information, Section 2.2.6 for details). From these data we obtain the joint probability density functions (JPDF) of friction and velocity fluctuations, shown for three Re in Fig. 2.4, where friction is plotted relative to the Blasius scaling $f^* = f_{\text{inst}} - f_{\text{Blasius}}$. For the SSM ($\lambda_z^+ < 3000$, lower row), the distribution remains virtually insensitive to changes in Re and exhibits a nearly circular shape, indicating that events with high speed and high (or low) friction are equally probable as those with low speed and high (or low) friction. This is also the case for the LSM ($\lambda_z^+ > 3000$, upper row), at low Re, *e.g.* $Re = 10\,000$. However, at large Re, *e.g.* $Re = 80\,000$, the distribution becomes elliptical, reflecting a strong correlation between u'_{LSM} and f^* in the first and third quadrants. This change in the shape of the JPDF clearly illustrates the transition taking place and confirms that it is associated with the dynamics of large scale motions in the log–layer. Furthermore it implies that positive velocity fluctuations impact the wall shear stress and lead to larger friction. Likewise, negative large scale fluctuations are strongly correlated with low friction events but seem to occur less often (the distribution is skewed towards positive fluctuations). This finding is in line with the observations that positive (negative) large scale fluctuations in the log–layer induce a large (small) amplitude modulation in the near wall velocity [Hutchins and Marusic, 2007b; Hutchins and Marusic, 2007a]. Overall, this large scale driven temporal intermittency changes the local velocity gradient at the wall and therefore elucidates the increase in drag observed after $Re > 65\,000$.

We propose that the Blasius power law is the signature of an intermediate regime, bridging the gap between the transitional regime, characterized by turbulent puffs, and high Reynolds number turbulence, dominated by large and very large scale motions. While these latter motions are known to dictate turbulent production and momentum transport at high Re [Guala *et al.*, 2006], their impact on the friction scaling had not been considered previously. We expect that their dominance of turbulent drag will continue to increase with Re and consequently refined models of wall friction must take these structural changes into account.
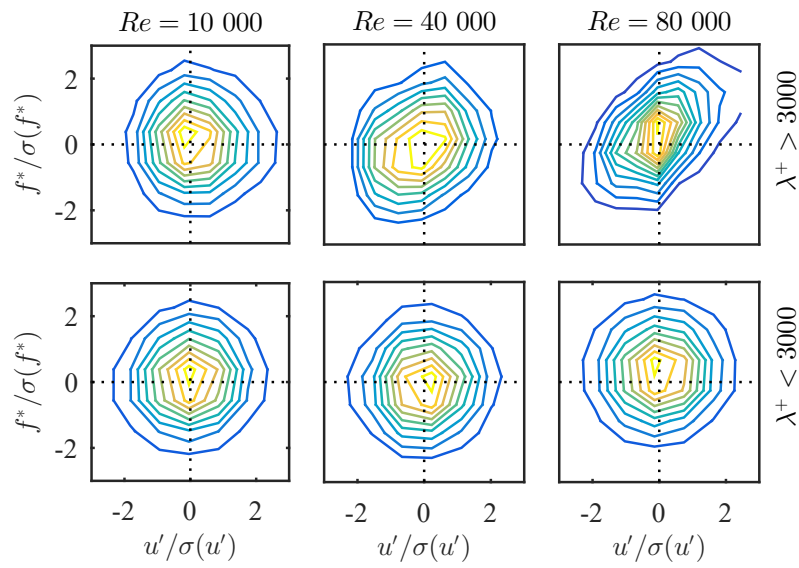
Figure 2.4: Joint probability density function (JPDF) between the deviation from the Blasius scaling f^* and the average velocity fluctuations in the log–layer u' (divided between large and small scales using the threshold $\lambda_z^+ = 3000$), normalized with their standard deviation, $\sigma(u')$. The lower row shows the JPDF for the small scale motions at $Re = 10\,000$, $Re = 40\,000$ and $Re = 80\,000$. In all three cases the distributions are close to circular and do not notably alter with Re. For the large scale motions (upper row), however the distribution considerably changes and becomes elliptical at large Re, reflecting that u'_{LSM} and f^* become correlated.

2.2 Supplementary Information

2.2.1 Experimental setup and methodology

The experimental apparatus is sketched in Fig. 2.5. Deionized water flows through a 3.6 m long, precision bore circular pipe (Duran, KPG) with an inner diameter of $D = 10\pm0.01$ mm. The measurement section consists of three separate segments, each $240R$ long. Custom PMMA flanges were used to join these segments smoothly. Water is pushed through the pipe into an external reservoir by using a large scale, custom made syringe pump with an internal diameter of $D_p = 125 \pm 0.11$ mm and total length $L_p = 1500 \pm 0.1$ mm. The syringe rod is connected to a linear actuator (Festo, ESBF-BS-80-1500-15P, not shown in Fig. 2.5) driven by a servomotor (Festo, EMMS-AS-70-M-LS-RS, not shown in Fig. 2.5) that allows to control the syringe plunger speed with an accuracy of ±0.01 mm/s. The flow is perturbed at the inlet of the glass pipe by a pin obstacle to ensure fully turbulent flow for $Re > 3000$. Turbulence is allowed to develop over a length of $240R$ and the pressure drop is measured from this location across a length of $L = 240R$. Differential pressure is measured by sampling the wall pressure with two taps ($d = 0.5$ mm) drilled through the custom PMMA flanges. The hole surface has been polished to remove any residual burr. In order to resolve friction factor better than the separation between Blasius and Prantl–von Kármán laws ($\approx 2.5\%$), two high resolution pressured transducers (Honeywell, HSCDRRN010KDAA5 and HSCDRRN030PDAA5, indicated by ΔP in Fig. 2.5) were carefully calibrated. For Reynolds numbers up to 40 000, we calibrated the first sensor (full scale 16 kPa) by using a 2 m tall water column. For larger Reynolds numbers, the other sensor (full scale 200 kPa) was calibrated with a pressure regulator against a pressure gauge (Fluke 700G). The water temperature is recorded at the outlet of the pipe with a Pt–100 probe (indicated as T in Fig. 2.5) and it is kept constant by a heat exchanger and a temperature controller unit (Thermo Electron Haake DC30 and Haake K20). During a typical measurement session, the syringe pump is initially actuated continuously back and forth for approximately six hours to allow water to reach thermal equilibrium. For each run, the piston speed,
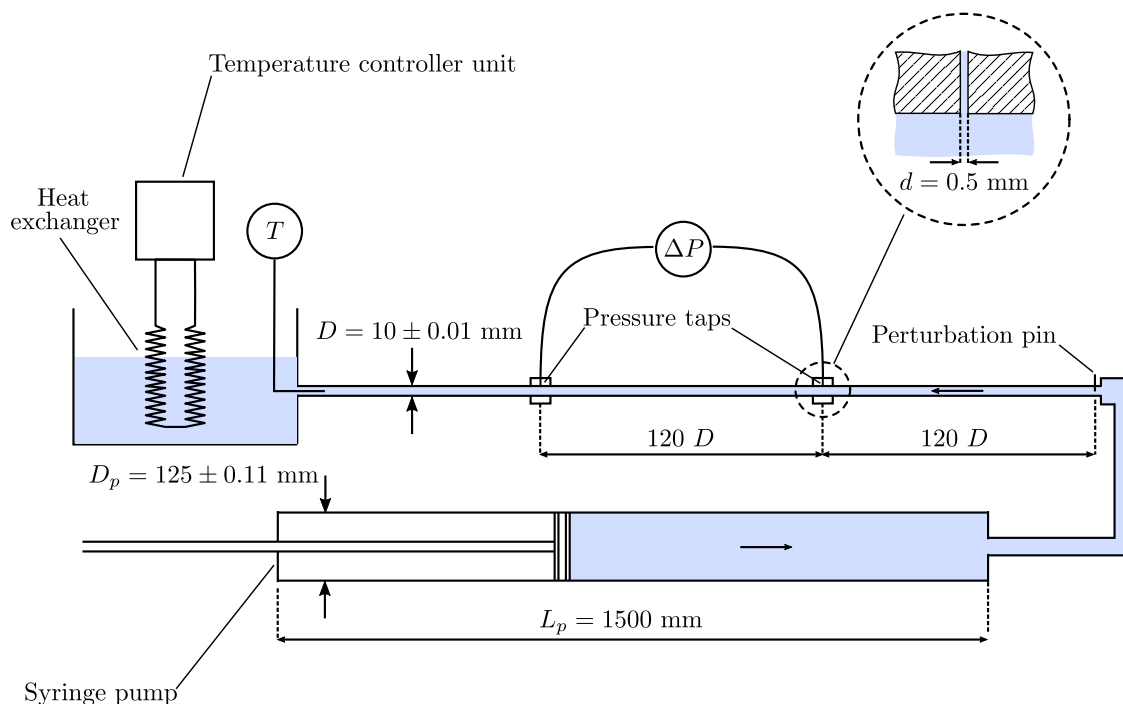
Figure 2.5: Sketch of the experimental setup. Drawing not to scale.

the water temperature and the differential pressure are measured simultaneously for about 12 000 advective time units (D/U, where U is the mean velocity). The Reynolds number is hence imposed and kept constant within ±0.2% of the nominal value. Friction factors are calculated from the pressure drop measurements using the Darcy–Weisbach formula, $f = 2\Delta P D/(\rho U^2 L)$, where ρ is the density of water. To ascertain the accuracy of the friction factor, we repeated the measurements several times at 18°C and 37°C to ensure repeatability under different speeds of the syringe plunger. The two sigma confidence interval of the mean friction was found to be less than ±0.4%.

2.2.2   Numerical simulations

The simulations were performed using *NSPipeFlow*, a highly scalable, pseudo–spectral solver for the Navier–Stokes equations in a pipe geometry which has been developed in–house. Spatial discretization of the equations in the azimuthal and axial directions were accomplished via Fourier–Galerkin expansions and eighth order central finite differences on a Gauss–Lobatto–Chebyshev grid were used in

the radial direction. The equations were advanced in time using a second–order predictor–corrector method. The time step size was dynamically adjusted using an algorithm based on the Courant–Friedrich–Lewy condition to ensure computational stability. The code was made parallel using a hybrid MPI–OPENMP programming strategy. For further details about the time–stepper and parallelization strategy, the reader is referred to [Lopez *et al.*, 2019] and [Shi *et al.*, 2015], respectively. The parameters of the simulations are shown in the table 2.1. A constant mass flow was enforced in the simulations (U = 0.5) and the average friction factor was calculated from the average dimensionless wall shear stress, τ_w, as $f = 8\tau_w/U^2$. The simulations were run until convergence in the average friction factor was achieved. Simulations for $Re > 60\,000$ were performed in Vienna Scientific Cluster using 2048 cores (256 MPI tasks and 8 THREADS per task) in nodes equipped with processors Intel Xeon E5-2650v2, 2.6 GHz and connected with high–speed InfiniBand. The rest of simulations were performed in our local cluster (IST Austria cluster) using up to 512 cores.

2.2.3 Production and dissipation balance

We show that Blasius $-1/4$ exponent can be rationalized using dimensional analysis. In a statistically steady state, the mean turbulent kinetic energy production $\overline{\mathcal{P}}$ must equal the mean viscous dissipation rate $\overline{\epsilon}$. Using the characteristic velocity and length of pipe flow, U and R, respectively, and defining a mean dissipative scale, $\overline{\eta}$, we can write dimensional estimates for $\overline{\mathcal{P}} \propto U^3/R$ and $\overline{\epsilon} \propto \nu^3/\overline{\eta}^4$. With these definitions, the energy balance results in

$$\overline{\eta}/R \propto Re^{-3/4} \tag{2.4}$$

Eq. (2.4) is akin to Kolmogorov's first similarity hypothesis and its validity over the range of Re investigated here has been verified using the numerical data (see Fig. 2.6 (a)). Multiplying both sides of eq. (2.4) by $(\overline{\eta}/\nu)^2$, we can rearrange terms to obtain

$$Re^{-1/4}\rho U^2 \propto \mu U/\overline{\eta} \tag{2.5}$$

Re	Re_τ	length (R)	Δ_r^+ (min)	Δ_r^+ (max)	$\Delta_{(R\theta)}^+$	Δ_z^+	δ_t
3 000	107.95	10.0	0.053	2.44	7.06	5.62	$4.80 \cdot 10^{-3}$
5 000	171.94	10.0	0.060	3.14	7.10	6.14	$4.80 \cdot 10^{-3}$
10 000	314.55	16.0	0.026	2.91	7.06	7.14	$4.80 \cdot 10^{-3}$
15 000	447.76	10.0	0.020	2.09	6.39	6.99	$4.44 \cdot 10^{-3}$
20 000	575.88	16.0	0.016	2.70	7.23	7.20	$1.91 \cdot 10^{-3}$
25 000	700.17	16.0	0.011	2.74	6.87	7.29	$1.54 \cdot 10^{-3}$
30 000	822.55	16.0	0.013	3.22	6.80	6.85	$1.14 \cdot 10^{-3}$
40 000	1 059.64	10.0	0.016	4.15	7.16	6.89	$9.76 \cdot 10^{-4}$
60 000	1 511.97	10.0	0.013	4.46	7.91	7.84	$7.02 \cdot 10^{-4}$
80 000	1 948.37	10.0	0.017	5.75	8.27	7.61	$4.81 \cdot 10^{-4}$
100 000	2 377.53	12.0	0.009	4.71	10.31	8.57	$3.11 \cdot 10^{-4}$

Table 2.1: From left to right: Reynolds number Re based on the mean velocity, Reynolds number Re_τ based on the friction velocity, pipe length, minimum and maximum radial resolution (in inner units), azimuthal resolution (in inner units), axial resolution (in inner units) and average time step size δ_t.
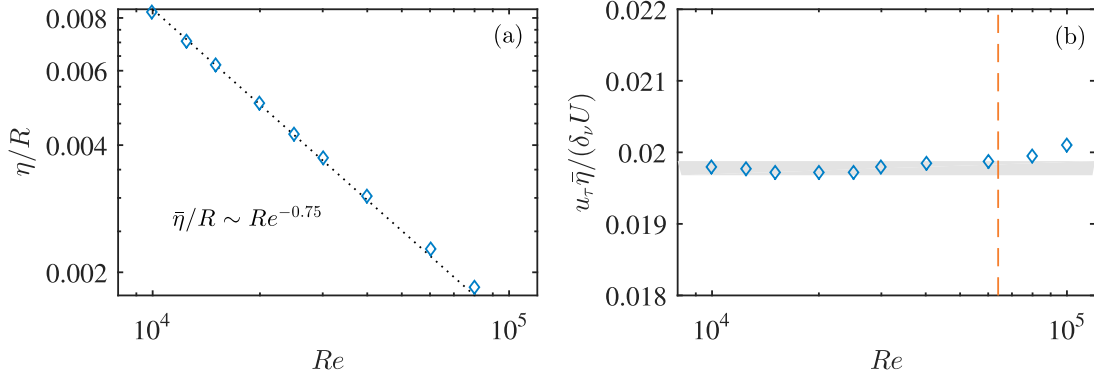
Figure 2.6: (a) Numerical verification of equation (2.4). (b) Ratio $\gamma = u_\tau \overline{\eta}/(\delta_v U)$ as a function of Re obtained from DNS. The vertical, dashed orange line indicates the deviation from the Blasius friction law.

By drawing an analogy between Eq. (2.5) and the Darcy–Weisbach formula for friction factors ($8f\rho U^2 = \mu u_\tau/\delta_v$, where μ is the dynamic viscosity, u_τ the friction velocity and δ_v the viscous length), one can easily see that f will follow the Blasius relation ($f \propto Re^{-1/4}$) if the proportionality

$$\frac{U}{\overline{\eta}} \propto \frac{u_\tau}{\delta_v},\qquad(2.6)$$

is satisfied. To test whether condition (2.6) holds, the ratio $\gamma = u_\tau\overline{\eta}/(\delta_v U)$ was determined from DNS (see Fig. 2.6 (b)). As seen, γ remains nearly constant up to $Re \approx 65\,000$ and so the proportionality is indeed met over the Blasius regime. For $Re > 65\,000$, γ deviates progressively from its constant value at smaller Re, which is also consistent with the observed deviation of f from the Blasius scaling. We note that an expression analogous to (2.6) was found by Gioia and Chakraborty [2006] following a different line of argument. However, numerical verification of such condition is given here for the first time.

2.2.4 Further details about the computations

Fig. 2.7 shows the variation of the turbulence intensity profiles obtained in our simulations as the Reynolds number increases. For all Re, the turbulence intensity is maximal at the buffer layer and then decays monotonically as one moves away from the wall. This maximum in turbulence intensity is known as the inner peak
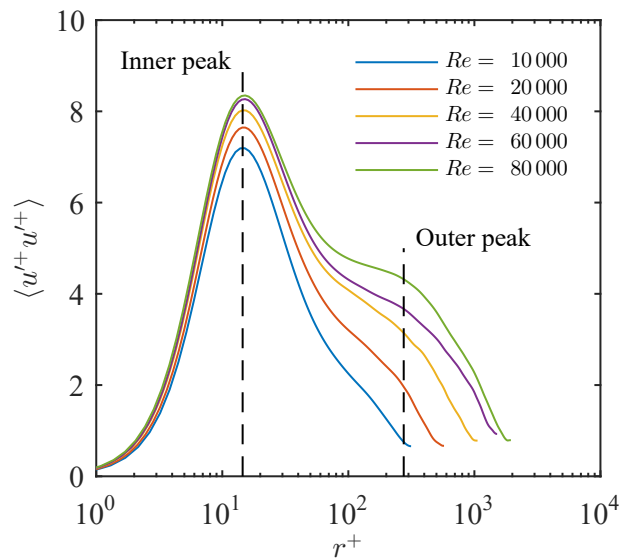
Figure 2.7: Radial profiles of the turbulence intensity in inner units as a function of the Reynolds number. The dashed lines indicate the location of the inner peak ($r^+ = 14$) and the approximate region of the logarithmic layer where the outer peak develops.

and it is associated with the dynamics of coherent structures in the near wall region, *i.e.* quasi–streamwise vortices and streaks [Kline *et al.*, 1967; Hamilton *et al.*, 1995]. A second peak associated with LSM, *i.e.* the outer peak, is known to emerge in the logarithmic layer [Smits *et al.*, 2011], but it is only observable in turbulence intensity profiles at $Re \approx 300\,000$ [Hultmark *et al.*, 2012]. However, a progressive increase of the turbulence intensity in the logarithmic layer can be clearly observed from Fig. 2.7 (see dashed line indicating the approximate location where the outer peak develops). This becomes particularly evident at Reynolds numbers between 60 000 and 80 000, coinciding with the change in the scaling of the friction factor. Inspection of the streamwise energy spectra show that these changes in the log–layer are consistent with the first signs of the outer peak and are therefore related to highly energetic LSM.
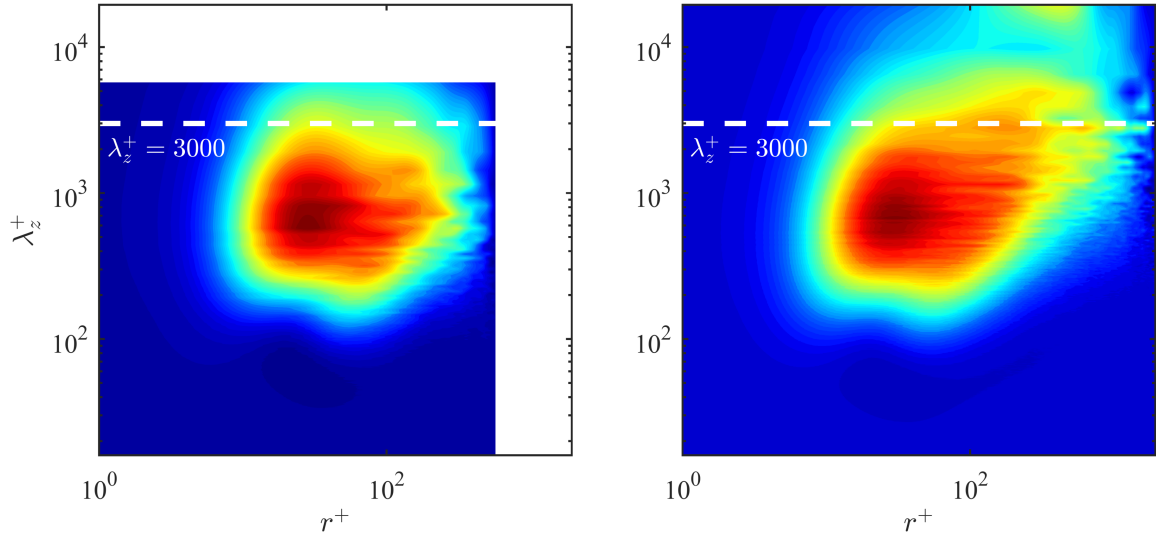
Figure 2.8: Premultiplied cospectra of the Reynolds shear stress $k_z \Phi_{u'v'}$ at $Re = 20\,000$ (left) and $Re = 80\,000$ (right) in inner units. The x–axis shows the distance from the wall r^+, whereas the y–axis indicates the streamwise wavelength of the structures λ_z^+. The white dashed line indicates the cutoff wavelength $\lambda_z^+ = 3000$ used to separate large and small scale motions.

2.2.5 Determination of the contribution of small and large scale motions to the Reynolds shear stress

The contribution of the large and small scale motions to $\langle -u'v' \rangle$ was determined from the streamwise cospectra of the Reynolds shear stress ($\Phi_{u'v'}$). Following previous studies, we chose a cutoff wavelength of $\lambda_z^+ = 3000$. As shown in Fig. 2.8, this cutoff wavelength separates to a good approximation scales related to the inner peak dynamics from those associated with the developing outer peak at these Re. $\Phi_{u'v'}$ was integrated up to and from the cutoff wavelength to obtain the contributions of the small and large scale motions to $\langle -u'v' \rangle$, respectively.

2.2.6 Correlation between friction factor and average fluctuations in the log–layer

To examine the correlation between friction factor and average streamwise fluctuations in the log–layer, the following procedure was followed. For each snapshot saved in the simulations, instantaneous friction factors, f_{inst}, were calculated at each streamwise location from the local velocity profile. At the same locations,

large and small scale streamwise velocity fluctuations, u'_{LSM} and u'_{SSM}, respectively, were obtained by filtering the fluctuating velocity field ($\lambda_z^+ > 3000$ and $\lambda_z^+ < 3000$, respectively) and averaging over the log–layer. The JPDFs between f_{inst} and u'_{LSM} or u'_{SSM} were then calculated. Defining the deviation of f_{inst} with respect to Blasius, $f^* = f_{\text{inst}} - f_{\text{Blasius}}$, combinations of values for f^* and u' (either LSM or SSM) can be mapped onto a four quadrants space. The first and second quadrants correspond to events where friction is larger than Blasius and the average velocity fluctuations in the log–layer are positive or negative, respectively. Similarly, the fourth and third quadrants reflect events where friction is below Blasius and velocity fluctuations are positive or negative, respectively. This representation enables to readily identify events which are directly correlated with the deviation of the friction factor from the Blasius scaling.

3   Destabilizing turbulence in pipe flow

Turbulence is the major cause of friction losses in transport processes and it is responsible for a drastic drag increase in flows over bounding surfaces. While much effort is invested into developing ways to control and reduce turbulence intensities [Lumley and Blossey, 1998; Kasagi *et al.*, 2009b; Kim and Bewley, 2007], so far no methods exist to altogether eliminate turbulence if velocities are sufficiently large. We demonstrate for pipe flow that appropriate distortions to the velocity profile lead to a complete collapse of turbulence and subsequently friction losses are reduced by as much as 90%. Counterintuitively, the return to laminar motion is accomplished by initially increasing turbulence intensities or by transiently amplifying wall shear. Since neither the Reynolds number *Re* nor the shear stresses decrease (the latter often increases), these measures are not indicative of turbulence collapse. Instead an amplification mechanism [Trefethen *et al.*, 1993; Brandt, 2014] measuring the interaction between eddies and the mean shear is found to set a threshold below which turbulence is suppressed beyond recovery.

3.1 Letter

Flows through pipes and hydraulic networks are generally turbulent and the friction losses encountered in these flows are responsible for approximately 10% of the global electric energy consumption. Here turbulence causes a severe drag increase and consequently much larger forces are needed to maintain desired flow rates. In pipes, both laminar and turbulent states are stable (the former is believed to be linearly stable for all Re, the latter is stable if $Re > 2040$ [Avila *et al.*, 2011]), but with increasing speed the laminar state becomes more and more susceptible to small disturbances. Hence in practice most flows are turbulent at sufficiently large Re. While the stability of laminar flow has been studied in great detail, little attention has been paid to the susceptibility of turbulence, the general assumption being that once turbulence is established, it is stable.

Many turbulence control strategies have been put forward to reduce the drag encountered in shear flows [Bewley *et al.*, 2001; Högberg *et al.*, 2003; Auteri *et al.*, 2010; Moarref and Jovanović, 2010; Lieu *et al.*, 2010; Quadrio *et al.*, 2009; Hof *et al.*, 2010; Rathnasingham and Breuer, 2003; Willis *et al.*, 2010; Du and Karniadakis, 2000; Min *et al.*, 2006]. Recent strategies employ feedback mechanisms to actively counter selected velocity components or vortices. Such methods usually require knowledge of the full turbulent velocity field. In computer simulations [Bewley *et al.*, 2001; Högberg *et al.*, 2003], it could be demonstrated that under these ideal conditions, flows at low Reynolds number can even be relaminarized. In experiments the required detailed manipulation of the time dependent velocity field is, however, currently impossible to achieve. Other studies employ passive (*e.g.* riblets) or active (oscillations or excitation of traveling waves) methods to interfere with the near wall turbulence creation. Typically here drag reduction of 10% to 40% has been reported, but often the control cost is substantially higher than the gain, or a net gain can only be achieved in a narrow Reynolds number regime.

Instead of attempting to control or counter certain components of the complex fluctuating flow fields, we will show in the following that by appropriately disturbing the mean profile, turbulence can be pushed outside its limit of existence and as

a consequence the entire flow relaminarizes. Disturbance schemes are developed with the aid of direct numerical simulations (DNS) of pipe flow and subsequently implemented and tested in experiments. In the DNS a flow is simulated in a five diameter (D) long pipe and periodic boundary conditions are applied in the axial direction. Initially we perturb laminar pipe flow by adding fluctuation levels of a fully turbulent velocity field rescaled by a factor k to a laminar flow field. As shown in Fig. 3.1a (dark blue curve), for small initial perturbations, *i.e.* small k, the disturbance eventually decays and the flow remains laminar. For sufficiently large amplitudes (k of order unity) turbulence is triggered (purple, red and cyan curves). So far this is the familiar picture of the transition to turbulence in shear flows, where turbulence is only triggered if perturbation amplitudes surpass a certain threshold. However, when increasing the turbulent fluctuations well beyond their usual levels ($k > 2.5$), surprisingly the highly turbulent flow almost immediately collapses and returns to laminar (light and dark green curves). Here the initially strong vortical motion leads to a redistribution of shear resulting in an unusually flat velocity profile (black profile in Fig. 3.1c).

To achieve a similar effect in experiments we increase the turbulence level by vigorously stirring a fully turbulent pipe flow ($Re = 3500$), employing four rotors located inside the pipe $50D$ downstream of the pipe inlet (see Supplementary Information Video 1, Fig. 3.17 and Supplementary Information Fig. 3.4). As the highly turbulent flow proceeds further downstream it surprisingly does not return to the normal turbulence level but instead it quickly reduces in intensity until the entire flow is laminar (Fig. 3.1b top to bottom and Supplementary Information Video 1, Fig. 3.17). Being linearly stable the laminar flow persists for the entire downstream pipe. In a second experiment, turbulent flow ($Re = 3100$) is disturbed by injecting fluid through 25 small holes (0.5 mm diameter) in the pipe wall (holes are distributed across a pipe segment with a length of $25D$, see Supplementary Information Fig. 3.6). Each injected jet creates a pair of counter–rotating vortices, intensifying the eddying motion beyond the levels of ordinary turbulence at this Re. The additional vortices redistribute the flow and as a consequence the velocity profile is flattened (Fig. 3.1c, purple dotted line). When the perturbation is actuated
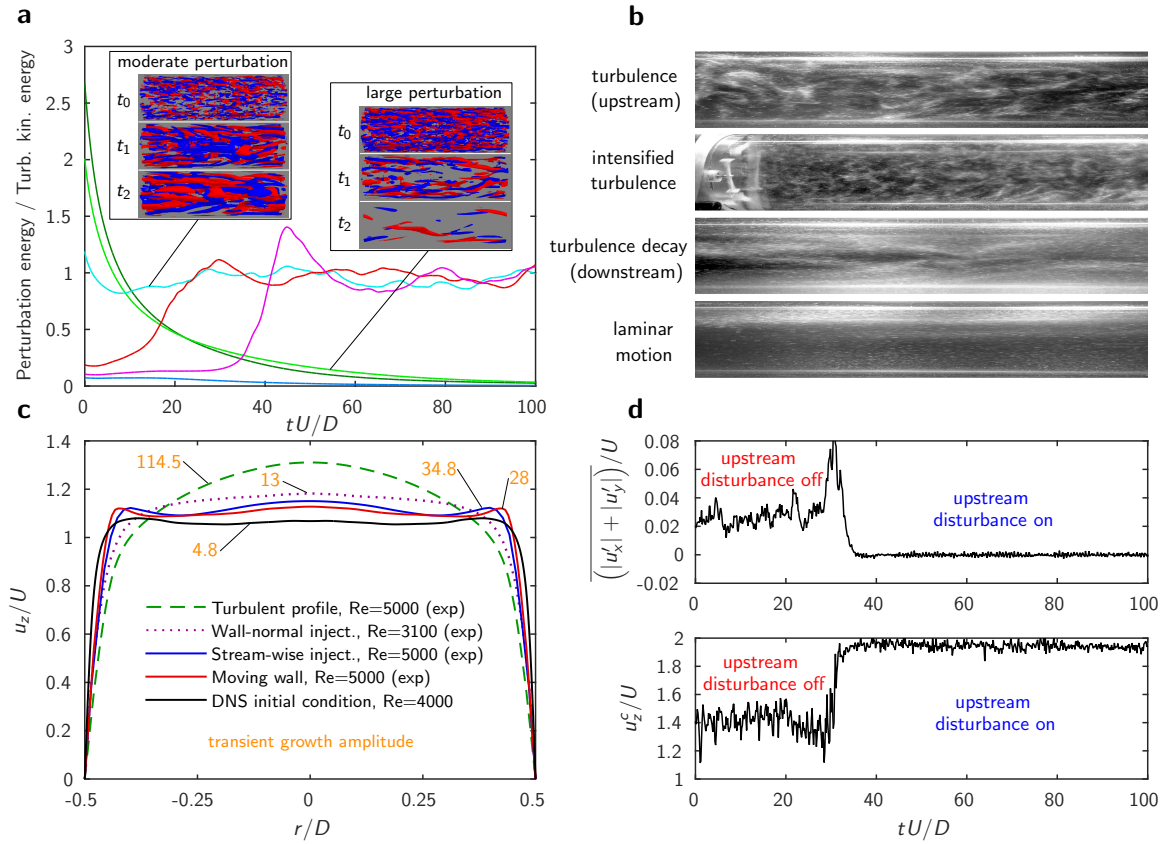
Figure 3.1: Perturbing turbulence. (a) Direct numerical simulations of pipe flow starting from turbulent initial conditions (taken from a run at $Re = 10\,000$), rescaled by a constant factor k and added to the laminar base flow at $Re = 4000$, which was then integrated forward in time (at $Re = 4000$). For small initial energies perturbations die out (dark blue curve). For sufficiently large energies ($k \approx 1$) transition to turbulence occurs (red, purple, cyan). For even larger energies ($k > 2.5$) however the initially turbulent flow is destabilized and collapses after a short time (light and dark green curve). The 6 streamwise vorticity isosurface figures show $\omega_z = +/-(\text{red/blue})\,7.2,\ 2.0,\ 1.6\,U/D$ respectively at snapshot times $t_0 = 0$, $t_1 = 5$ and $t_2 = 10(D/U)$. (b) Fully turbulent flow (top panel) at $Re = 3100$ is perturbed by vigorously stirring the fluid with four rotors. The more strongly turbulent flow (panel 2) eventually relaminarizes as it proceeds downstream (panel 3 and 4). (c) Temporally and azimuthally averaged velocity fields of modified/perturbed flow fields in simulations and experiments. u_z is the streamwise velocity component, the cross stream components are denoted by u_x and u_y. (d) Relaminarization of fully turbulent flow in experiments at $Re = 3100$. The flow is perturbed by injecting 25 jets of fluid radially through the pipe wall. When actuated the fluctuation levels in the flow drop (top panel) and the centre line velocity switches from the turbulent level to the laminar value ($2U$, where U is the mean velocity in the pipe), bottom panel.

downstream, fluctuation levels drop and the center line velocity returns to its laminar value (Fig. 3.1d). Laminar motion persists for the remainder of the pipe. In this case the frictional drag is reduced by a factor of 2. Overall the injected fluid only amounts to $\approx 1.5\%$ of the total flow rate in the pipe. With the present actuation device we achieved a net power saving (taking all actuation losses into account) of 31% over the remainder of the pipe. On the other hand the minimum actuation cost required to create the necessary flow disturbance is substantially lower ($\approx 1\%$), so that the net saving potential at this Re is 45% (see Supplementary Information, Section 3.3.4).

In another experiment we attempted to disrupt turbulence ($Re = 5000$) by injecting fluid parallel to the wall in the streamwise direction (see Supplementary Information Fig. 3.5 and 3.7). Unlike for the previous case, this disturbance does not result in a magnification of cross–stream fluctuations, but instead it directly increases the wall shear stress and hence also the friction Reynolds number, Re_τ. Directly downstream of the injection point the latter is increased by about 15%. The acceleration of the near wall flow automatically causes deceleration of the flow in the pipe center (the overall mass flux is held constant) hence again resulting in a flatter velocity profile (blue in Fig. 3.1c). Despite the local increase in Re_τ, further downstream the fluctuation levels begin to drop and the turbulent flow has been sufficiently destabilized that eventually ($30D$ downstream) it decays and the flow returns to laminar. As a result, friction losses drop by a factor of 2.9 (see Fig. 3.2a) and the potential net power saving (not including actuation losses) is 55% (see Supplementary Information, Section 3.3.4). For this type of perturbation we find that relaminarization occurs for an intermediate injection range ($\approx 15\%$ of the flow rate in the pipe), while for smaller and larger rates the flow remains turbulent. A property common to all above relaminarization mechanisms is their effect on the average turbulent velocity profile.

In order to test a possible connection between the initial flat velocity profile and the subsequent turbulence collapse, we carried out further computer simulations where this time a forcing term was added to the full Navier–Stokes equations. The force was formulated such that it decelerates the flow in the central part of the pipe
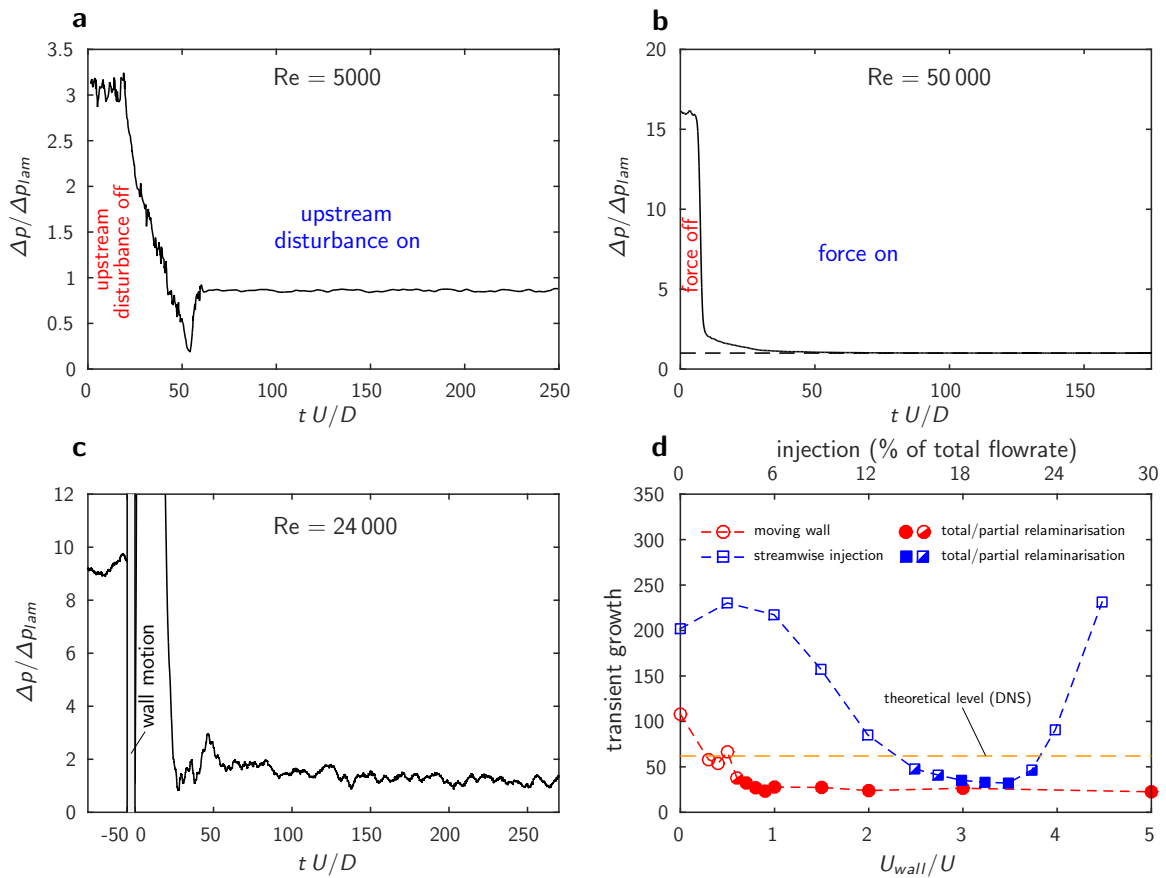
Figure 3.2: Laminarization mechanisms. (a) After the streamwise near wall injection is actuated the pressure drop reduces to its laminar value. (b) A body force term is added in the numerical simulations which leads to an on average flatter flow profile (the fluid close to the wall is accelerated while it is decelerated in the near wall region). Disturbing the flow profile in this manner leads to a collapse of turbulence, here shown for $Re = 50\,000$ where consequently friction losses drop by a factor of 10. (c) In this experiment the near wall fluid is accelerated via a sliding pipe segment, which is impulsively moved in the axial direction. Directly after the pipe segment is stopped the flow has a much flatter velocity profile. Subsequently turbulence collapses and the frictional drag drops to the laminar value. (d) Transient growth measures the efficiency of the lift–up mechanism, *i.e.* how perturbations in the form of streamwise vortices are amplified while growing into streaks (deviations of the streamwise velocity component). All disturbance schemes used lead to a reduction in transient growth. The threshold value below which relaminarization occurs in the numerical (control via body force) is indicated by the orange line. For comparison the experimental flow disturbance mechanisms are shown in blue (streamwise injection) and red (moving wall). In agreement with the numerical prediction all disturbance amplitudes that lead to a collapse of turbulence (solid symbols) fall below the threshold value found in the simulations.

cross section while it accelerates the flow in the near wall region. The mass flux through the pipe and hence Re remain unaffected (see Supplementary Information Eq. (3.19) and Supplementary Information Fig. 3.10). Unlike in the experiments where the disturbance is applied locally and persists in time, here the forcing is applied globally. As shown in Fig. 3.2b, upon turning on the forcing with sufficient amplitude the initially fully turbulent flow completely relaminarizes. Hence a profile modification alone suffices to destabilize turbulence. Interestingly, the energy required for the forcing is smaller than the energy gained due to drag reduction (even for intermediate forcing amplitudes, see Supplementary Information Fig. 3.11). In this case we therefore obtain a net energy saving already in the presence of the forcing (in experiments the saving is achieved downstream of the perturbation location). After removal of the forcing (see Supplementary Information Fig. 3.15) turbulence fluctuation levels continue to drop exponentially and the flow remains laminar for all times. This effect has been tested for fully turbulent flow for Reynolds numbers between 3000 and 100 000 and in all cases a sufficiently strong force was found to lead to a collapse of turbulence resulting in drag decrease and hence energy saving in the numerical simulations of up to 95% (in practical situations finite amplitude perturbations may limit the persistence of laminar flow at such high Re).

We next investigate whether a profile modification on its own also relaminarizes turbulence in experiments. While body forces like that used in the simulations are not available (at least not for electrically, non–conducting fluids), profiles can nevertheless be flattened by a local change in the boundary conditions. For this purpose one pipe segment is replaced by a pipe of slightly (4%) larger diameter which is pushed over the ends of the original pipe and can be impulsively moved with respect to the rest of the pipe (see Supplementary Information Video 2, Fig. 3.18 and Supplementary Information Fig. 3.8). The pipe segment is then impulsively accelerated in the streamwise direction and abruptly stopped, the peak velocity of the $300D$ long movable pipe segment is equal or larger (up to 3 times) than the bulk flow speed in the pipe. The impulsive acceleration of the near wall fluid leads to a flattened velocity profile (red profile in Fig. 3.1c). Despite the fact that overall the

fluid is accelerated and additional shear is introduced (Re_τ is increased), after the wall motion is stopped (abruptly, over the course of 0.2 s) turbulence also in this case decays (see Fig. 3.2c and Supplementary Information Video 2, 3.18). If on the other hand the wall acceleration is reduced, with wall velocities lower than $0.8U$, turbulence survives. The impulsive wall motion is found to relaminarize turbulence very efficiently up to the highest Reynolds number ($Re = 40\,000$) that could be tested in the experiment (here the wall was moved at the bulk flow speed).

In turbulent wall–bounded shear flows, energy has to be transferred continuously from the mean shear into eddying motion, and a key factor here is the interplay between streamwise vortices (*i.e.* vortices aligned with the mean flow direction) and streaks. The latter are essentially dents in the flow profile that have either markedly higher or lower velocities than their surroundings. Streamwise vortices "lift up" low velocity fluid from the wall and transport it towards the center (see Supplementary Information Fig. 3.12). The low velocity streaks created in the process give rise to (non–linear) instabilities and the creation of further vortices. Key to the efficiency of this "lift–up mechanism" is that weak vortices suffice to create large amplitude streaks. This amplification process is rooted in the non–normality [Trefethen *et al.*, 1993] of the linear Navier Stokes operator and its magnitude is measured by the so called transient growth (TG) (see also Supplementary Information Fig. 3.13 and 3.14).

Computing TG for the forced flow profiles in the DNS, we indeed observe that TG monotonically decreases with forcing amplitude (see Supplementary Information Fig. 3.14) and it assumes its minimum value directly before turbulence collapses. Generally, the flatter the velocity profile the more the streak vortex interaction is suppressed, and in the limiting case of a uniformly flat profile the lift–up mechanism breaks down entirely.

Revisiting the experiments, the velocity profiles of all the disturbed flows considered exhibit a substantially reduced transient growth (Fig. 3.1c). For the streamwise injection, amplitudes relaminarizing the flow also show the minimum amplification (Fig. 3.2d) while at lower and higher injection rates where turbulence survives the amplification factors are higher and above the threshold found in the

simulations. Similarly for the moving wall at sufficiently large wall acceleration where relaminarization is achieved, the lift–up efficiency is reduced below threshold, while at lower wall speeds it remains above. Some parallels between the present study and injection and suction control in channels and boundary layers [Park and Choi, 1999; Sumitani and Kasagi, 1995; Fukagata *et al.*, 2002] can be drawn. While for boundary layers during the injection phase the drag downstream increases, during the suction it decreases. Suction applied to a laminar Blasius boundary layer leads to a reduction of the boundary layer thickness and this is well known to delay transition [Fransson and Alfredsson, 2003] and push the transition location downstream.

The drag reduction achieved for the different methods used to destabilize turbulence is summarized in Fig. 3.3. In each case the friction value before the profile modification corresponds to the characteristic Blasius law for turbulence (upper line) and after the disturbance it drops directly to the laminar Hagen–Poiseuille law. Hence the maximum drag reduction feasible in practice is reached (Fig. 3.3b), and at the highest Reynolds numbers studied in experiments, 90% reduction is obtained. Although the numerical and experimental relaminarization methods affect the flow in different ways, the common feature is that the velocity profile is flattened.

The presented control schemes only require manipulation of a single velocity component and moreover they do not require any information about the instantaneous turbulent velocity field. The overall control strategy is far simpler compared to recently proposed active and feedback control schemes, while at the same time it offers the maximum possible drag reduction. The future challenge is to develop and optimize methods that lead to the desired profile modifications in high Reynolds number turbulent flows.
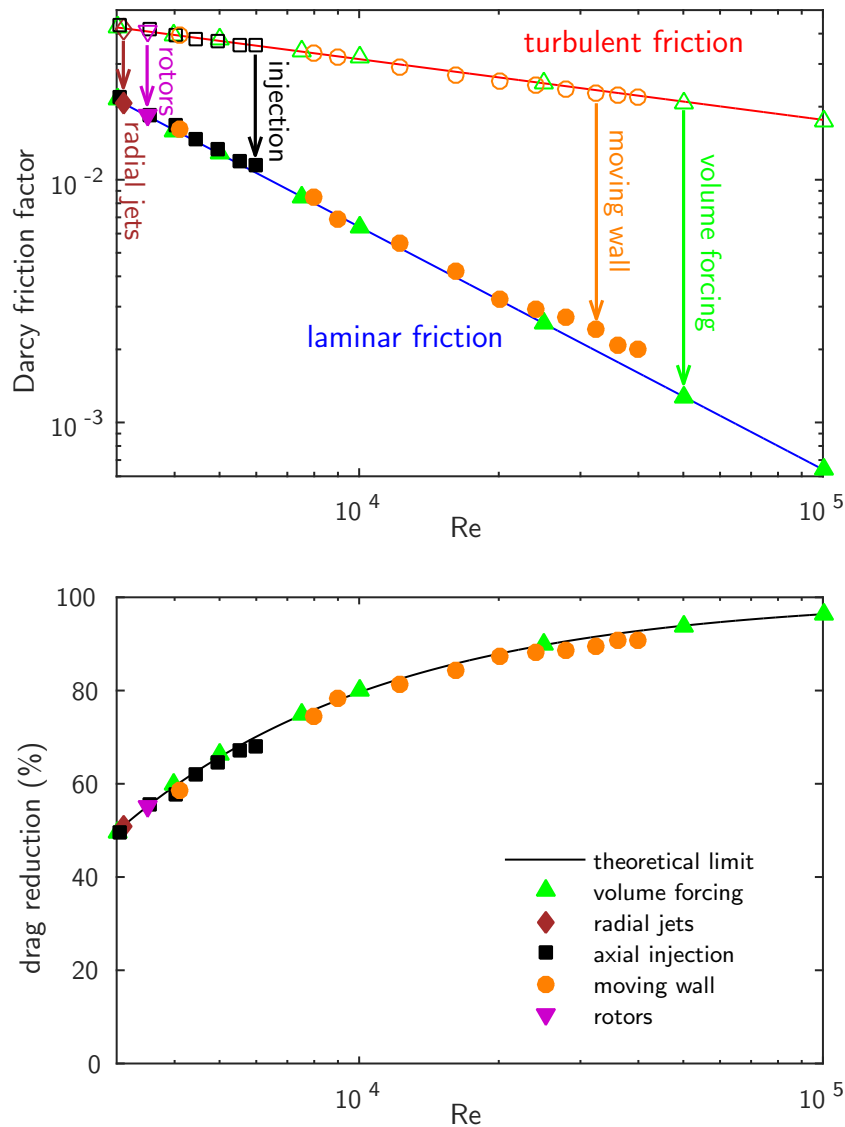
Figure 3.3: Drag reduction. (a) Friction factor, f, as a function of Re. Initially all flows are fully turbulent and friction factors follow the Blasius–Prandtl scaling ($f = 0.316Re^{0.25}$, red line). When the control is turned on flows relaminarize and the friction factors drop to the corresponding laminar values (Hagen–Poiseuille law in blue, $f = 64/Re$). The rotors, radial jet injection, axial injection and moving wall controls are carried out in laboratory experiments while the volume force cases are from direct numerical simulations of the Navier–Stokes equations. For all cases the Reynolds number is held constant throughout the experiment. (b) Drag reduction as a function of Re. For the injection perturbation a maximum drag reduction of $\approx 70\%$ was reached whereas for the moving wall and volume forcing 90% and 95% were achieved respectively. All data points reach the drag reduction limit set by relaminarization except for the $Re > 30\,000$ in experiments where values are slightly above. Although these flows are laminar (*i.e.* fluctuations are zero) the profile shape is still developing and has not quite reached the Hagen–Poiseuille profile yet (the development length required to reach a fully parabolic profile increases linearly with Re).

3.2   Methods

3.2.1   Experimental setup for the rotors

The facility consists of a PMMA pipe with inner diameter $D = 54 \pm 0.2$ mm and a total length of 12 m ($222D$) made of 2 m sections (see Supplementary Information, Fig. 3.4). The flow in the pipe is gravity driven and the working fluid is water which enters the pipe from a reservoir. The flow rate and hence the Reynolds number ($Re = UD/\nu$, where U is the mean velocity, D the diameter of the tube and ν the kinematic viscosity of the fluid) can be adjusted by means of a valve in the supply pipe. The temperature of the water is continuously monitored at the pipe exit. The flow rate is measured with an electromagnetic flow meter (ProcessMaster FXE4000, ABB). The accuracy of Re is within $\pm1\%$. To ensure fully turbulent flow the flow is perturbed by a small static obstacle (a 1 mm thick, 20 mm long needle located $10D$ after the inlet). 2 m downstream from the inlet the turbulent flow is perturbed by four small rotors which are mounted on a support structure within the pipe as indicated in Supplementary Information, Fig. 3.4. The wiring of the motors is incorporated in the support structure of the motors. The rotors are small rectangular bars with even smaller rectangular bars at the tips. Their only purpose is to induce perturbations to the flow but no propelling motion or thrust. The rotors are turned at a rate of 7 rotations per second. For the purpose of visual observations and video recordings of the flow field the flow is seeded with neutrally buoyant anisotropic particles [Matisse and Gorman, 1984]. The three locations where Supplementary Information Video 1, Fig. 3.17 was recorded are indicated in Supplementary Information, Fig. 3.4.

3.2.2   Experimental setup for the wall–normal jet injection and the streamwise injection through an annular gap

The facility consists of a glass pipe with inner diameter $D = 30 \pm 0.01$ mm and a total length of 12 m ($400D$) made of 1 meter sections (see Supplementary Information, Fig. 3.5). The flow in the pipe is gravity driven and the working fluid is water which

enters the pipe from a reservoir. The flow rate and hence the Reynolds number ($Re = UD/v$ where U is the mean velocity, D the diameter of the tube and v the kinematic viscosity of the fluid) can be adjusted by means of a valve in the supply pipe. The temperature of the water is continuously monitored at the pipe exit. The flow rate is measured with an electromagnetic flow meter (ProcessMaster FXE4000, ABB). The accuracy of Re is within ±1%. To ensure fully turbulent flow the flow is perturbed by a small static obstacle (a 1 mm thick, 20 mm long needle located $10D$ after the inlet). 2 m downstream from the inlet the turbulent flow can be perturbed in a controlled way by two different devices which are mounted within the pipe (see Supplementary Information, Fig. 3.6 and Supplementary Information, Fig. 3.7). The velocity field is measured $\approx 330D$ downstream from the disturbance (control) at the position of the light sheet. The measurement plane is perpendicular to the streamwise flow direction (pipe z–axis). All three velocity components within the plane are recorded using a high–speed stereo PIV system (Lavision GmbH) consisting of a laser and two Phantom V10 high–speed cameras with a full resolution of 2400×1900 px. The resulting spatial resolution is 77 vectors per D. The data rate is 100 Hz. Hollow glass spheres (mean diameter 13 μm, $\rho = 1.1$ g/cm) are used as seeding particles. Around the measurement plane the pipe is encased by a water filled prism such that the optical axes of the cameras are perpendicular to the air–water interface to reduce refraction and distortion of the images. Downstream of the perturbation the pressure drop Δp is measured between two pressure tabs with a differential pressure sensor (DP 45, Validyne, full range of 220 Pa with an accuracy of ±0.5%) separated by $39.5D$ in the axial direction. As the difference in pressure drop between laminar and turbulent flows is very distinct even at moderate Reynolds numbers the signal is utilized to observe whether the flow is laminar or turbulent.

3.2.3   Experimental setup for the moving pipe

A movable Perspex pipe with inner diameter $D = 26 \pm 0.1$ mm and a total length of 12 m ($461D$) is fitted to very thin–walled stainless steel pipes (MicroGroup) with

outer diameter $d_{st,o} = 25.4 \pm 0.13$ mm and a wall thickness of 0.4 ± 0.04 mm such that the Perspex pipe overlaps the steel pipes at the upstream and downstream end (see Supplementary Information, Fig. 3.8). The steel pipes are stationary (mounted on fixed bearings). With respect to the Perspex pipe they act as support and slide bearings, allowing the Perspex pipe to be moved back and forth in the axial direction. To prevent sagging the Perspex pipe is supported by six additional bushings (polymer sleeve bearings, Igus). To avoid leakage a radial shaft seal is mounted at both ends of the Perspex pipe. The length of the control section between stationary upstream and downstream stainless steel pipe, *i.e.* the actual length where the wall of the Perspex pipe is in contact with the fluid and can be moved relative to the mean flow by moving the Perspex pipe, is $L_{\text{control}} = 385D$. The Perspex pipe is connected to a linear actuator (toothed belt axis with roller guide driven by a servomotor, ELGA-TB-RF-70-1500-100H-P0, Festo; not shown in the figure). The linear actuator can move the Perspex pipe for an adjustable distance (traverse path) $s \leq s_{\max} = 1.5$ m at an adjustable velocity $U_{\text{pipe}} \leq U_{\text{pipe,max}} = 5.5$ m/s. The maximum acceleration is $a = 50$ m/s^2. The resulting wall velocity of the Perspex pipe is specified as a ratio to the mean flow velocity U, such that $u_{\text{wall}} = U_{\text{pipe}}/U$. The flow rate and hence the Reynolds number ($Re = UD/\nu$ where U is the mean velocity, D the diameter of the tube and ν the kinematic viscosity of the fluid) can be adjusted by means of a valve in the supply pipe. The temperature of the water is continuously monitored at the pipe exit. The flow rate is measured with an electromagnetic flow meter (ProcessMaster FXE4000, ABB). The accuracy of Re is within $\pm 1\%$. The flow is always turbulent when entering the control area. The velocity field is measured $\approx 50D$ upstream from the downstream steel pipe. The measurement plane is parallel to the streamwise flow direction (pipe z–axis) and located in the center line of the pipe. The two velocity components within a plane of $\approx 3.5D$ length are measured using a high–speed 2D–PIV system (LaVision) with a full resolution of 2400×1900 px. The resulting spatial resolution is 56 vectors per D. The data rate is 100 Hz. Hollow glass spheres with a mean diameter of 13 μm are used for seeding. Around the measurement plane the pipe is encased by a small rectangular Perspex box ($50 \times 50 \times 350$ mm) filled with water such that the optical axis of the camera is

perpendicular to the air–water interface to reduce refraction and distortion of the images. A differential pressure sensor (DP 45, Validyne, full range of 550 Pa with an accuracy of ±0.5%) is mounted onto the movable Perspex pipe. Here the pressure drop Δp in the Perspex pipe is measured between two pressure taps (axial spacing 260 mm).

3.2.4   Numerical method

We solve the incompressible Navier–Stokes equations

$$\frac{\partial \boldsymbol{u}}{\partial t} + \boldsymbol{u} \cdot \boldsymbol{\nabla}\boldsymbol{u} = -\boldsymbol{\nabla}p + \frac{1}{Re}\Delta\boldsymbol{u}, \ \boldsymbol{\nabla} \cdot \boldsymbol{u} = 0 \tag{3.1}$$

in a straight circular pipe in cylindrical coordinates (r, θ, z), r, θ and z being the radial, azimuthal and axial coordinate respectively. Throughout this study, the flow is driven by a constant mass flux. In Eqs. (3.1) velocity is normalized by the mean velocity U and length by pipe diameter D. A Fourier–Fourier–finite difference code is used for the integration of the governing equations, with periodic boundary condition in the axial and azimuthal directions. In the radial direction a central finite difference scheme with a 9–point stencil is adopted. In this formulation, velocity can be expressed as

$$\boldsymbol{u}(r, \theta, z, t) = \sum_{k=-K}^{K} \sum_{m=-M}^{M} \hat{\boldsymbol{u}}_{k,m}(r, t)e^{(i\alpha kz+im\theta)} \tag{3.2}$$

where αk and m give wave numbers of the modes in axial and azimuthal direction respectively, $2\pi/\alpha$ gives the pipe length L_z, and $\hat{\boldsymbol{u}}_{k,m}$ is the complex Fourier coefficient of mode (k, m). The governing equations are integrated with a 2nd–order, semi–implicit time–stepping scheme, for details see Willis and Kerswell [2009]. The code has been verified and extensively used in many studies [Willis and Kerswell, 2009; Avila *et al.*, 2010; Barkley *et al.*, 2015].

In Table 3.1, we list the Reynolds numbers, pipe lengths and resolutions we considered in our simulations. To avoid significant domain size effect, the pipe lengths are selected to contain a few low–speed streaks, whose streamwise length is typically around 500 wall units in our normalization, see Jimenéz and Pinelli [1999].

The pipe length was doubled for $Re = 4000$ and $Re = 5000$ to verify that the pipe lenghs here in the table are sufficient. The resolutions are set to be able to sufficiently resolve the near wall structures, see reference grid sizes shown in the Table 1 of Jimenéz and Pinelli [1999]. Note that there is a difference of a factor of 2 in length scales between our normalization and theirs (double ours to compare with theirs).

3.3   Supplementary Information

3.3.1   Tables

$Re = \frac{UD}{\nu}$	$Re_\tau = \frac{u_\tau D}{\nu}$	$L_z(D)$	L_z^+	$\Delta r_{\min}^+$	$\Delta r_{\max}^+$	$(\Delta\theta D/2)^+$	Δz^+
4 000	282	12.6	3 553	0.046	2.6	7.0	7.0
5 000	342	12.6	4 309	0.056	3.2	8.4	8.4
10 000	628	6.3	3944	0.032	6.8	6.8	13.0
25 000	1 400	3.0	4 200	0.032	4.8	8.6	8.2
50 000	2 570	1.5	3854	0.020	5.0	10.2	10.0
100 000	4 714	0.8	3 772	0.016	6.2	9.6	9.8

Table 3.1: The Reynolds number Re, the friction Reynolds number $Re_\tau = u_\tau D/\nu$ ($u_\tau = \sqrt{\tau_w/\rho}$ is the friction velocity defined based on wall shear stress τ_w and density ρ), pipe length in diameter, pipe length in wall unit $L_z^+ = L_z u_\tau/\nu = L_z/D\, Re_\tau$, the smallest and maximum radial grid size $\Delta r_{\min}^+ = \Delta r_{\min}/D\, Re_\tau$, $\Delta r_{\max}^+ = \Delta r_{\max}/D\, Re_\tau$, azimuthal grid size at the pipe wall (maximum) $(\Delta\theta D/2)^+ = \Delta\theta/2\, Re_\tau$ and axial grid size $\Delta z^+ = \Delta z/D\, Re_\tau$ in wall units.

3.3.2   Figures

46
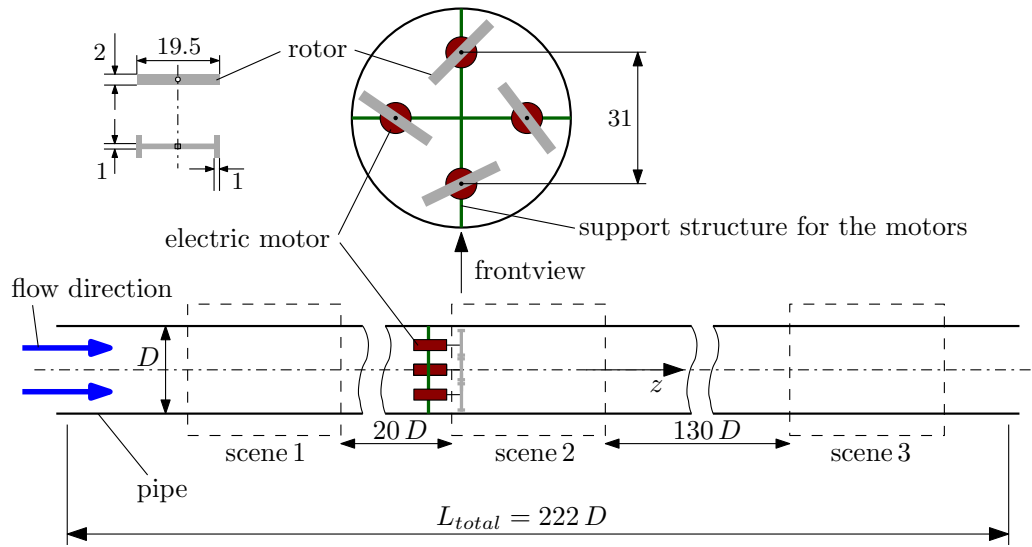
Figure 3.4: Sketch of the test facility used to perturb the flow with four rotors driven by four electric motors. The diameter of the PMMA pipe is $D = 54\,\text{mm}$. The flow direction is from left to right. Drawing not to scale. All dimensions in mm. The dashed rectangles indicate the locations of the scenes in the movie.
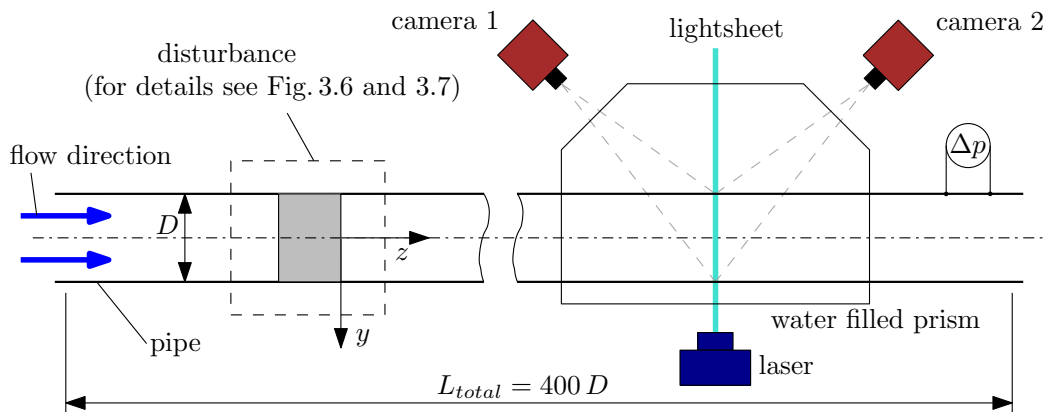
Figure 3.5: Sketch of the test facility used to disturb the flow with the wall–normal jet injection and the streamwise injection through an annular gap, see Supplementary Information Fig. 3.6 and Supplementary Information Fig. 3.7 for details. The diameter of the glass pipe is $D = 30\,\text{mm}$. The flow direction is from left to right. Drawing not to scale.
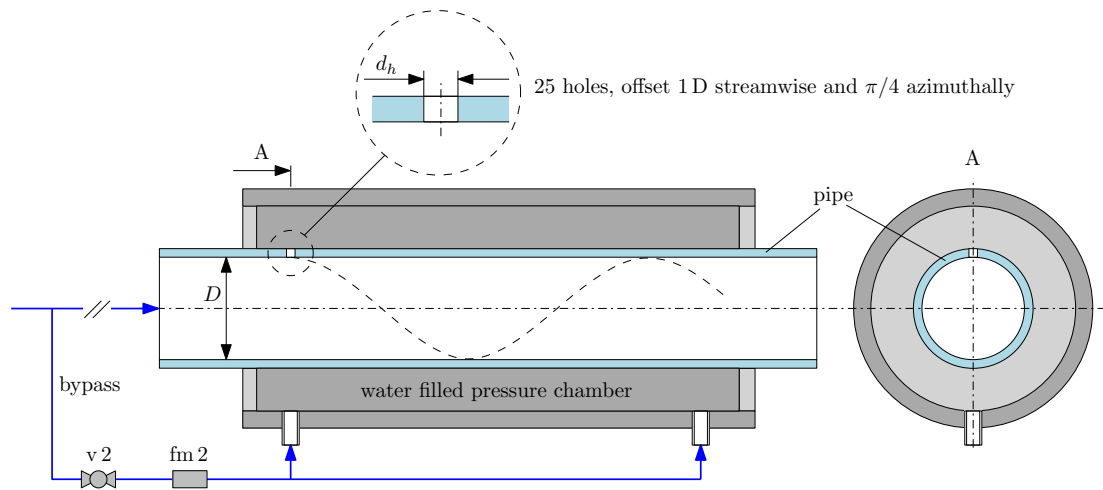
Figure 3.6: Device to inject wall–normal jets. Sketch of the device which allows to inject fluid into the main pipe through 25 small holes with diameter $d_h = 0.5\,\mathrm{mm}$. The holes are offset by $1\,D$ in the streamwise and $\pi/4$ in the azimuthal direction. The section where the pipe is perforated is made of Plexiglas and encased by a water–filled pressure chamber. To ensure uniform injection all the holes have been machined with a tolerance of 0.01 mm and are subjected to the same pressure, the latter guaranteed by the large volume of the water–filled encasing chamber. Fluid is taken from the main pipe via a bypass and then re–injected through the pressure chamber. The bypass is equipped with a valve (v 2) and a flow meter (fm 2) to precisely adjust and measure the injected flow such that the flow rate and hence the velocity of the resulting jets can be precisely adjusted and measured. At $Re = 3100$ and for a bypass ratio $\beta_J = 0.015$ the injection flow rate is $Q_J = 2.5\,\mathrm{ml/min}$ per single hole, corresponding to an injection velocity $U_J = Q_J/(\pi d_h^2/4) = 0.2$ m/s. The device is mounted within two pipe segments. The flow direction is from left to right. Drawing not to scale.
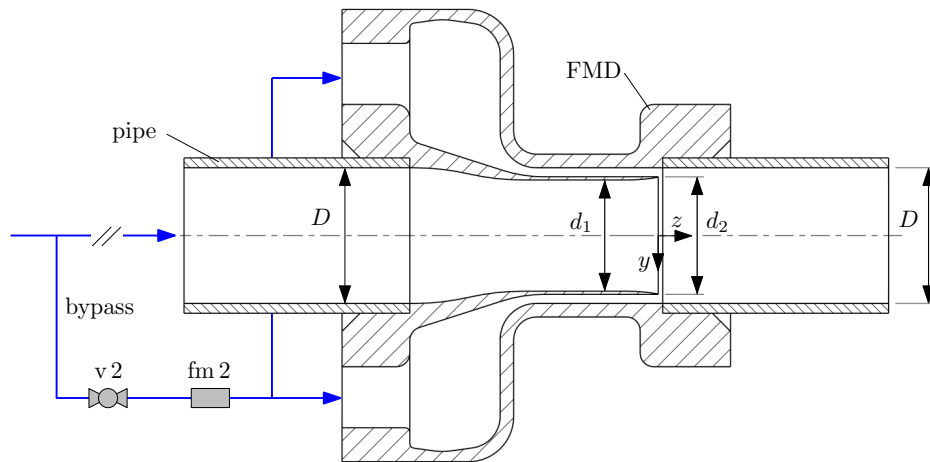
Figure 3.7: Device for streamwise injection through an annular gap. The device allows to inject fluid into the main pipe through a small annular concentric gap of 1 mm close to the pipe wall. The main pipe is slightly narrowed in a short range just upstream the injection point (d_1 = 26.6 mm, d_2 = 28 mm, open gap area A_1 = 91.1 mm^2). At a small backward facing step (z = 0, the plane of confluence) the fluid coming from the bypass is axially injected into the main pipe through an annular gap. The specified Reynolds number in the main pipe applies to the range upstream the bypass and downstream the confluence at z = 0. Fluid is taken from the main pipe via a bypass and then re–injected through a concentric gap close to the wall. The device is mounted within two pipe segments. The bypass is equipped with a valve (v 2) and a flow meter (fm 2) to precisely adjust and measure the injected flow through the gap. The flow direction is from left to right. Drawing not to scale. Patent pending.
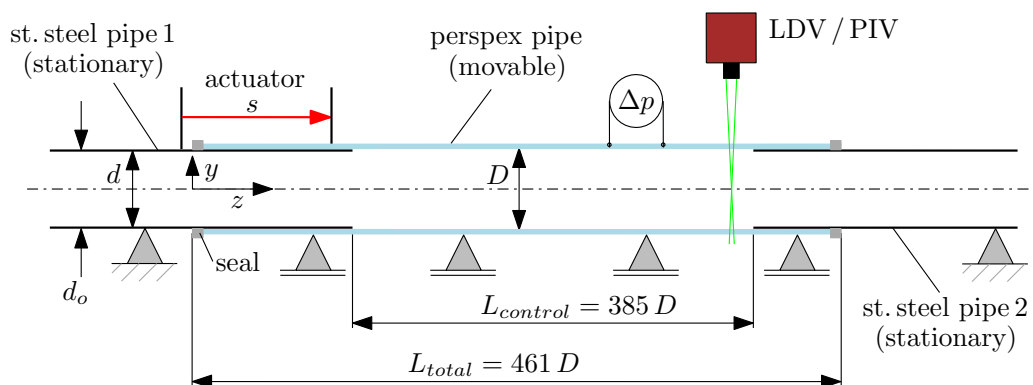
Figure 3.8: Sketch of the experimental setup with a moving pipe section. The flow direction is from left to right. A Perspex pipe is slipped over two stationary, very thin walled stainless steel pipes such that the Perspex pipe overlaps the steel pipes at the upstream and downstream end. The Perspex pipe is movable in the axial direction for an adjustable distance s. Drawing not to scale.
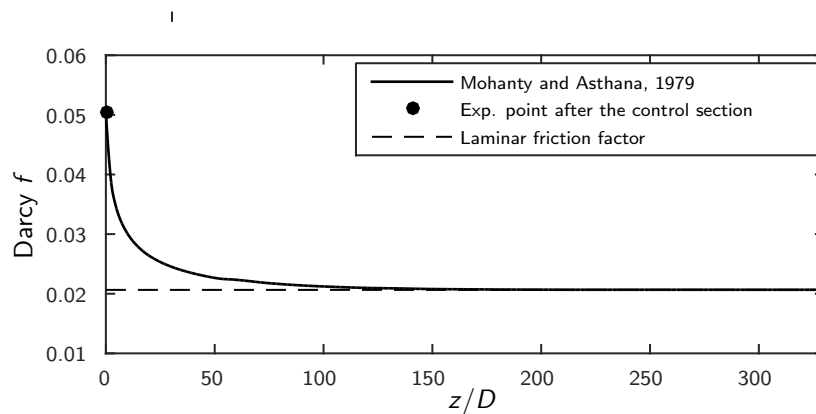
Figure 3.9: Darcy friction factor f as a function of the distance z/D from the control section in the wall–normal injection experiment. Starting from experimental data measured right downstream the jets section (solid dot), the spatial evolution of f is modeled after Mohanty and Asthana [1979]. The friction $f_R = 0.0221$ used to estimate the power dissipated in the remainder of the pipe is obtained by averaging f along $330D$. Note that f approaches quickly the laminar value (dashed line) and the flow can be considered fully developed to Hagen–Poiseuille after $\approx 140D$.
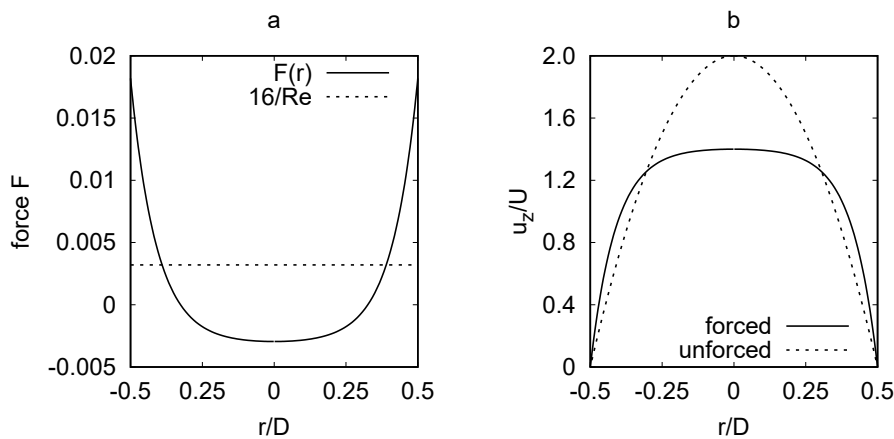
Figure 3.10: (a) The force $F(r)$ as a function of r at $Re = 5000$ given the parameter $\beta = 0.6$ (solid line). For comparison, the pressure gradient of the unforced laminar flow $\partial p/\partial z = 16/Re$ is given by the dashed line. (b) The forced (solid line) and the unforced (dashed line) velocity profile of the basic laminar flow. Note that in the forced flow case both the $F(r)$ and pressure gradient $16/Re$ shown in (a) are at work.
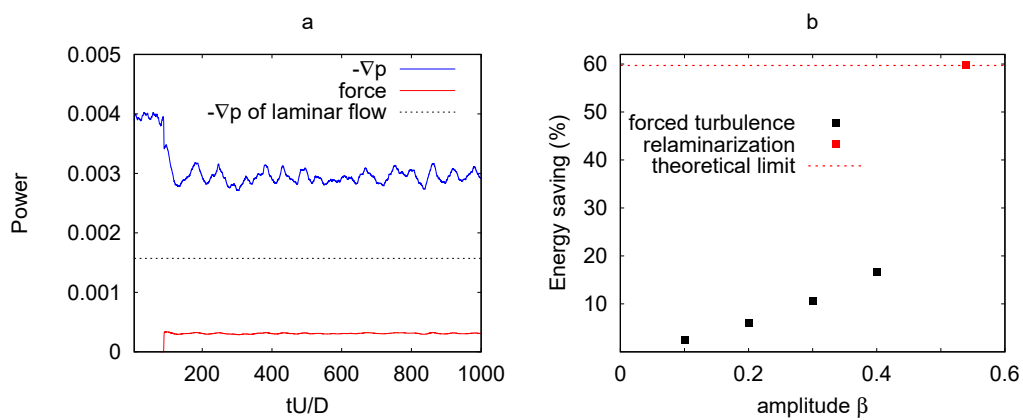
Figure 3.11: (a) The power signal of a forcing case at $Re = 4000$ with the parameter $\beta = 0.44$. The blue line is for the driving pressure gradient (see Supplementary Information Eq. (3.20)) and the red for the active forcing (see Supplementary Information Eq. (3.21)). The dashed line marks the power of the pressure gradient corresponding to laminar flow. Flow is initially fully turbulent and the force is turned on at $t = 100$. (b) Net energy saving as a function of the forcing amplitude β at $Re = 4000$. At sufficient forcing amplitude, turbulence collapses and the energy saving approaches the theoretical limit of 60% at this Reynolds number (red symbol and dashed lines).
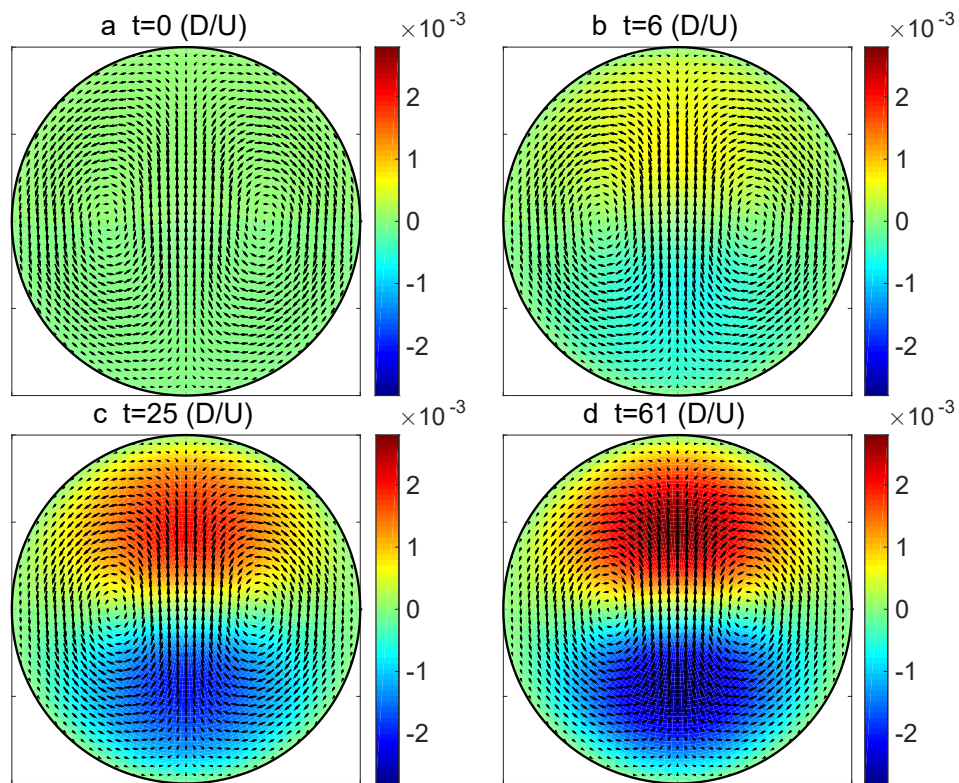
Figure 3.12: The generation of strong streaks by weak streamwise vortices due to the non–normality of the linearized flow. The calculation is at $Re = 5000$ with the parameter $\beta = 0.3$. The basic velocity profile is taken as the average velocity profile of the forced turbulent flow under this forcing parameter. A weak perturbation containing a pair of streamwise vortices (black arrows) is introduced to the flow and the growth of the streaks (colormap) are monitored (see the sequence of A—D). In the figure, the amplitude of the vortices (the maximum of the velocity component) is about 3×10^{-4}, which does not show significant change in all four panels. However, it generates strong streaks.
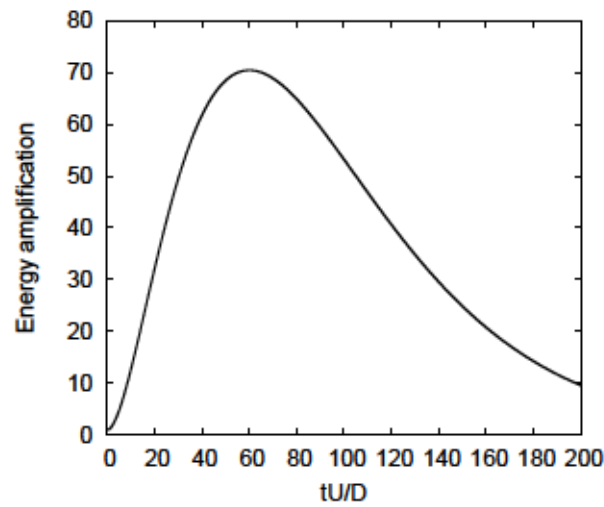
Figure 3.13: The transient amplification of energy of the flow (streaks) generated by the weak vortices as shown in Supplementary Information Fig. 3.12a. Large transient amplification can be reached before the disturbances eventually decay.
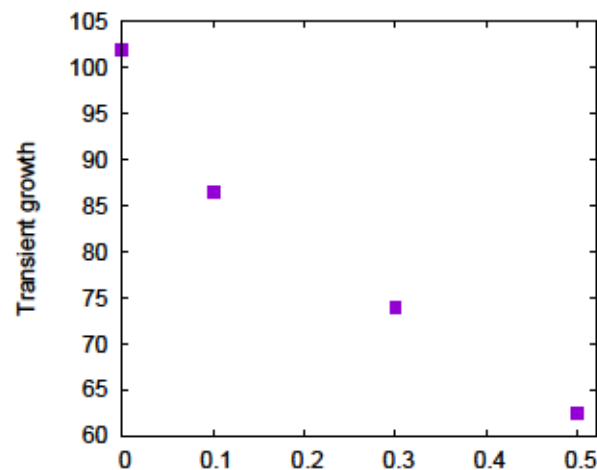
Figure 3.14: The transient growth of the forced turbulent mean velocity profile as the forcing parameter β increases. Clearly, as β increases, the transient growth decreases, *i.e.*, the streaks generated by weak vortices become weaker. When β surpasses about 0.5, turbulence tends to become localized and eventually relaminarizes as β increases further.
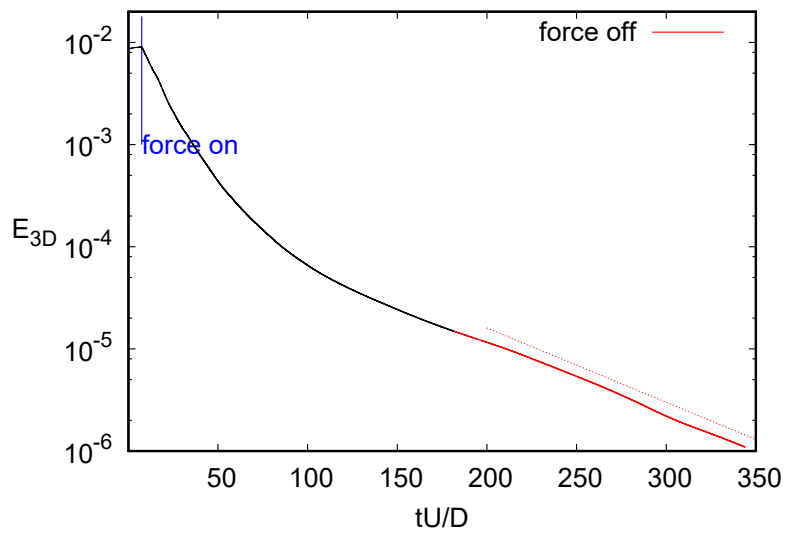
Figure 3.15: The kinetic energy of the 3–D turbulent fluctuations at Re = 50 000. Force $F(r)$ with $\beta = 0.98$ is turned on at $t = 7.5$ (marked by blue vertical line), and it is turned off at $t = 180$ and the kinetic energy after this point is shown as red line. The dotted red line indicates an exponential decay.
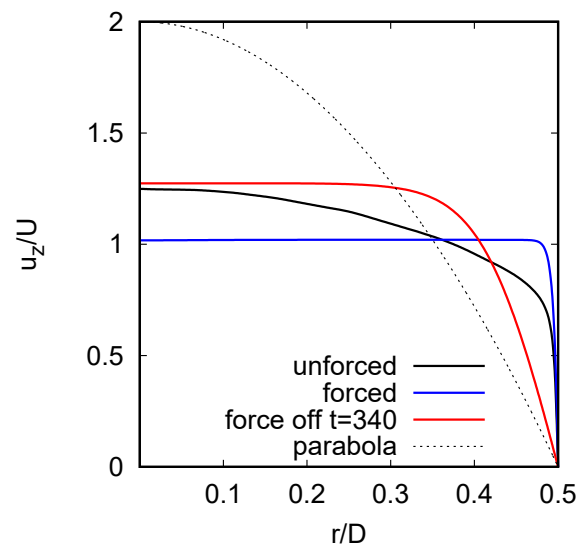
Figure 3.16: The velocity profile of the turbulence at Re = 50 000 as shown in Supplementary Information Fig. 3.15 at a few time instants. The black one is the velocity profile of a normal turbulence, the blue one is for the forced velocity profile at $t = 100$. The red one is the velocity profile at $t = 340$ after the force was switched off at $t = 180$. The dashed black line is the profile of the Hagen–Poiseuille flow.

54

3.3.3 Videos
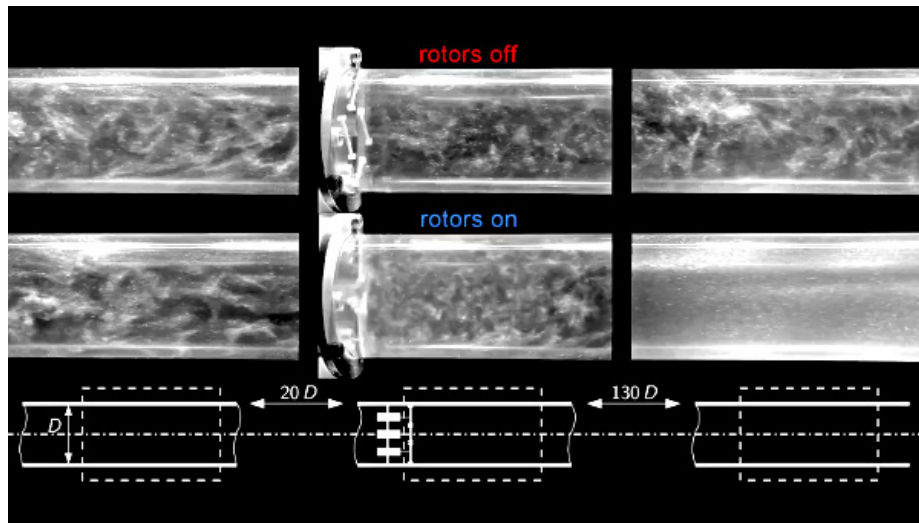
Figure 3.17: Supplementary Information, Video 1. Relaminarization by vigorously stirring a turbulent pipe flow with four rotors. Left column: turbulent pipe flow at $Re = 3500$ upstream of the actuation section ($20D$). Central column: the control section with rotors turned off and on. Right column: comparison of the flow downstream of the control section ($130D$). Video available online at https://doi.org/10.1038/s41567-017-0018-3.
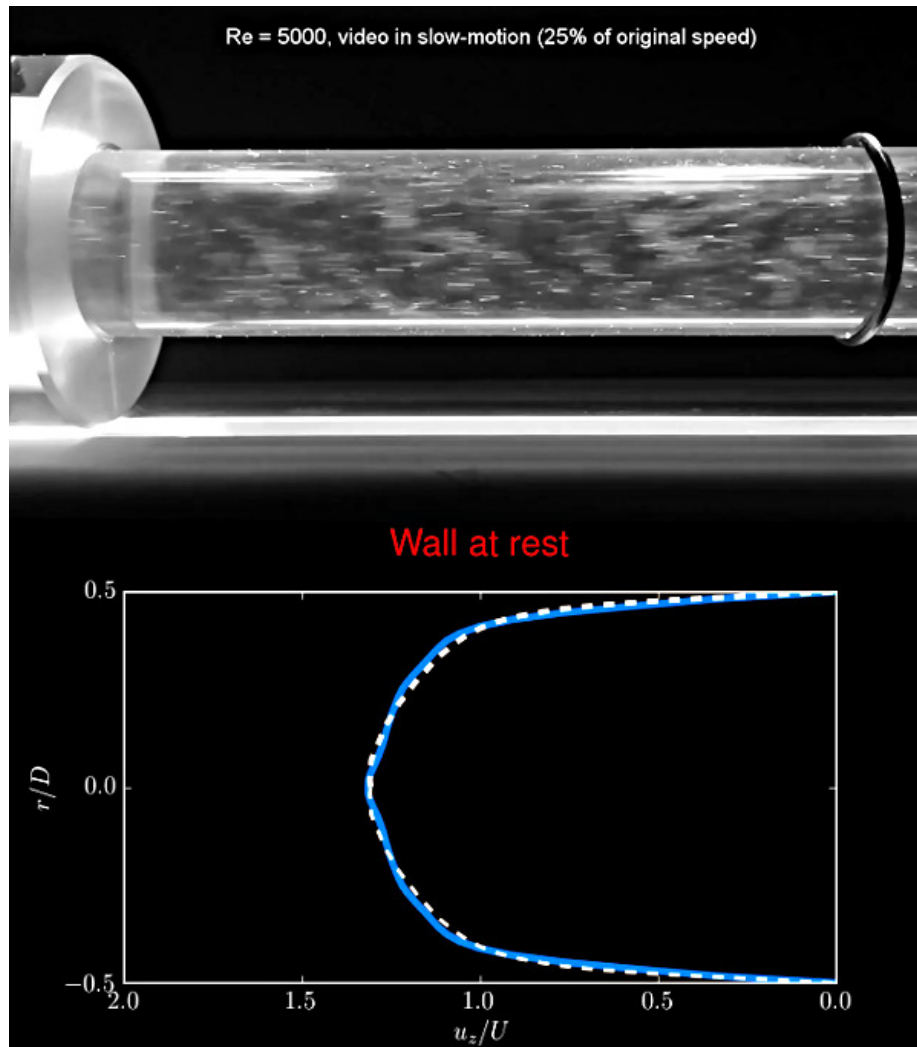
Figure 3.18: Supplementary Information, Video 2. Relaminarization by impulsive movement of a pipe segment. Top: The pipe wall is shifted in the axial direction for a length of 12D at $Re = 5000$. The movement is sufficient to initiate a full relaminarization which starts after the wall stops. Bottom: azimuthally averaged axial velocity as measured by means of PIV during the experiment (blue line) and turbulent reference profile (white, dashed line). Video available online at https://doi.org/10.1038/s41567-017-0018-3.

3.3.4 Energetic considerations

Wall–normal jets

We assume a fully–developed turbulent flow of density ρ at $Re = 3100$, with mean velocity U and Darcy friction factor [Pope, 2000] $f_T = 0.0439$. The pipe diameter is $D = 30$ mm, whereas the injection hole diameter is $D_J = 0.5$ mm. The injection ratio is $\beta_J = NQ_J/Q = 0.015$, where $N = 25$ and Q and Q_J are the main and single injection flow rates. We start by expressing the kinetic energy per unit time pumped by the jets into the flow,

$$\frac{N\Pi_J}{\frac{1}{2}\rho U^2 Q} = \frac{N\frac{1}{2}\rho U_J^2 Q_J}{\frac{1}{2}\rho U^2 Q} = \frac{\frac{1}{2}\rho U_J^2 \beta_J Q}{\frac{1}{2}\rho U^2 Q} = \frac{\beta_J^3}{N^2}\left(\frac{D}{D_J}\right)^4 = \frac{0.015^3}{25^2}\left(\frac{30}{0.5}\right)^4 = 0.07. \quad (3.3)$$

Note that powers throughout this section are normalized by $\frac{1}{2}\rho U^2 Q$. Next, in order to compute the power associated to the controlled flow, we subdivide our domain in a control and remainder section. The control section has a length of $L_C = 25\,D$ and it is characterized by a constant friction factor $f_C \approx 0.05$, estimated from the the velocity profile measured at the end of the jets section. The remainder length is $L_R = 330\,D$ with an average friction factor $f_R = 0.0221$, which is estimated by considering the evolution of the flow from plug–like to parabolic. More precisely, we average the friction over the pipe remainder by using the data provided by Mohanty and Asthana [1979], see Supplementary Information Fig. 3.9. The friction factor is found to be rather close to the laminar value, as the wall velocity gradient quickly recovers the laminar slope. We proceed by evaluating all the sources of power consumption. We have

$$\frac{\Pi_C}{\frac{1}{2}\rho U^2 Q} = \frac{L_C}{D}f_C = 25 \cdot 0.05 = 1.25, \quad (3.4)$$

$$\frac{\Pi_R}{\frac{1}{2}\rho U^2 Q} = \frac{L_R}{D}f_R = 330 \cdot 0.0221 = 7.29, \quad (3.5)$$

$$\frac{\Pi_T}{\frac{1}{2}\rho U^2 Q} = \frac{L_C + L_R}{D}f_T = (25 + 330) \cdot 0.0439 = 15.59, \quad (3.6)$$

where Π_C, Π_R, Π_T are the power dissipated in the control section, in the pipe remainder and in the whole pipe without control, respectively. The power difference with respect to the turbulent reference is

$$\frac{\Delta\Pi}{\frac{1}{2}\rho U^2 Q} = \frac{\Pi_T - (\Pi_C + \Pi_R + N\Pi_J)}{\frac{1}{2}\rho U^2 Q} = 15.59 - (1.25 + 7.29 + 0.07) = 6.98, \quad (3.7)$$

which implies a net saving if $\Delta\Pi > 0$. To quantify the efficiency of the control method we follow the same approach as in [Kasagi *et al.*, 2009a] and [Quadrio, 2011]. We compute the relative net power saving

$$S = \frac{\Delta\Pi}{\Pi_T} = \frac{6.98}{15.59} = 45\%, \quad (3.8)$$

and the control cost normalized by the power gain,

$$\frac{1}{G} = \frac{N\Pi_J}{\Pi_T - (\Pi_C + \Pi_R)} = \frac{0.07}{15.59 - (1.25 + 7.29)} = 1\%, \quad (3.9)$$

which also represents the minimum actuator efficiency required to have $S > 0$. As a final remark, it is possible to estimate the minimum remainder length that ensures a positive net gain. By repeating the estimate of S for smaller values of the remainder length we find

$$L_R|_{S=0} \approx 25D.$$

Finally, we assess the actual energy saving in the experiment where further losses are encountered due to the actuator limited efficiency. The pressure required for the jet injection through the simple and not optimized actuation device amounts to $\Delta P_D = 680\,\mathrm{Pa}$ at a flow rate $NQ_J = 0.06\,\mathrm{l/min}$. The corresponding non–dimensional dissipated power is

$$\frac{\Pi_D}{\frac{1}{2}\rho U^2 Q} = \frac{\Delta P_D N Q_J}{\frac{1}{2}\rho U^2 Q} = 2.15, \quad (3.10)$$

and consequently, the energy saving for the real setup results

$$S^* = \frac{\Pi_T - (\Pi_C + \Pi_R + \Pi_D)}{\Pi_T} = 31\%. \quad (3.11)$$

Streamwise injection

Similarly to the wall–normal jets case, we estimate the efficiency of the streamwise injection device. To this end, we assume a fully–developed turbulent flow of density

ρ at $Re = 5000$, with mean velocity U and Darcy friction factor $f_T = 0.0377$. The remainder length is $L_R = 330\,D$ with an average friction factor $f_R = 0.0143$, estimated in the same way described in the previous section. The ratio between the area from which the fluid is injected and the total area is $\beta_A = 0.13$, while the injection ratio is $\beta_Q = Q_J/Q = 0.18$. The kinetic energy per unit time introduced by the annular jet into the flow can be estimated as

$$\frac{\Pi_I}{\frac{1}{2}\rho U^2 Q} = \frac{\frac{1}{2}\rho U_I^2 Q_I}{\frac{1}{2}\rho U^2 Q} = \frac{\beta_Q^3}{\beta_A^2} = \frac{0.18^3}{0.13^2} = 0.345. \tag{3.12}$$

An additional pressure loss due to the area contraction inside the injection device is modeled as

$$\frac{\Pi_L}{\frac{1}{2}\rho U^2 Q} = K = 0.5, \tag{3.13}$$

where K is chosen conservatively. The power dissipated in the remainder section with and without control is respectively,

$$\frac{\Pi_R}{\frac{1}{2}\rho U^2 Q} = \frac{L_R}{D} f_R = 330 \cdot 0.0143 = 4.72, \tag{3.14}$$

$$\frac{\Pi_T}{\frac{1}{2}\rho U^2 Q} = \frac{L_R}{D} f_T = 330 \cdot 0.0377 = 12.44. \tag{3.15}$$

The power difference with respect to the turbulent reference is

$$\frac{\Delta\Pi}{\frac{1}{2}\rho U^2 Q} = \frac{\Pi_T - (\Pi_R + \Pi_L + \Pi_I)}{\frac{1}{2}\rho U^2 Q} = 12.44 - (4.72 + 0.5 + 0.345) = 6.88. \tag{3.16}$$

Consequently, the relative net power saving and control cost normalized by the power gain are respectively

$$S = \frac{\Delta\Pi}{\Pi_T} = \frac{6.88}{12.44} = 55\%, \tag{3.17}$$

and

$$\frac{1}{G} = \frac{\Pi_I}{\Pi_T - (\Pi_R + \Pi_L)} = \frac{0.345}{12.44 - (4.72 + 0.5)} = 5\%. \tag{3.18}$$

Finally, the minimum remainder length that allows a positive net power saving is estimated to be

$$L_R|_{S=0} \approx 47D.$$

3.3.5   Forcing the flow

To implement our control technique, *i.e.*, to deform the velocity profile, an external force term $\boldsymbol{F} = F(r)\hat{z}$ is introduced to the Navier–Stokes equations. This force decelerates the flow near the pipe center and accelerates the flow near the pipe wall while keeping the mass flux unchanged. As a result the velocity profile is deformed on average to a more plug–like one compared to the parabola $\boldsymbol{U} = (2 - 8r^2)\hat{z}$ in the unforced situation. This forcing technique in essence is the same as in Hof *et al.* [2010], however a different functional form was chosen for the forcing in order to control fully turbulent flow. In this study, the force is such that it generates a velocity profile in laminar flow given by

$$\boldsymbol{u}(\beta, r) = (2 - \beta)(1 - \frac{\cosh{(2cr)} - 1}{\cosh{(c)} - 1})\hat{z} \tag{3.19}$$

where β is the decrease of the center line velocity compared to the parabola and will be taken as a measure of the forcing amplitude. c is a parameter to assure the constant mass flux. The body force $\boldsymbol{F}$ is solved inversely given the target profile. As an example, a force and the resulting velocity profile at $Re = 5000$ with the force parameter $\beta = 0.6$ is shown in Supplementary Information Fig. 3.10. As shown, the body force is negative, *i.e.*, acting upstream near the pipe center, slowing down the flow, and is the other way around near the pipe wall.

Subsequently, this body force will be imposed globally on top of fully turbulent flows. At high Reynolds numbers (above 3000), we observed that turbulence indeed decays and the flow relaminarizes given sufficient force, as shown in Fig. 3.2b in the main text and in Supplementary Information Fig. 3.15 at $Re = 50\,000$ where the flow is forced with the force parameter $\beta = 0.98$. At this Re, the friction drops by a factor of 16 after the flow relaminarizes and the velocity profile recovers towards the parabolic Hagen–Poiseuille profile. The same control was tested up to $Re = 100\,000$ in our simulations and relaminarization was also obtained given sufficiently strong force.

Our simulations also show that an energy saving is immediately achieved when the force is activated, even if flow stays turbulent under the forcing. To illustrate this point, forces with several different amplitudes are tested at $Re = 4000$ and the

results are shown in Supplementary Information Fig. 3.11. The energy consumption is calculated as the the power of the driving pressure gradient and the controlling force per unit volume (power density) as

$$P_\mathrm{p} = \frac{\int_V (-\nabla p \cdot \boldsymbol{u}) dV}{V} \tag{3.20}$$

and

$$P_\mathrm{F} = \frac{\int_V (\boldsymbol{F} \cdot \boldsymbol{u}) dV}{V}. \tag{3.21}$$

The integration is performed over the whole computational domain V. Note that the driving pressure gradient is spatially invariant and the controlling force is only radially dependent, therefore, these two forces only do work on the mean flow. The energy consumption due to the enhanced skin friction (flattened velocity profile) under the forcing is accounted for by the energy consumption of the controlling force. Consequently the energy saving is defined as

$$S = \frac{P_\mathrm{p,\ unforced} - P_\mathrm{p,\ forced} - P_\mathrm{F}}{P_\mathrm{p,\ unforced}}. \tag{3.22}$$

The time series of the energy consumption of an example at $Re = 4000$ for the driving pressure gradient and for the active forcing are shown in Supplementary Information Fig. 3.11a. We can see that, upon activating the forcing at $t = 100$, the decrease in the driving pressure gradient (energy gain) outweighs the energy consumption of the forcing (energy loss), meaning a net energy saving, though turbulence remains at a lower level under the forcing. The energy saving also increases with a stronger forcing, as shown in Supplementary Information Fig. 3.11b.

3.3.6 The lift–up mechanism

To better understand why turbulence decays in the presence of a disturbance/forcing that flattens the velocity profile we consider how the profile shape influences the lift–up mechanism. This mechanism is a major energy growth mechanism in shear flows and is responsible for the transition to turbulence in linearly stable shear flows (see a recent review by Brandt [2014]). It has been shown that, for inviscid

flow, streamwise invariant cross–flow disturbances, such as streamwise rolls, do not decay and thus continually convect the mean shear (*i.e.* $u_r \frac{\partial U_z(r)}{\partial r}$) and redistribute the streamwise momentum, generating strong low/high speed streamwise streaks. The strongly distorted velocity profile becomes susceptible to other instabilities which generate 3–D turbulent fluctuations via nonlinear interaction [Hamilton *et al.*, 1995]. Theoretical argument of Landahl [1980] showed that the disturbance kinetic energy grows at least linearly with time in inviscid flows. This energy growth will be limited by the viscosity in viscous flows, however, only at large times. On the other hand, the lift–up ($u_r \frac{\partial U_z(r)}{\partial r}$) directly enters the turbulence production term in the equations for the kinetic energy of turbulent fluctuations [Song *et al.*, 2017].

Supplementary Information Fig. 3.12 illustrates the lift–up exhibited by a vortex pair imposed on the mean turbulent flow profile. The vortices redistribute the shear and lift up slow fluid (blue) from the wall and replace it by faster fluid (red) from the central part of the pipe. The initial perturbation (consisting of the vortex pair) is strongly amplified as it is transformed into streaks. To obtain a measure of this amplification mechanism we consider the linearized Navier–Stokes equations and perform a transient growth (TG) analysis (following the analysis of Butler and Farrel [1993] and the algorithm by Meseguer and Trefethen [2003]). As the forced mean turbulent velocity profile is linearly stable small perturbations to the linearized equations must eventually decay. However disturbances of the form shown in Supplementary Information Fig. 3.12a will experience significant growth for some transient period (during lift–up) before they eventually decay (Supplementary Information Fig. 3.13). For the case shown the initial disturbance energy is amplified by a factor 70, *i.e.* the eventual streaks have a 70 times larger energy than the initial vortices. We next probe how TG is affected for the forced profiles. As shown in Supplementary Information Fig. 3.14, as the forcing amplitude is increased TG continuously decreases, *i.e.* by flattening the velocity profile the vortex streak interaction becomes less efficient. At a forcing amplitude of about $\beta = 0.60$ turbulence decays and the flow relaminarizes.

The same procedure has been applied to the experimental flows: starting from the measured averaged velocity profile and assuming that the profile is fixed under

the influence of the disturbance, we conducted a TG analysis around this modified profile. As shown in Fig. 2d in the main text the TG of profiles the disturbed profiles is indeed reduced considerably, suggesting that vortices are less efficient in producing streaks. Hence the energy growth via the lift–up mechanism is clearly subdued. As also illustrated in Fig. 2d the collapse of turbulence in the experiments happens at comparable TG values as the ones found in the simulations for identical Re.

3.3.7   Removing the force

As shown in Supplementary Information Fig. 3.15, turbulence keeps decaying while a sufficient forcing is applied (black line after the vertical blue line). Under the forcing, turbulence continually decays and will eventually disappear. Clearly, the active forcing is consuming energy, manifesting higher shear at the wall than the ideal Hagen–Poiseuille flow (see Supplementary Information Fig. 3.10b), and it is not optimal if the force is always kept on. Thanks to the subcriticality of the laminar pipe flow, only perturbations above certain finite amplitudes can trigger turbulence, the force can be switched off once the tubrulent velocity fluctuations decayed below the critical value. After that, turbulence cannot recover even if the force is switched off. Here in the figure we show that after a sufficient control time (about 170 D/U in this simulation), turbulence indeed keeps decaying when the force is removed (see the red solid line after about $t = 180$). Eventually the kinetic energy enters an exponential decay regime, which is the signature of a linear process. We did not continue the simulation due to the very high computational cost at this high Reynolds number. However, turbulence is not expected to recover in this linear regime.

Supplementary Information Fig. 3.16 shows the velocity profile at some time instants. The black line is the averaged velocity profile of a normal unforced turbulence at Re=50 000. When the force is turned on at $t = 7.5$, the velocity profile is quickly flattened into a plug–like one as the blue line shows. After the force is switched off at $t = 180$, the velocity profile starts to recover towards the parabolic

profile of the Hagen–Poiseuille flow because turbulent fluctuations are nearly extinct. However, this recovery is a long asymptotic process and roughly takes hundreds of convective time units. The red line shows the velocity profile during this recovery process at $t = 340$.

---

4 Relaminarization by steady modification of the streamwise velocity profile in a pipe

We show that a rather simple, steady modification of the streamwise velocity profile in a pipe can lead to a complete collapse of turbulence and the flow fully relaminarizes. Two different devices, a stationary obstacle (inset) and a device to inject additional fluid through an annular gap close to the wall, are used to control the flow. Both devices modify the streamwise velocity profile such that the flow in the center of the pipe is decelerated and the flow in the near wall region is accelerated. We present measurements with stereoscopic particle image velocimetry to investigate and capture the development of the relaminarizing flow downstream these devices and the specific circumstances responsible for relaminarization. We find total relaminarization up to Reynolds numbers of 6000, where the pressure drop in the downstream distance is reduced by a factor of 3.4 due to relaminarization. In a smooth straight pipe the flow remains completely laminar downstream of the control. Furthermore, we show that transient (temporary) relaminarization in a spatially confined region right downstream the devices occurs also at much higher Reynolds numbers, accompanied by a significant drag reduction. The underlying physical mechanism of relaminarization is attributed to a weakening of the near–wall turbulence production cycle.

4.1 Introduction

The control of turbulence to reduce skin friction is of great interest in a wide variety of technological applications, as frictional drag is a heavy consumer of energy and thus a possibly avoidable source of significant operating costs and massive carbon emissions. Numerous techniques for the control of turbulent flows have been proposed over the years. However, only a few methods of control have already been successfully implemented in practical engineering devices.

Flow control is commonly classified as either active or passive depending on whether or not external energy input is required [Gad-el-Hak, 2000]. The most sophisticated, and on a theoretical basis most elegant method, is active feedback (closed–loop) control of turbulence (see *e.g.* [Moin and Bewley, 1994; Lumley and Blossey, 1998; Kim and Bewley, 2007; Kasagi *et al.*, 2009b; Sharma *et al.*, 2011; McKeon *et al.*, 2013]). However, the practical implementation is technically highly demanding and expensive due to the required sensors for realtime flow measurements and elaborate actuators to control the flow. Predetermined (open–loop) active techniques are usually characterized by greater simplicity and comparative ease of implementation. Among such techniques, modifying the flow through large–scale, spanwise forcing created by boundary motion (wall oscillation or transverse traveling wave excitation) or a body force has produced promising results (see *e.g.* [Karniadakis and Choi, 2003; Quadrio *et al.*, 2009; Auteri *et al.*, 2010; Nakanishi *et al.*, 2012; Tomiyama and Fukagata, 2013; Rabin *et al.*, 2014]).

The wide range of passive control techniques comprises diverse approaches such as surface modifications by means of *e.g.* riblets [Garcia-Mayoral and Jiménez, 2011], grooves [Frohnapfel *et al.*, 2007], shark skin surfaces [Dean and Bhushan, 2010], hydrophobic walls [Watanabe *et al.*, 1999; Rothstein, 2010] or by forcing small optimal perturbations [Fransson *et al.*, 2006]. Furthermore, modifications of the fluid employing polymer additives [White and Mungal, 2008; Choueiri *et al.*, 2017] and modifications of the flow field by means of honeycombs and screens [Lumley and McMahon, 1967; Laws and Livesey, 1978].

Most of the above mentioned methods have in common that they reduce skin

friction and decrease the turbulence level by some amount in the control area but can not totally extinguish turbulence and have no effect further downstream. However, the ultimate goal of turbulence control in terms of energy saving is relaminarization (also denoted as turbulent–laminar transition, reversion, retransition, and laminarization) of the flow, leaving aside the discussion on possible sublaminar friction in duct flows [Bewley, 2009; Fukagata *et al.*, 2009].

Occasional evidence of relaminarization not determined by dissipation and the Reynolds number has been found when a turbulent flow is subjected to effects of acceleration, suction, blowing, magnetic fields, stratification, rotation, curvature and heating [Sreenivasan, 1982]. For example, a peculiarity of curved pipes is that the threshold for the onset of subcritical turbulence is postponed and occurs at Reynolds numbers considerably larger than in straight pipes. As a consequence, low Reynolds number turbulent flows emerging from a straight pipe may relaminarize in a subsequent curved pipe [Sreenivasan and Strykowski, 1983; Kühnen *et al.*, 2015a].

In particular, the effect of a favorable pressure gradient (FPG) on a boundary layer and the related case of accelerated pipe flow have received considerable attention concerning relaminarization. In accelerated pipe flow, *i.e.* during and subsequent to a rapid increase of the flow rate of an initially turbulent flow, the flow has been observed to transiently first visit a quasi–laminar state and then again undergo a process of transition that resembles the laminar–turbulent transition (see *e.g.* [Greenblatt and Moss, 1999; Greenblatt and Moss, 2004]; see also [He and Seddighi, 2013; He and Seddighi, 2015] for accelerated flow in a channel). And a strong FPG imposed on a boundary layer has been found to have a damping effect on the growth of perturbations [Corbett and Bottaro, 2000] and to cause a temporary state of relaminarization (see *e.g.* [Patel and Head, 1968; Blackwelder and Kovasznay, 1972; Narasimha and Sreenivasan, 1973; Spalart, 1986; Warnack and Fernholz, 1998; Ichimiya *et al.*, 1998; Mukund *et al.*, 2006; Bourassa and Thomas, 2009]). In experiments, the FPG is usually imposed on the flow by means of various types of convergence in wind tunnels, but can also appear at a heated wall in a setting with a buoyancy–aided mixed convection (see *e.g.* [Jackson *et al.*, 1989] and references

therein). Closely related, *e.g.* Modi [1997] successfully employs a "moving surface boundary layer control" to prevent or delay the separation of the boundary layer from the wall, where the moving surface is provided by rotating cylinders. Regarding pipe flow, Pennell *et al.* [1972] observed temporary relaminarization by fluid injected through a porous wall segment of the pipe. All these authors showed that a wall–bounded turbulent shear flow may relaminarize or, more accurately, transiently tend to a laminar–like or quasi–laminar state under certain suitable conditions, even if the Reynolds number is above criticality. However, in all cases inevitable retransition to turbulence was found at a later stage, rendering the use of the word relaminarization somehow misleading as it characterizes an intermediate but not the final result. Although various parameters have been proposed to quantify the acceleration level needed for relaminarization (for a compilation see [Bourassa and Thomas, 2009]), there is neither agreement on a precise criterion for the occurrence of relaminarization and how it can be triggered, nor on how its onset may be recognized.

Profound understanding of ways to control turbulence has emerged from studies elucidating the near–wall flow dynamics. Obviously, the near–wall region is crucial to the dynamics of attached shear flows, as it is the region of the highest rate of turbulent energy production and of the maximum turbulent intensities. The dominant structures of the near–wall region are the streamwise velocity streaks and the quasi–streamwise vortices, and the dominant dynamics is a cyclic process characterized by the formation of velocity streaks from the advection of the mean profile by streamwise vortices, and the generation of vortices from the instability of the streaks, also referred to as self–sustaining process (see *e.g.* [Hamilton *et al.*, 1995; Waleffe, 1997; Jiménez, 2013; Brandt, 2014]). By clever use of "wrong physics" for numerical experiments on modified turbulent channels, Jimenéz and Pinelli [1999] showed that a local cycle of turbulence regeneration exists in the near wall region, which is independent of the outer flow. By numerically interrupting the cycle at various places they observed a breakdown of turbulence and eventual relaminarization. Also the aforementioned riblets are believed to directly weaken the quasi–streamwise vortices of turbulence regeneration, *i.e.* proposing that the

drag reduction by riblets is due to the weakening of these vortices by the increase in spanwise friction at the wall [Jiménez, 1994].

Turbulence arises from finite amplitude perturbations. At the lowest Reynolds numbers where turbulence can be observed (given a large enough initial perturbation), it does so in the form of localized structures called puffs which have a constant length and advect along the pipe [Wygnanski and Champagne, 1973; Mukund and Hof, 2018]. Hof *et al.* [2010] observed an immediate collapse of single turbulent spots in the intermittent regime at relatively low Reynolds numbers if two puffs were triggered too close to each other. They related the breakdown to a flattened streamwise velocity profile induced by the trailing puff, weakening the turbulence regeneration cycle beyond recovery. Their observation is also in qualitative agreement with predictions from a model explaining the emergence of fully turbulent flow in pipes and rectangular ducts [Barkley *et al.*, 2015]. From this model it was inferred that the excitability to the turbulent state only depends on the streamwise velocity component and hence an appropriate manipulation of the streamwise velocity profile may destroy the turbulent state.

Further investigations by Kühnen *et al.* [2018c] have recently shown that a modification of the velocity profile in a pipe by several means can lead to a complete collapse of turbulence and the flow can be forced to fully relaminarize also at higher Reynolds numbers. The annihilation of turbulence was achieved by a steady, active, open–loop manipulation of the streamwise velocity component alone, greatly simplifying control efforts. In their numerical simulations Kühnen *et al.* [2018c] added an appropriate radially dependent body force term, $F(r)$, to the equation of motion, modifying the streamwise velocity profile to a more plug–like one. Furthermore, they presented four different experimental techniques to modify the velocity profile of turbulent flow, such that the resulting profile was (more) plug–shaped and flat or even had velocity overshoots in the near wall region of the pipe. The first technique employed four rotors located inside the pipe to vigorously stir the flow. The second technique used wall–normal injection of additional fluid through 25 small holes placed consecutively in a helical fashion around the pipe. The third technique was by injecting fluid through an annular gap at the wall

to accelerate the flow close to the wall. The fourth approach was by means of a movable pipe segment which was used to locally accelerate the flow at the wall. In all cases turbulence was shown to decay and the flow eventually relaminarized completely, up to Reynolds numbers of 100 000 in DNS and 40 000 in experiments. The experiments demonstrated that relaminarization occurred as a direct result of a particular velocity and shear stress distribution especially in the wall region. The modified profile was shown to specifically suppress transient growth such that vortices do not efficiently create streaks.

Pipes and pipelines are central for the distribution of fluids throughout society, ranging from small diameter tubes in domestic settings to pipes in industrial plants and to large scale pipelines. The overall pumping costs surmount to billions of Euros per year and the frictional losses encountered in these flows are responsible for a significant part of the global energy consumption. Thus a huge amount of energy (pumping power due to frictional drag) could be saved if flows in pipes were laminar instead of turbulent. Pipe flow has a property that makes it particularly attractive for a way of turbulence control which totally extinguishes turbulence and establishes a laminar flow: the laminar state is stable to infinitesimal perturbations at all flow speeds [Drazin and Reid, 2004]. Consequently, once relaminarization is achieved, the flow will remain laminar provided that the pipe is straight and smooth. Turbulence will only return if a sufficiently strong disturbance is encountered. It is therefore not necessary to apply relaminarization control techniques throughout the pipe but instead it suffices to implement control stations at fixed locations (for example behind bends) to ensure laminar flow in the straight downstream pipe sections.

In the present investigation we want to further explore the effect, scope and consequences of a modified streamwise velocity profile which relaminarizes the flow. In order to do so we insert an obstacle partially blocking the pipe (method 1) and inject fluid through an annular gap at the wall (method 2). Both approaches force the streamwise velocity profile in a similar manner. The inserted obstacle is a purely passive means, while the injection device can be considered as steady, open–loop forcing. The obstacle device is better suited for measurements of the downstream

flow field at various distances, as it can be easily mounted at any arbitrary position within the pipe. The device to inject fluid through an annular gap is better suited to continuously vary the amount of acceleration close to the wall and fathom out the maximum Reynolds number where relaminarization is possible. We present measurements with stereoscopic particle image velocimetry and investigate the development of the flow downstream these devices. Furthermore we try to elucidate the specific circumstances responsible for relaminarization. Both devices are solely used for demonstration and proof–of–principle purposes. Detailed considerations on a possible net energy gain achievable with such devices are beyond the scope of the present manuscript.

The outline of the paper is as follows. In the next section we describe the experimental facility and the devices used to control the flow. Selected results of our extensive investigations and measurements are presented in section 4.3. In section 4.4 we discuss the results and compare them to previous investigations concerned with relaminarization.

4.2   Experimental facility

The experimental setup consists of a basic pipe flow facility constituting fully turbulent flow in a straight long glass pipe and two different kinds of interchangeable stationary flow management devices (FMDs) to control the flow. In the following section the facility and the different FMDs are described in detail.

4.2.1   Facility

The setup consists mainly of a glass pipe with inner diameter $D = 30 \pm 0.01$ mm and a total length of 9 m ($300\,D$) made of 1 meter sections. Fig. 4.1 shows a sketch of the facility. Gravity driven water enters the pipe from a reservoir. The flow rate Q_m is measured by means of an electromagnetic flowmeter (fm 1) in the supply pipe. The Reynolds number ($Re = UD/\nu$, where U is the mean velocity and ν the kinematic viscosity of the fluid) can be adjusted by means of a valve (v 1) in the supply pipe.
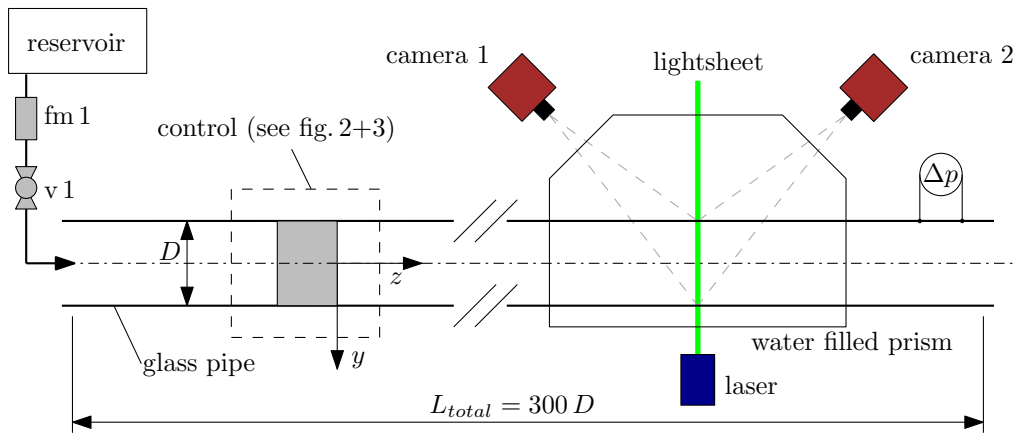
Figure 4.1: Sketch of the experimental facility used to control turbulent pipe flow with two different kinds of devices. Stereoscopic PIV measurements of the flow field are made downstream of the devices (see Figs. 4.2 and 4.3 for details). The flow direction is from left to right. Drawing not to scale.

The velocity vector field is measured $\approx 250\,D$ downstream from the inlet at the position of the lightsheet. The measurement plane is perpendicular to the streamwise flow direction (pipe $z-$axis). All three velocity components within the plane are recorded using a high–speed stereo PIV system (Lavision GmbH) consisting of a continuous laser (Fingco 532H-2W) and two Phantom V10 high–speed cameras with a full resolution of $2400 \times 1900\,\mathrm{px}$. Spherical glass particles (sphericel, mean diameter $13\,\mu\mathrm{m}$, Potter Industries) are used to seed the flow. Around the measurement plane the pipe is encased by a water filled prism such that the optical axes of the cameras are perpendicular to the air–water interface to reduce refraction and distortion of the images.

A differential pressure sensor (DP 103, Validyne) is used to measure the pressure drop Δp between two pressure taps. It is used for a straightforward detection of the flow state based on the large difference between turbulent and laminar friction factors (f_T and f_L). For this purpose the sensor is placed downstream the FMD as indicated in Fig. 4.1, and the pressure taps are separated by $30\,D$ in the streamwise direction.

For reference, a non–dimensional Cartesian coordinate system $(x, y, z) = (\tilde{x}/D, \tilde{y}/D, \tilde{z}/D)$ is used as indicated in Fig. 4.1. The origin of the coordinate system is always located at the downstream end of the FMD. The respective Cartesian velocity

components $(\tilde{u}, \tilde{v}, \tilde{w})$ are made non–dimensional either with the mean velocity U, yielding (u, v, w), or with the friction velocity w_τ, yielding y^+ and w^+. To calculate w_τ we use the estimate $w_\tau = U(f/8)^{0.5}$ [Pope, 2000], where the friction factor f is obtained from pressure drop measurements. Velocity fluctuations are denoted by ′, <> denotes cross sectional averaging and a bar averaging over time.

4.2.2   Orifice plate obstacle (method 1)

The first device to control the flow is a stationary obstacle or inset which can be mounted within the pipe. Fig. 4.2 shows a sketch of the device. It is made of a custom made, thin–walled tube of $L_{tot} = 200$ mm total length with an outer diameter of $d_1 = 28$ mm and an inner diameter of $d_2 = 26$ mm. To facilitate flow visualization the tube is made of Plexiglass. The tube is closed at the upstream end with a perforated plate with a wall thickness of $L_1 = 5$ mm. 7 holes with diameter $d_3 = 3.3$ mm are drilled into that plate. The device can be mounted concentrically within the pipe at any axial position by means of three small streamwise ribs (interference fit). As a result 78.6% of the pipe is blocked at the upstream end of the device. The flow is divided into two separate parts. One part of the flow goes through the 1 mm annular gap along the pipe wall, while the other part of the flow goes through the perforated plate in the bulk. The device thus forms a deliberate obstacle or obstruction acting as a spatially extended volume forcing on the flow. Its sole purpose is to tailor the velocity distribution of the flow at the downstream end of the device (in the plane $z = 0$) in a controlled way. For reference in the following text the device is referred to as obstacle–FMD.

Devices with several different blockage ratios, gap widths, more or less holes with different diameters have also been tested. Although there is certainly still room for further optimization, it was found that with reasonable effort the specific dimensions mentioned above seem to work best in terms of relaminarization capability. The device is quite sensitive to changes. *E.g.,* already if the diameter d_3 of the holes is less than 2.8 mm or larger than 4 mm instead of 3.3 mm and all other dimensions are left unchanged, the device is not able to relaminarize the flow at any Reynolds
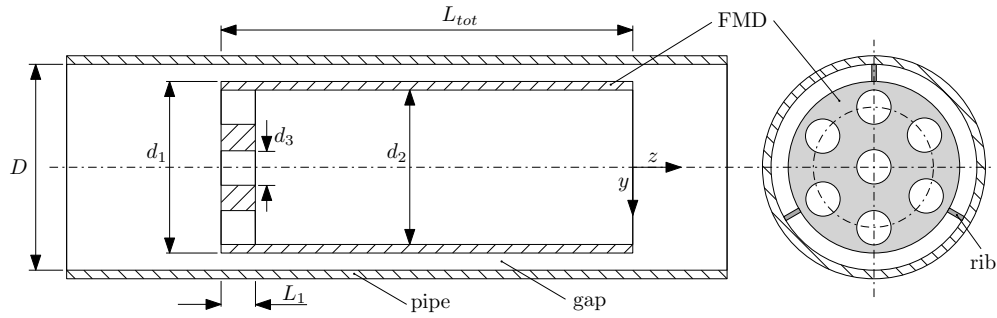
Figure 4.2: Sketch (sideview and frontview) of the orifice plate obstacle (obstacle–FMD). The device can be mounted at any axial position within the pipe (the ribs provide interference fit). The flow direction is from left to right. Drawing not to scale.

number.

4.2.3 Annular gap injection nozzle (method 2)

To complement and extend the purely passive control mechanism of the obstacle–FMD we designed a device which allows to inject fluid into the main pipe through a small annular concentric gap close to the pipe wall as shown in Fig. 4.3. The modification of the velocity profile resulting from this active open–loop control of the flow is similar to the stationary obstacle, but the amount of injected fluid and hence the level of acceleration close to the pipe wall can be controlled and continuously adjusted via a valve in the feeding line. In the reported setup the feeding line is implemented as a bypass that takes fluid from upstream the main pipe and re–injects it through the device. However, the injection device could just as well be used without the bypass by injecting fluid from an external reservoir via a pump. This method was found to be equally effective and relaminarization up to similar Re values could be achieved. We tested two different devices by systematically varying the injected flow rate at different Reynolds numbers, one device with an annular gap of 1 mm and one with an annular gap of 2 mm. In the following text these devices are referred to as 1 mm–FMD and 2 mm–FMD.

As sketched in Fig. 4.3 the main pipe is slightly narrowed in a short range just upstream the injection point (1 mm–FMD: $d_1 = 26.6$ mm, $d_2 = 28$ mm, open gap area $A_1 = 91.1$ mm^2; 2 mm–FMD: $d_1 = 24.6$ mm, $d_2 = 26$ mm, open gap area
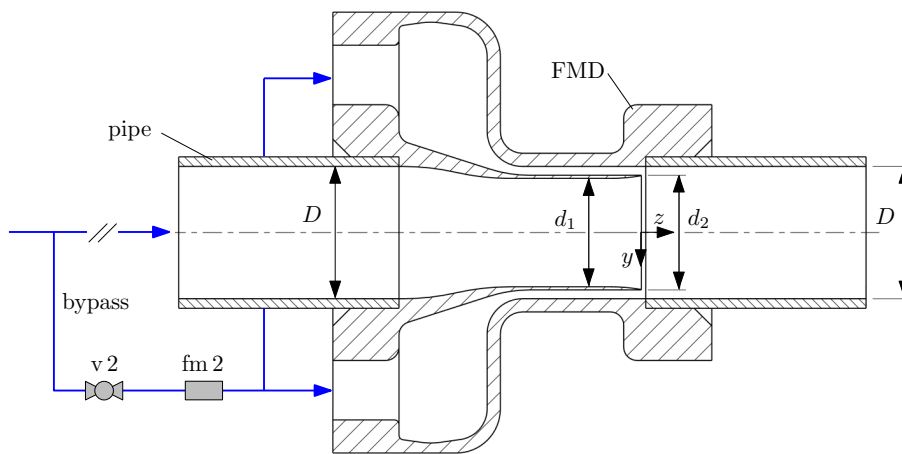
Figure 4.3: Sketch of the control device acting as injection nozzle through an annular gap (1 mm–FMD and 2 mm–FMD). Fluid is taken from the main pipe via a bypass and then re–injected through a concentric gap close to the wall. The device is mounted within two pipe segments. The bypass is equipped with a valve (v 2) and a flow meter (fm 2). The flow direction is from left to right. Drawing not to scale.

$A_2 = 175.9 \, \text{mm}^2$). At a small backward facing step ($z = 0$, the plane of confluence) the fluid coming from the bypass is axially injected into the main pipe through the annular gap close to the wall. Based on the measured bypass flow rate Q_{bp} and the open gap area, the mean velocity U_{inj} of the injected flow in the plane of confluence can be calculated. As the total flow rate Q_m is measured in the supply pipe (see Section 4.2.1), the specified Reynolds number in the main pipe applies to the range upstream the bypass and downstream the confluence at $z = 0$. The Reynolds number Re_n and the mean velocity U_n in the slightly narrowed part of the device is calculated based on d_1 and $Q_m - Q_{bp}$.

In all measurements reported the flow rate was chosen such that $Re_n \gtrsim 3000$ to ensure fully turbulent flow in the slightly narrowed section (as for $Re_n \lesssim 2800$ the main flow may become (intermittently) laminar already without any forcing [Avila and Hof, 2013]). For the 2 mm–FMD this criterion was met for $Re \gtrsim 4000$.

4.3   Results

In this section we present the results of the measurements split into two subsections for each kind of device. Representative sets of stereoscopic PIV measurements are shown for Reynolds numbers where the flow relaminarizes and where it does not. The FMDs were first investigated at different Reynolds numbers by means of mere visualization. Neutrally buoyant anisotropic particles [Matisse and Gorman, 1984] were added as tracer particles and the flow in the pipe was illuminated by means of LED string lights along the whole length of the pipe to be able to observe the development of the flow field downstream of the FMDs. The observations were also recorded with a video camera. A selected prime example of a relaminarizing flow is made available in the online supporting material.

From visual observations in combination with pressure drop measurements we obtained very reliable information whether or not the flow completely relaminarized at a certain Reynolds number. Although relaminarization is a gradual process [Sreenivasan, 1982] and the flow tends only asymptotically to the fully developed laminar parabolic Hagen–Poiseuille profile [Durst *et al.*, 2005], it is accompanied by drastic changes in the structure and dynamical behaviour of the flow. The mean velocity profile departs from the well–known law of the wall, the friction factor exhibits a substantial decrease and Reynolds stresses become negligible, the turbulence intensity goes down, *etc.*. Visually most striking and conspicuous is the total decay of any eddying motion, as all velocities normal to the streamwise direction fade away.

More difficult to capture and quantify is the transient state of ongoing relaminarization, also referred to as laminarescent. It signifies the earlier stages of relaminarization (loosely, a precursor to relaminarization) in which large departures occur from the turbulent state [Sreenivasan, 1982]. However, remaining perturbations in the flow may trigger retransition to turbulence. It is only when the flow has reached a sufficiently laminar state that it remains laminar for the remainder of the pipe. As will be shown further down, monitoring the flow at $z \approx 100 - 150$ provides a clear and unambiguous indication whether or not the flow has relaminarized
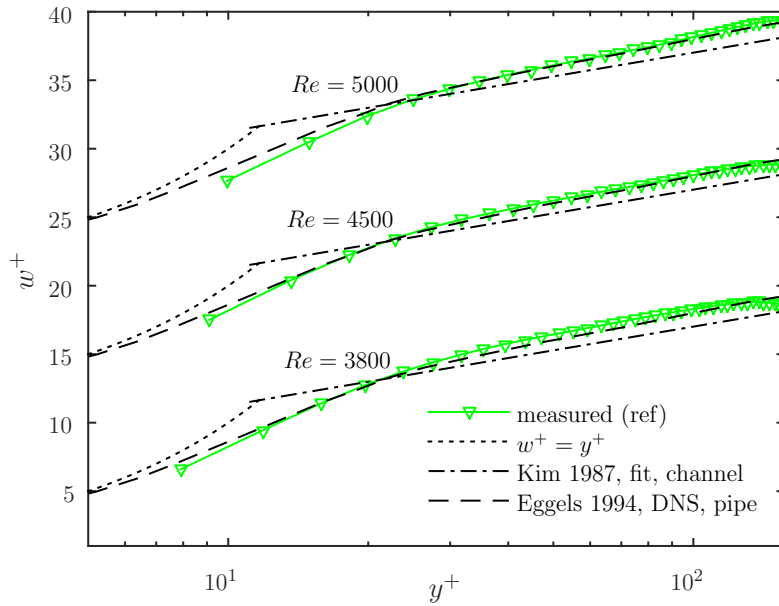
Figure 4.4: A comparison of the measured uncontrolled turbulent flow (ref) with the the law of the wall (fit from Kim *et al.* [1987], $w^+ = 2.5 \ln y^+ + 5.5$) and DNS in a pipe from Eggels *et al.* [1994]. The viscous sublayer is indicated by $w^+ = y^+$.

completely.

4.3.1 Measurements of uncontrolled turbulent flow for reference

To be able to compare the controlled, relaminarizing flow to uncontrolled fully turbulent flow we first measured the flow without FMDs. The respective measurements are going to be used for reference in the remainder of the present work. The velocity profiles measured at $Re = 3800$, $Re = 4500$ and $Re = 5000$ normalized by the inner variables are plotted in Fig. 4.4 in the usual semi–logarithmic manner. For comparison, the law of the wall is plotted with the Kármán constant $\kappa = 0.4$ and the additive constant $A = 5.5$ (to compensate the low Reynolds number effect, see [Kim *et al.*, 1987]). Furthermore, DNS results by Eggels *et al.* [1994] for pipe flow at $Re = 5300$ are shown. Eggels *et al.* demonstrated that the mean velocity profile in a pipe fails to conform to the law of the wall, in contrast to channel flow. This is clearly reaffirmed by our measurements. While for $Re = 3800$ our measured velocity profile is slightly above the DNS data of Eggels *et al.*, their data coincide very well with our results for $Re = 4500$ and $Re = 5000$. Eggels *et al.* stated a best fit of $\kappa = 0.35$
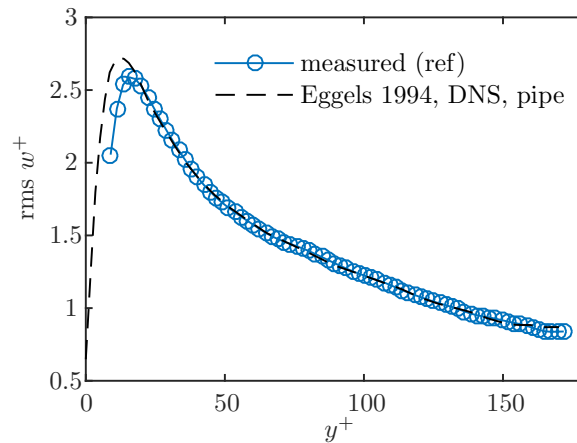
Figure 4.5: Streamwise rms profile measured at $Re = 5000$ scaled on inner variables. The dashed line shows the results from Eggels *et al.* [1994] for comparison.

with an additive constant $A = 4.8$. For $Re = 5000$ we find a best fit of $\kappa = 0.33$ and $A = 4.2$ for $40 < y^+ < 120$ or $\kappa = 0.34$ and $A = 4.6$ for $40 < y^+ < 100$. The near wall region is only partly resolved in the measured velocity profiles. The smallest values of y^+ are 7.9, 9.1 and 10 respectively, corresponding to $\approx 0.08\,\text{mm}$.

The root–mean–square (rms) values of the streamwise fluctuating velocity $\sqrt{\overline{w'^2}}$, normalized by the friction velocity, are plotted in Fig. 4.5 for $Re = 5000$. Obviously, the major part of the fluctuations occurs close to the wall. For comparison, DNS results by Eggels *et al.* [1994] for pipe flow at $Re = 5300$ are shown. The peak value (2.6) of the measured rms is in excellent accordance and the position of the peak ($y^+ = 18.2$) as well as the overall trend of the data is in good accordance with previous investigations (see also [Mochizuki and Nieuwstadt, 1996]).

4.3.2 Orifice plate obstacle (inset)

For the visual observation of the flow field we placed the obstacle–FMD 80 D downstream from the entrance of the pipe where the turbulent flow can be considered fully developed. We varied the Reynolds number between 2500 and 5000 and found a continuously laminar flow field at $z = 150$ up to $Re \approx 4200$. At slightly higher Reynolds numbers we observed laminar–turbulent intermittency. For $Re \gtrsim 4400$ we found only turbulent flow at $z = 150$. Inspection of the flow field in the closer downstream vicinity ($0 < z \lesssim 10$) of the obstacle–FMD shows a rather turbulent
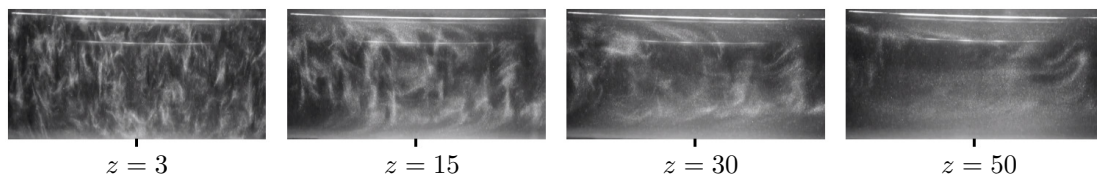
Figure 4.6: Still pictures from supplementary movie 1 (see online materials) of a short section of the pipe at $Re = 4000$. The camera was following the flow downstream the obstacle–FMD at the mean velocity U. The difference between turbulent flow (at $z = 3$) and laminar flow (at $z = 50$) is unambiguous. Video available online at https://doi.org/10.1007/s10494-018-9896-4.

zone right downstream the device where strong cross–stream motion is obviously present. But for $Re \lesssim 4200$ all visible perturbations in the flow field decay until the flow appears clearly laminar at $z \approx 50$. This evolution is well observable in Fig. 4.6, depicting still pictures from supplementary movie 1 (see online materials; see also [Kühnen *et al.*, 2015b]), where the camera follows the flow at approximately the mean velocity on its journey from upstream of the device until it has relaminarized downstream. A laminarescent part of the flow as in Fig. 4.6 at $z = 15$, where the turbulence intensity is obviously reduced by some amount in the downstream vicinity of the device, could be observed up to $Re \approx 4800$.

To characterize the flow downstream the device we took PIV measurements for two representative cases at $Re = 3800$ and $Re = 4500$ and 14 axial stations downstream the FMD: at $z = 2, 3, 4, 6, 9, 12, 15, 18, 24, 30, 40, 50, 70$ and 100. The development of the time–averaged, streamwise velocity $\overline{w}$ in the plane $y = 0$ is shown in Figs. 4.7 (a) and (b). Each profile is calculated from 200 independent vector fields and azimuthally and temporally averaged. For reference, the most left profile (ref) is showing the respective measurement of uncontrolled turbulent flow. Fig. 4.7 (c) provides the respective levels of the centerline velocity for quantification. As can be seen from the figure, at $Re = 3800$ the flow fully relaminarizes, while at $Re = 4500$ retransition to turbulence takes place.

A particularly noteworthy effect of the device on the time–averaged velocity profiles is the increase in the velocity gradient at the wall. At $z = 2$ the profiles at both Reynolds numbers exhibit characteristic overshoots of fast fluid close to the wall (peak at $x = \pm 0.44$) and a clearly decreased centerline velocity (≈ 1 and

(a) $Re = 3800$

(b) $Re = 4500$

(c) centerline velocities
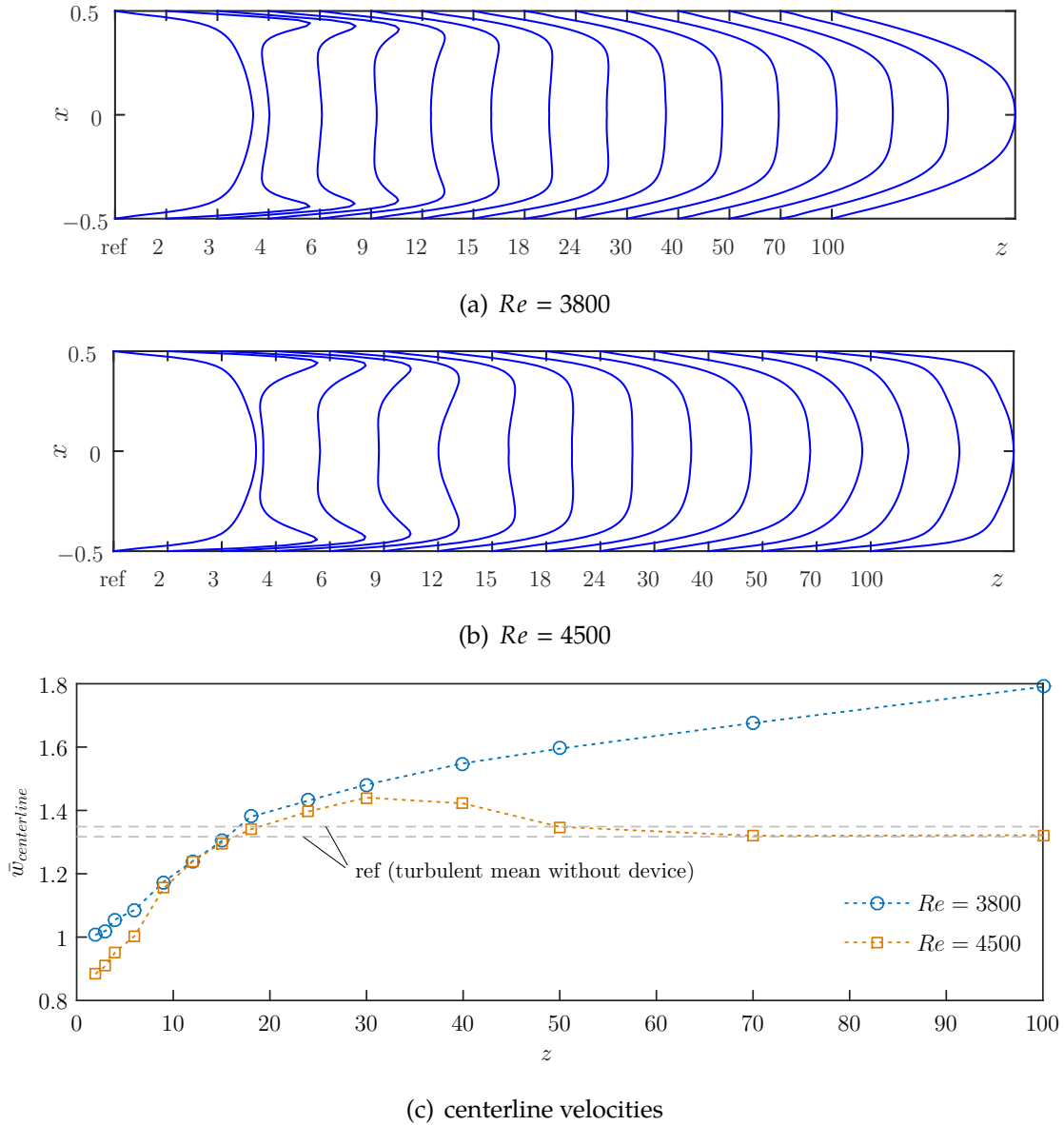
Figure 4.7: Downstream evolution of mean streamwise velocity profiles ($\overline{w}$) in the plane $y = 0$ measured at (a) $Re = 3800$ and (b) $Re = 4500$. In each plot the profile of uncontrolled turbulent flow is shown for reference (ref) at the left. (c) Respective levels of the axially developing centerline velocity.

≈ 0.9 respectively), causing a M–shaped appearance with a pronounced plateau in the center. This plateau in the bulk area, where the axial velocity is approximately constant, stretches from $-0.32 \lesssim x \lesssim 0.32$. The plateau is even more flat at $z = 3$ and 4, where the peak of the velocity overshoot has moved slightly towards the center ($x \pm 0.43$ and $x \pm 0.41$, respectively). The increase in the velocity gradient close to the wall, however, does not persist for more than a few pipe diameters. At $z \approx 15$ the two peaks have disappeared completely and the plateau covers the range $-0.25 \lesssim x \lesssim 0.25$. Simultaneously, the initially steep gradient in the axial velocity close to the wall has decreased considerably. Concerning the centerline velocity the value of uncontrolled turbulent flow is regained around $z = 15 - 18$. Interestingly, for both Reynolds numbers $\overline{w_c}$ rises clearly above the uncontrolled level in the subsequent range $18 \lesssim z \lesssim 50$.

The completely different downstream behavior of the flow at $Re = 3800$ and $Re = 4500$ becomes apparent only for $z \gtrsim 30$. The flow at $Re = 3800$ keeps developing towards a laminar parabolic profile. At $z = 100$ the centerline velocity has reached a value of ≈ 1.8. At this Reynolds number it takes yet another $\approx 120\,D$ [Durst *et al.*, 2005] to reach the fully developed state under perfect conditions (the laminar profile is sensitive to small disturbances, *e.g.* due to thermal convection or minor misalignments of the pipe segments [van Doorne and Westerweel, 2007]). But the centerline velocity of the flow at $Re = 4500$ keeps increasing only till $z \approx 30$. The mean turbulent centerline velocity is clearly surpassed at $z \gtrsim 20$. However, in the range $30 \lesssim z \lesssim 40$ the centerline velocity starts to fall back towards the turbulent mean.

The scenario of complete relaminarization at $Re = 3800$ and of final retransition to turbulence at $Re = 4500$ is also apparent from the axial development of the streamwise and inplane turbulence intensity $ti_w = \left\langle \frac{w_{\text{rms}}}{U} \right\rangle$ and $ti_{u,v} = \left\langle \frac{u_{\text{rms}} + v_{\text{rms}}}{2U} \right\rangle$ as plotted in Fig. 4.8 (a) and (b). Right downstream the device the levels of turbulence intensity are slightly increased above the turbulent reference flow. It should be noted however that in the bulk region of the cross section right downstream of the obstacle–FMD, remaining flow perturbations induced by the perforated plate at the upstream end of the obstacle–FMD may still be significant, as $L_{\text{tot}} = 200\,\text{mm}$ (see Fig. 4.2) is not
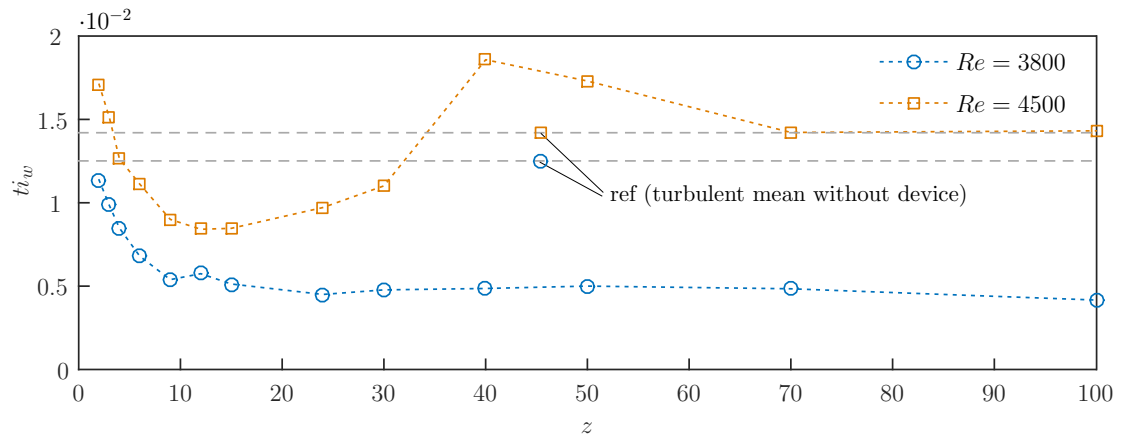
(a) turbulence intensity (streamwise)
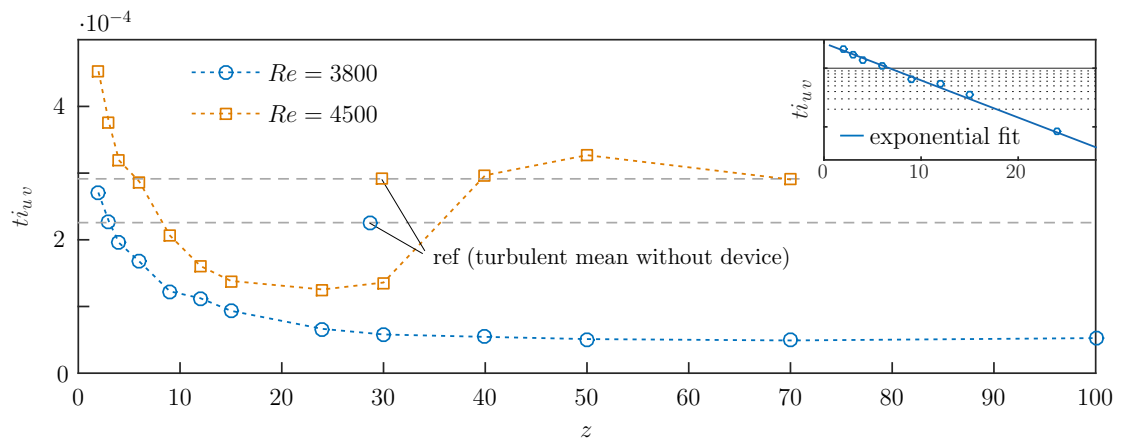
(b) turbulence intensity (inplane)

Figure 4.8: Downstream evolution of the streamwise (ti_w) and inplane ($ti_{u,v}$) turbulence intensity. The respective level of uncontrolled turbulent flow is shown for reference (ref). The inset in (b) displays an exponential fit to the data at $Re = 3800$ for $z = 2 - 30$, plotted on a log–scale.

sufficiently long to regain streamwise invariance (see *e.g.* [Barbin and Jones, 1963; Doherty *et al.*, 2007]). The increase in turbulence intensity can hence not be clearly attributed to the accelerated part of the flow coming through the gap.

Already at $z \gtrsim 3$ ($Re = 4500$) ti_w drops below the level of uncontrolled turbulent flow. The same applies regarding $ti_{u,v}$ at $z = 4$ ($Re = 3800$) and $z = 6$ ($Re = 4500$) respectively. While for $Re = 3800$ $ti_{u,v}$ decreases exponentially until $z \approx 30$ where the stable level of unavoidable measurement noise is reached, a qualitatively similar decrease in $ti_{u,v}$ at $Re = 4500$ is perceived only until $z = 15$. For $15 \lesssim z \lesssim 30$ $ti_{u,v}$ is almost constant, followed by a steep increase which even leads to an overshoot above the mean turbulent level for $40 \lesssim z \lesssim 70$. Further downstream the flow seems to resemble an uncontrolled turbulent flow again. ti_w exhibits a qualitatively very similar development, but the increase back to the turbulent level at $Re = 4500$ starts a little earlier (around $z = 15$) and the overshoot above the turbulent level takes place more rapidly and pronouncedly (+30% at $z = 40$) . At $Re = 3800$ ti_w seems to reach the laminar (noise) level in the range $z = 10 - 15$. The remaining velocity fluctuations can be attributed to measurement noise.

To elucidate the downstream development of turbulence fluctuations within the cross section of the pipe, the streamwise velocity fluctuations (w_{rms}^2) at selected axial stations are depicted in Fig. 4.9. The reference measurement of the uncontrolled turbulent flow (see also Fig. 4.5) at the respective Reynolds number is plotted as a dashed line. In the core region of the cross section right downstream of the obstacle–FMD the flow is only slightly changed for both Reynolds numbers compared to the uncontrolled flow, recognizable by the increased rms level for $x \lesssim 0.2$ at $z = 2$. This is apparently due to the perturbations caused by the perforated plate at the upstream end of the obstacle–FMD. Closer to the wall a more prominent deviation from the uncontrolled flow is visible, depicting also a clear cut qualitative difference between the measurements at $Re = 3800$ and $Re = 4500$. For $Re = 3800$ the maximum of streamwise fluctuations close to the wall has decreased below the level of uncontrolled flow already at $z = 2$. Additionally, the maximum has significantly moved towards the centerline (apparent until $z = 4$). As z increases there is a substantial reduction in turbulence level within the whole cross section.
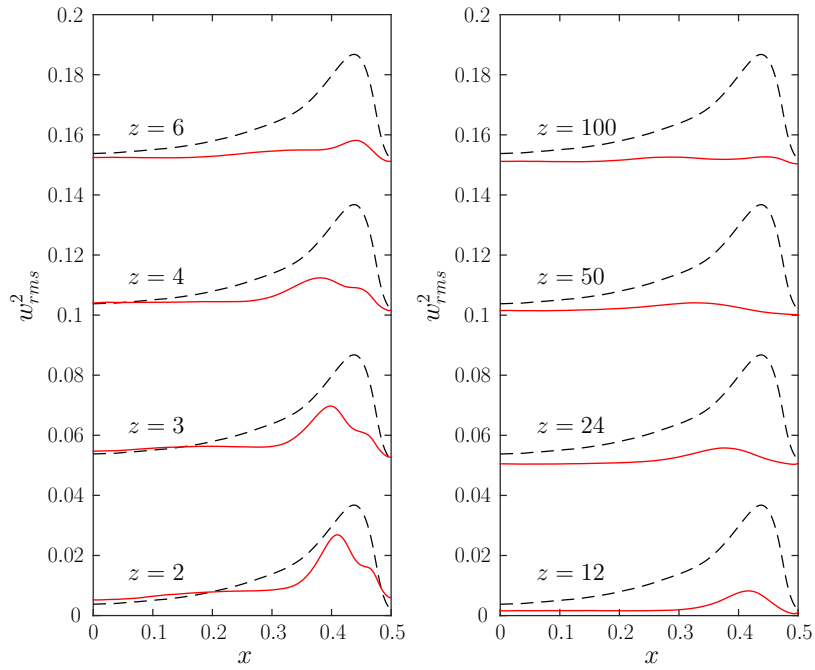
(a) *Re* = 3800
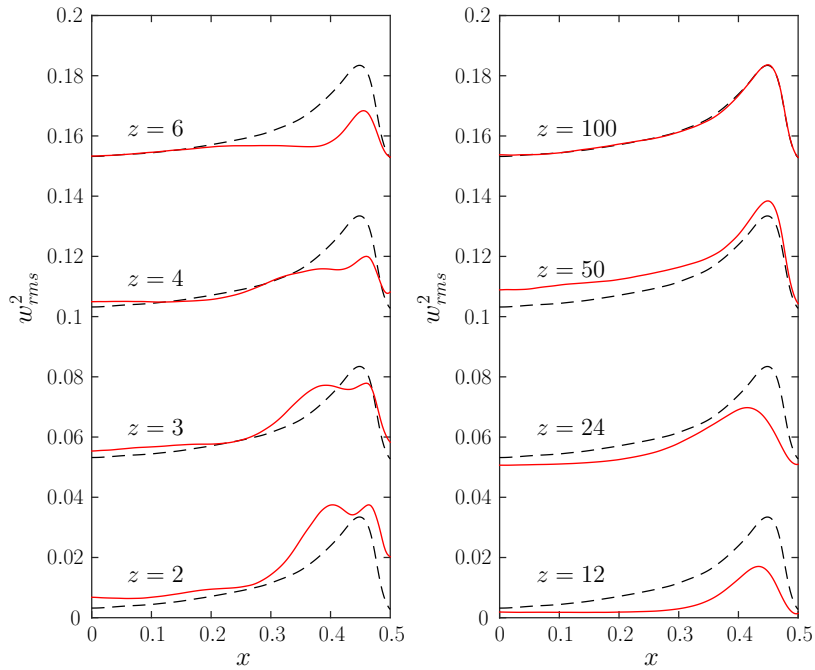
(b) *Re* = 4500

Figure 4.9: Downstream evolution of the streamwise velocity fluctuations (w_{rms}^2) at 8 selected axial stations for *Re* = 3800 and *Re* = 4500. The dashed line is showing the uncontrolled turbulent flow for reference.
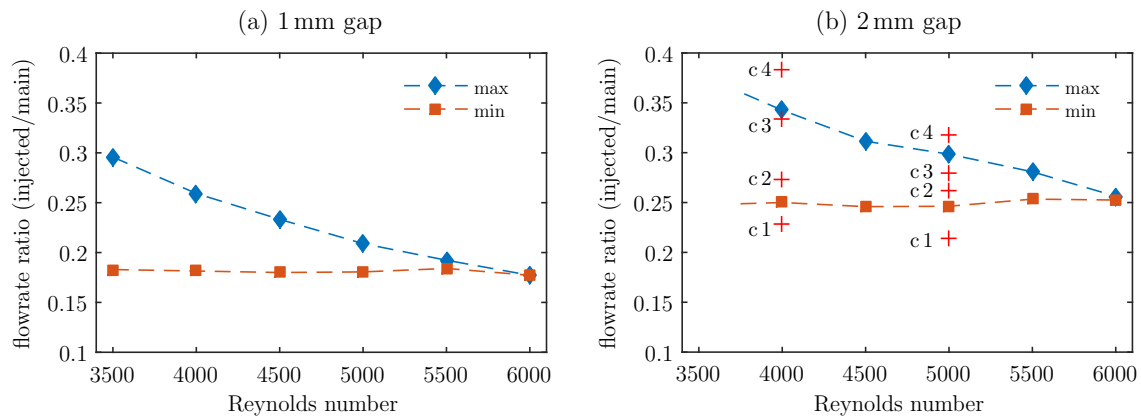
Figure 4.10: Ratio of flow rate injected into the main pipe through the concentric gap. The gap width is a) 1 mm and b) 2 mm. For increasing Reynolds numbers max and min depict the maximum and minimum injection flow rates that cause total relaminarization. All flow rate ratios in between also lead to relaminarization. For the cases c1—c4 at $Re = 4000$ and $Re = 5000$ in (b) marked by a $+$ see the text.

Initially the turbulent fluctuations decay very quickly close to the wall and more slowly in the bulk region. For $z > 30$ the flow can be considered laminar and the overall turbulence intensity does not change significantly anymore (see also Fig. 4.8).

For $Re = 4500$ on the other hand the maximum of streamwise fluctuations at $z = 2$ has not dropped significantly and is comparable to uncontrolled turbulence. A double–humped, much thickened shape of the near–wall peak can be observed instead (visible up to $z = 4$). However, for $z = 4 - 24$ the peak close to the wall clearly decreases beyond the level of uncontrolled flow and the overall turbulence intensity is substantially reduced. Yet, at $z = 50$ the near wall region looks similar to the reference flow again. In the core region the rms level is even increased beyond the reference flow, yielding the increased level in turbulence intensity as depicted in Fig. 4.8. Finally, at $z = 100$, the flow has completely returned to the uncontrolled level.

4.3.3 Annular gap injection nozzle

With the 1 mm–FMD and the 2 mm–FMD, the devices which allow to inject fluid into the main pipe through an annular gap close to the pipe wall, the amount of injected
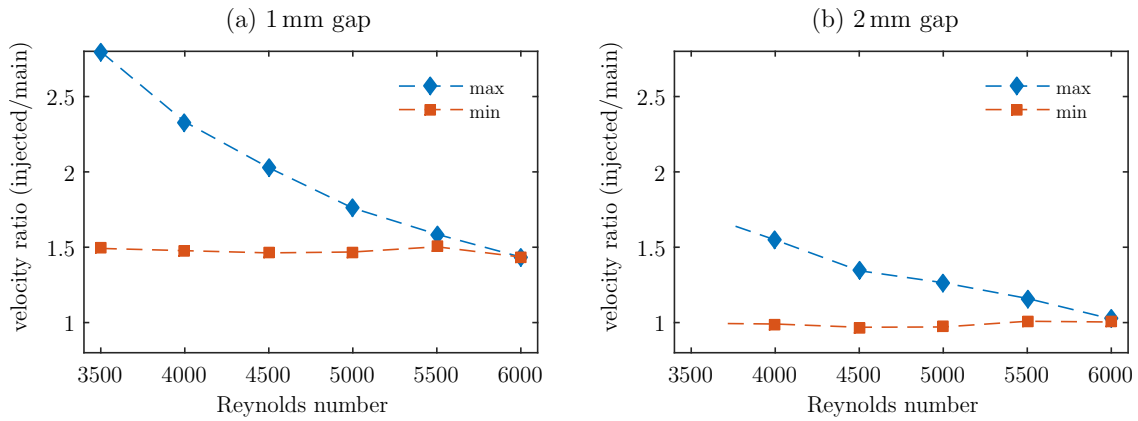
Figure 4.11: Velocity ratios U_{inj}/U_n of the injected flow to the respective main flow in the pipe at $z = 0$ (in the plane of confluence). The (mean) velocities are calculated based on the measured flow rates as depicted in Fig. 4.10.

fluid Q_{bp} and hence the level of acceleration close to the pipe wall can be controlled and continuously adjusted via a valve in the bypass. To investigate which flow rates and mean flow velocities of injected flow result in complete relaminarization, we increased the Reynolds number in increments of 500 and varied the flow rate through the bypass, *i.e.* the amount of fluid injected through the gap.

Up to $Re = 6000$ we could find injection flow rates for both gap widths which cause a continuously laminar flow field at $z = 150$ and the remainder of the pipe. *I.e.*, when we measure the pressure drop sufficiently far downstream we find either turbulent or laminar pressure drop depending on the respective injection flow rate, nothing in between. Fig. 4.10 shows the measured ratios $Q_{bp}/(Q_m - Q_{bp})$ of the flow rates of injected flow to the main flow for each gap width which lead to relaminarization. Fig. 4.11 shows the respective velocity ratios U_{inj}/U_n of injected flow to the main flow. In both figures max and min depict the maximum and minimum flow rate (velocity) ratios that would cause total relaminarization downstream. All flow rate (velocity) ratios in between also relaminarize the flow. While at lower Reynolds numbers a relatively broad range of flow rate ratios is suitable for relaminarization, the range quickly narrows down with increasing Reynolds number. For both devices it is rather the maximum of the flow rate ratio which decreases from initially $\approx 30\%$ (1 mm–FMD) and $\approx 35\%$ (2 mm–FMD), while the minimum amount of injected flow stays relatively constant at 18% and 25% for

the 1 mm–FMD and 2 mm–FMD respectively. Concerning the velocity ratio this implies possible injection velocities in a broad range of 1.5—3 (1 mm–FMD) and 1—1.5 (2 mm–FMD) times higher than the mean flow velocity in the pipe at $Re = 4000$. At $Re = 6000$ the injection velocities necessary for total relaminarization narrow down to 1.5 and 1 as compared to the velocity of the main flow. For both gap widths the curves intersect slightly above $Re = 6000$, indicating that for higher Reynolds numbers no complete relaminarization is possible with the present devices.

Visual inspection of the flow field in the downstream vicinity ($0 < z \lesssim 50$) of the FMDs at Reynolds numbers and flow rate ratios between min and max shows a scenario which is very similar to the one during relaminarization downstream the obstacle–FMD as described in section 4.3.2: the flow field in the direct downstream vicinity ($0 < z \lesssim 10$) of the device shows a turbulent flow and turbulence levels look comparable to the level upstream the device. However, for $Re \lesssim 6000$ all visible perturbations in the flow field quickly decay downstream until the flow is clearly perceivable laminar at $z \approx 30 - 50$. Furthermore, the flow stays unambiguously laminar for the remainder of the pipe.

If the ratio of injected fluid is just below the minimum or just above the maximum depicted in Fig. 4.10, a transiently relaminarizing (laminarescent) part of the flow can be observed as in Fig. 4.6 at $z = 15$, where the turbulence intensity is obviously reduced by some amount in the downstream vicinity of the device. *I.e.*, incipient (transient) relaminarization at earlier stages is well observable, but finally the flow always returns to a fully turbulent state at around $z \approx 30 - 50$.

As the scenario for injection flow rates between the indicated minimum and maximum and $Re \lesssim 6000$ is so similar to the one downstream the obstacle–FMD at $Re = 3800$ (see *e.g.* Fig. 4.6 and 4.7) and for flow rates closely below the minimum or above the maximum similar to to the one downstream the obstacle–FMD at $Re = 4500$ respectively, no further pictures or measurements of the downstream evolution are shown for the 1 mm–FMD and the 2 mm–FMD.

Fig. 4.12 presents PIV measurements of 4 different injection flow rates with the 2 mm–FMD at a single axial station, namely $z = 2.5$, which is the closest distance to the device possible for our stereoscopic PIV measurements. The four cases c1—c4
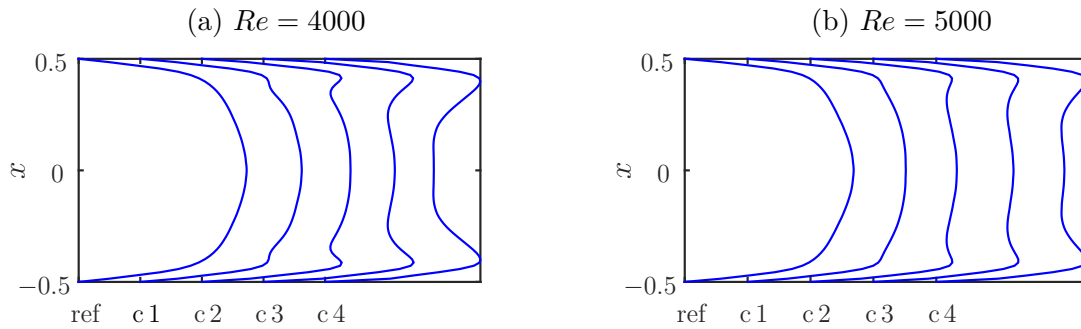
Figure 4.12: Streamwise velocity profiles ($\overline{w}$) measured at $z = 2.5$ and (a) $Re = 4000$ and (b) $Re = 5000$. Cases 1—4 depict different injection flow rates with the $2\,mm$–FMD as indicated in Fig. 4.10 (b) by a +. A measured profile of uncontrolled turbulent flow is shown for reference (ref).

of different injection flow rates are indicated in Fig. 4.10 (b) by the + symbols at $Re = 4000$ and $Re = 5000$. c1 represents a case where the flow rate of injected fluid is just beneath the minimum flow rate which is necessary for full relaminarization. c2 and c3 represent cases where full relaminarization is observed. At c4 the flow rate is already somewhat above the maximum, meaning that the controlled flow exhibits features of relaminarization but finally returns to a turbulent state downstream (similar to c1). The streamwise velocity profiles in Fig. 4.12 clearly show the increasing injection flow rate close to the wall. While for c1 only a minor hump is visible, for c2—c4 the peak close to the wall (stably at $x \approx 0.41$ for all injection flow rates and both Reynolds numbers) is manifest. Again, the appearance of the velocity profiles (at least for c4) could be described as M–shaped with a pronounced plateau in the center.

The respective streamwise velocity fluctuations at $z = 2.5$ are plotted in Fig. 4.13. For the injection case c1 the near wall peak is greatly reduced compared to the reference flow and moved from $x \approx 0.44$ to $x \approx 0.33$ for both Reynolds numbers. All streamwise fluctuations close to the wall have almost disappeared, and in the core region the rms level is already reduced too. However, the flow does not relaminarize in the long term. For injection cases c2 and c3 the reduction of the near wall peak is even more distinct, especially at $Re = 5000$, where no significant peak is present at all. Also the reduction in the core region is more pronounced. Although for c3 the fluctuation level close to the wall is increased as compared to
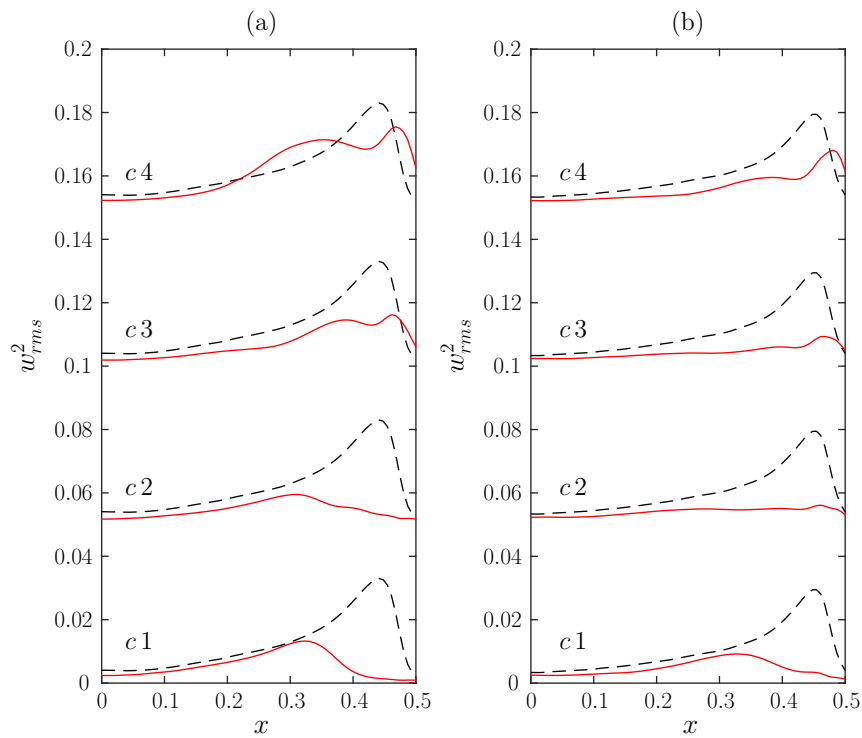
Figure 4.13: Streamwise velocity fluctuations (w_{rms}^2) measured at $z = 2.5$ and (a) $Re = 4000$ and (b) $Re = 5000$. Cases c1–c4 depict different injection flow rates as indicated in Fig. 4.10 (b) by a +. The dashed line is showing uncontrolled turbulent flow for reference.
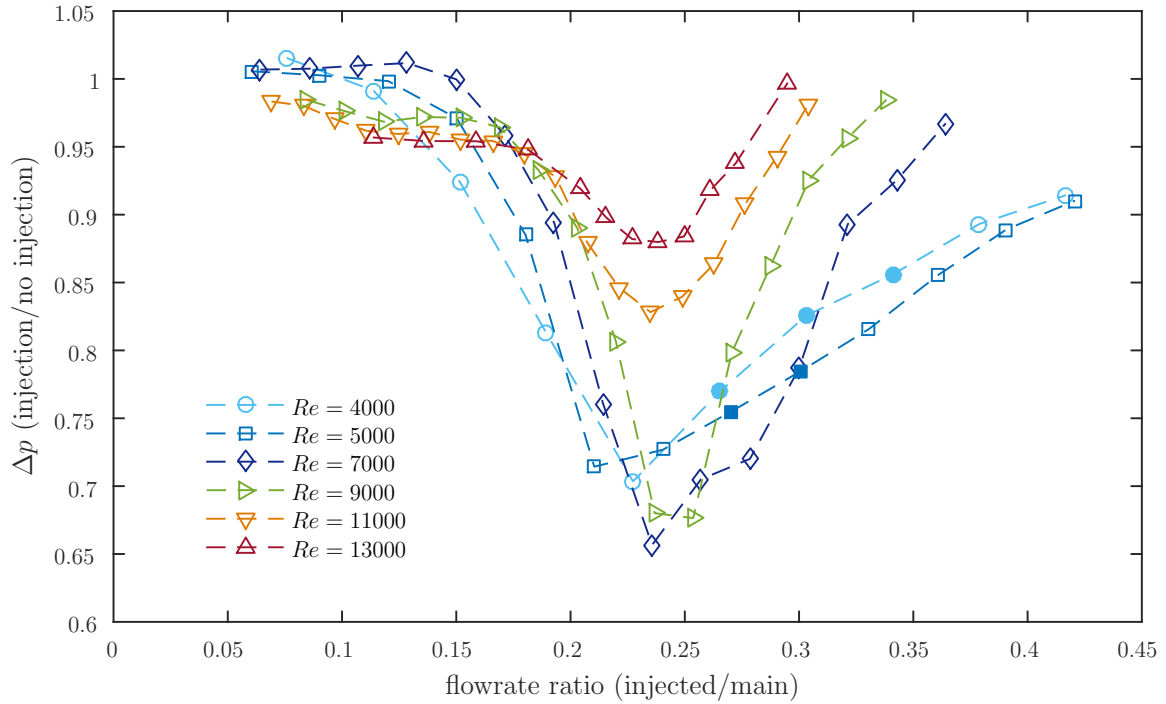
Figure 4.14: Variation of the pressure drop Δp (scaled with the pressure drop of the unforced reference flow) with different injection flow rates, measured in the downstream vicinity of the 2 mm–FMD (first pressure tap at $z = 6.2$, second at $z = 29$). Filled symbols indicate full relaminarization further downstream.

c2, especially for $Re = 4000$, c2 and c3 show clearly reduced fluctuation levels and accordingly relaminarize completely downstream. For the injection case c4 it seems that, although the absolute level of the near wall peak is still reduced below the uncontrolled turbulent reference, a double humped, thickened shape of the peak can be observed. c4 eventually turns fully turbulent further downstream.

For $Re > 6000$ we visually also observed a transiently relaminarizing state in the section $z \approx 6 - 30$ up to $Re \approx 10\,000$, similar to the scenario described in section 4.3.2 downstream the obstacle–FMD at $Re = 4500$. The transient relaminarization can cause laminar–turbulent intermittency in the section $z \approx 30 - 100$, although not very pronounced. The higher the Reynolds number, the higher the turbulent fraction, where laminar patches would quickly shrink downstream due to the faster propagation of the turbulent fronts [Barkley *et al.*, 2015].

To further investigate the evolution of the flow right downstream the injection device and detect temporally and spatially confined (partial) relaminarization we

measured the mean streamwise pressure gradient between two pressure taps at $z = 6$ and $z = 29$ respectively (*i.e.* over a $23\,D$ stretch). The first pressure tap is supposed to be sufficiently far away from $z = 0$ to avoid direct influence from the backward facing step of the injection device. At the same time the second pressure tap is supposed to be sufficiently close to the device to cover the whole area of transient relaminarization suggested by visual observations and Figs. 4.7 and 4.8.

The measured variation of Δp with the injection flow rate at several Reynolds numbers is plotted in Fig. 4.14. For all cases depicted we find significant drag reduction at certain injection flow rates, and the trend is similar to increasing the injection from zero: above an injected flow rate of $\approx 15\%$ a clear drag reduction can be observed, suggesting the onset of relaminarization for flow rate ratios roughly between $10 - 15\%$ for this specific device. The highest decrease in Δp is found for flow rate ratios around $20 - 25\%$. With even higher injection flow rates Δp returns towards the initial uncontrolled value. For $Re = 4000$ and $Re = 5000$ Δp decreases by up to $\approx 30\%$ for injection flow rates of $\approx 20 - 25\%$. Interestingly, the maximum drag reduction over the $23\,D$ stretch downstream of the injection point is not achieved for those injection flow rates necessary for complete relaminarization further downstream (indicated by filled symbols, see also Fig. 4.10), but for flow rates which are slightly below. For $Re = 7000$ and $Re = 9000$ the drag reduction is even larger (down to 65% of the uncontrolled flow), despite the fact that the flows return to turbulence further downstream. At $Re = 11\,000$ and $Re = 13\,000$ the decrease in Δp is still significant (by 18% and 12% respectively), yet already much less. However, the measurements clearly indicate transient relaminarization also at these higher Reynolds numbers, *i.e.* temporary relaminarization in a spatially confined region right downstream the injection device.

4.4   Discussion

Our results demonstrate that by increasing the flow velocity close to the pipe wall in the proposed way turbulence can either be completely annihilated or at least temporally (in a spatially confined region downstream the control) weakened

considerably. A chief precondition to the relaminarization process seems to be a steady, homogeneous local acceleration of the region of the viscous sublayer and the buffer layer above the level of uncontrolled flow, while the velocity is decreased accordingly in the log–law region. Once this profile modification is realized, we observe an immediate collapse of turbulence production at the wall. Thereafter turbulence intensity decays exponentially with z. The most drastic reduction in turbulence levels is found in the region near the pipe wall. If the injection (forcing of the velocity profile) is too weak or too strong or at $Re \gtrsim 6000$ several effects like remaining perturbations in the flow or secondary circulation caused by the injection trigger turbulence again and inevitably lead to a turbulent flow further downstream.

The results are in good accordance with the principal process of relaminarization in previous investigations concerning the natural decay of turbulence at low (subcritical) Reynolds numbers. *E.g.* Narayanan *et al.* [1968], who investigated relaminarization by reducing the initial Reynolds number, found exponential decay of the turbulence intensity in the streamwise direction too. Sibulkin [1962] also noted that the rate of decay of turbulence fluctuations appears to be more rapid near the wall and in the middle region of the pipe rather than at intermediate positions.

Pennell *et al.* [1972], who similarly observed temporal relaminarization triggered by fluid injected through a porous–walled pipe at Reynolds numbers above criticality, noticed a thickening of the viscous and buffer layers due to the start of injection. This caused a significant yet transient reduction of the turbulence level. In the later stages of the retransition to full turbulence (already at 6 and 10 D downstream the injection) their rms–profiles exhibit a very similar double–humped shape as we observe in Fig. 4.13 for case c4. Note that the cases in which double peaks are present in the rms profiles coincide with the existence of a strongly M–shaped velocity profile with strong velocity overshoots at the wall, and that all these profiles belong to cases which return to a full turbulent state further downstream. *I.e.*, one peak seems to be related to the near–wall turbulence generation and the other to the inner flank of the M–shape. This is consistent with Pennell *et al.* [1972], who suggested that the double–humped rms profile is a definite characteristic of the retransition process (to turbulence) in a pipe, and it seems also consistent with the observations
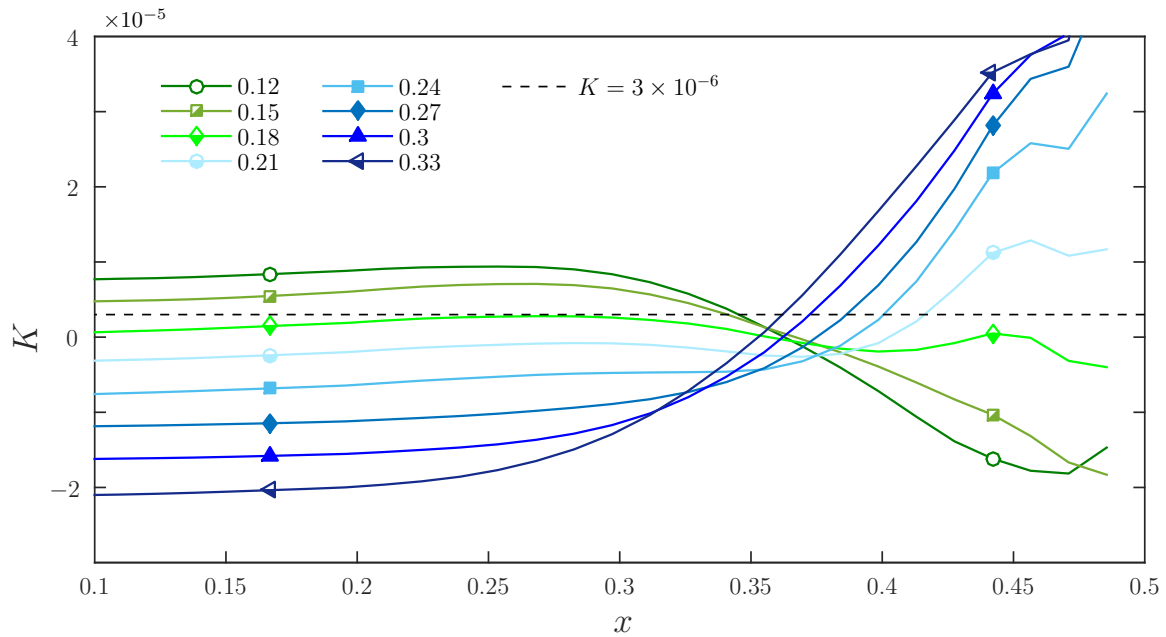
Figure 4.15: Local acceleration parameter *K* for different injection flow rates by the 2mm–FMD, measured at Re = 5000 and z = 2.5. Filled symbols indicate full relaminarization, half–filled symbols partial relaminarization further downstream.

of He *et al.* [2016b].

Furthermore, the qualitative trend of our data is very similar to observations (see *e.g.* [Patel and Head, 1968; Blackwelder and Kovasznay, 1972; Narasimha and Sreenivasan, 1973; Spalart, 1986; Warnack and Fernholz, 1998; Ichimiya *et al.*, 1998; Mukund *et al.*, 2006; Bourassa and Thomas, 2009]) concerning the effect of a FPG on a turbulent boundary layer. Under the (accelerating) influence of a FPG the viscous sublayer of a turbulent boundary layer is known to increase in thickness and the velocity in the outer region decreases. Measurements and simulations of boundary layers under a FPG have been characterized to exhibit reversion from the turbulent to the laminar state. It is also the FPG and its effect on the wall region of the flow which has been found to be primarily responsible for departures from the inner law (and, by inference, for triggering relaminarization).

Various parameters have been suggested to quantify the acceleration level in spatially accelerating flows and define the onset of relaminarization, see Bourassa and Thomas [2009] for a compilation of "acceleration driven laminarization parameters". While there is not a consensus in criteria of laminarization, one of the most widely

used is the acceleration parameter

$$K = \frac{\nu}{U_\infty^2} \frac{\mathrm{d}U_\infty}{\mathrm{d}z} \qquad (4.1)$$

where z is the streamwise direction, U_∞ is the free–stream velocity in this direction and ν the kinematic viscosity. Several authors have reported that turbulence is not sustained if K is higher than a critical value in the range $2.5 - 3.6 \times 10^{-6}$ [Launder, 1964; Moretti and Kays, 1965; Blackwelder and Kovasznay, 1972; Spalart, 1986]. At the same time most researchers have also criticized the use of K for being based on bulk flow parameters while the laminarization phenomenon is assumed to be a boundary layer event, necessarily having its basis in boundary layer considerations.

Based on eq. (4.1) we calculated the acceleration parameter $K = \frac{\nu}{w^2} \frac{\Delta w}{\Delta z}$ for different injection flow rates for 2mm–FMD at $Re = 5000$ with $\Delta z = 2.5$, *i.e.* we compare the acceleration level at $z = 2.5$ to the reference flow. Fig. 4.15 shows the result for selected flow rate ratios (0.12–0.33 in increments of 0.03) as a function of the radial direction. Furthermore, the aforementioned (global) level of $K \approx 3 \times 10^{-6}$ is indicated. Note that at arbitrarily small z close to the backward–facing step of the injection device the values for K in the near–wall region would be even higher. Fig. 4.15 suggests that the calculated values for K roughly match the critical values proposed in the literature, in particular when taking into account the findings provided by Fig. 4.14, indicating the onset of relaminarization for flow rate ratios between $10 - 15\%$ for the 2mm–FMD. It would be necessary to measure much closer to $z = 0$ for a more accurate assessment.

However, the major drawback of K is in any case the empirical nature and the lack of a mechanistic explanation. Warnack and Fernholz [1998] also pointed out that no single criterion could be used to predict the beginning or end of the breakdown of the law of the wall. They found that for flow with low acceleration where laminarization did not occur, there still was a breakdown of the law of the wall and a slight reduction in turbulent intensities. Relaminarization in boundary layers was observed as a gradual change of the turbulence properties and not catastrophic. Retransition, however, is a fast process due to the remaining turbulence structure and may be compared with bypass transition [Warnack and Fernholz, 1998].

An interesting approach to how specific conditions can cause the flow to laminarize on a local scale is provided by Jimenéz and Pinelli [1999]. They have shown not only that the near–wall turbulence regeneration cycle is autonomous, *i.e.* self–sustaining independently of whether or not fluctuations are present in the region $y^+ > 60$, but also that it can be interrupted numerically at various places, leading to the decay of turbulence and to eventual laminarization. Using a filter to make the streamwise velocity (more) uniform they identified the minimum streak length needed to sustain the cycle to be between 300 and 400 wall units. Their proposed control strategy is hence to weaken or decorrelate the streaks in the region below $y^+ = 60$ and above $y^+ = 20$.

Instead of using a numerical filter on the near–wall region, we locally replace and substitute the flow by injection through the gap. The injected flow and the resulting modified flow in the near–wall region is supposedly more homogeneous and "streak–free". In support of this, Fig. 4.16 (a) shows several distinct (high–speed) streaks in the near wall region (the region roughly below $y^+ = 60$ marked by the dashed circle) of an instantaneous snapshot of turbulent flow at $Re = 4000$. However, in Fig. 4.16 (b), depicting the flow field right downstream (at $z = 2.5$) of the 2 mm–FMD for the case c2 (*i.e.* relatively small injection just sufficient for full relaminarization), the streaky structures in the near–wall region are replaced or superimposed by the injected flow coming from the gap at the wall.

Kühnen *et al.* [2018c] designate the relaminarization observed due to a modified profile also to a weakening of the near–wall cycle, yet argue from a slightly different perspective focusing on the efficiency of the "lift–up mechanism" [Brandt, 2014]. To obtain a measure for the amplification mechanism of the regeneration cycle they consider the linearized Navier–Stokes equations and perform a transient growth (TG) analysis (following the algorithm given by Meseguer and Trefethen [2003]). The velocity profiles of all successfully modified, *i.e.* relaminarizing flows considered by Kühnen *et al.* [2018c] are shown to exhibit a substantially reduced TG. Generally the flatter the velocity profile the more the streak vortex interaction is suppressed and in the limiting case of a uniformly flat profile the lift–up mechanism breaks down entirely.

a) uncontrolled (ref)   b) controlled (c 2)
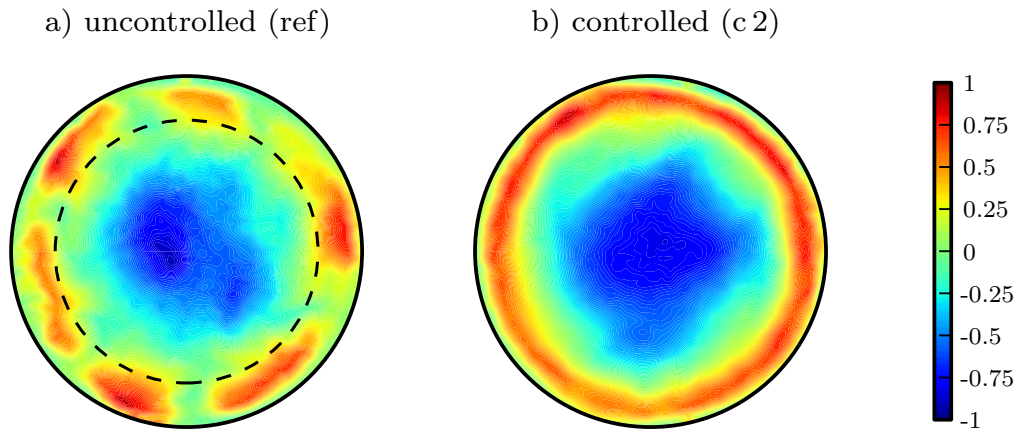
Figure 4.16: (Color online) Contours of the (instantaneous) streamwise velocity w in the cross section of the pipe. The laminar flow field has been subtracted to emphasize near–wall streaks (color bar expressed in units of the bulk velocity). a) is the unmodified turbulent reference flow and b) depicts case c2 with an injection flow rate as indicated in Fig. 4.10 (b) by a + ($Re = 4000$, $z = 2.5$). $y^+ \approx 60$ is indicated by the dashed circle.

We applied the same procedure here to (azimuthally and temporally averaged) velocity profiles measured at $z = 2.5$ downstream of the $2\,mm$–FMD for different injection flow rates. Assuming that the profile is fixed under the influence of the perturbation we conducted a TG analysis around the modified profiles. As shown in Fig. 4.17 the profiles indeed show a considerably decreasing TG with increasing injection flow rate suggesting that vortices are less efficient in producing streaks. Very similar to the trend of the pressure drop measured in the downstream vicinity of the device (see Fig. 4.14) the TG exhibits a clear minimum amplification at an optimal flow rate ratio before it starts to rise again towards the value of unmodified flow. Interestingly, the optimal is found at slightly higher injection flow rates than those for the smallest pressure drop in Fig. 4.14. In any case, the flow rate ratios with the least amplified perturbations are exactly those which relaminarize downstream at $Re = 4000$ and $Re = 5000$ (indicated with filled symbols). The data suggest that the turbulence regeneration cycle is weakened indeed and breaks down due to a reduced efficiency of the lift–up process.

The present study elucidates the general process of relaminarization caused by a modified streamwise velocity profile by simple means. Both the stationary obstacle–FMD and the injection nozzles (1 mm–FMD and $2\,mm$–FMD) can cause
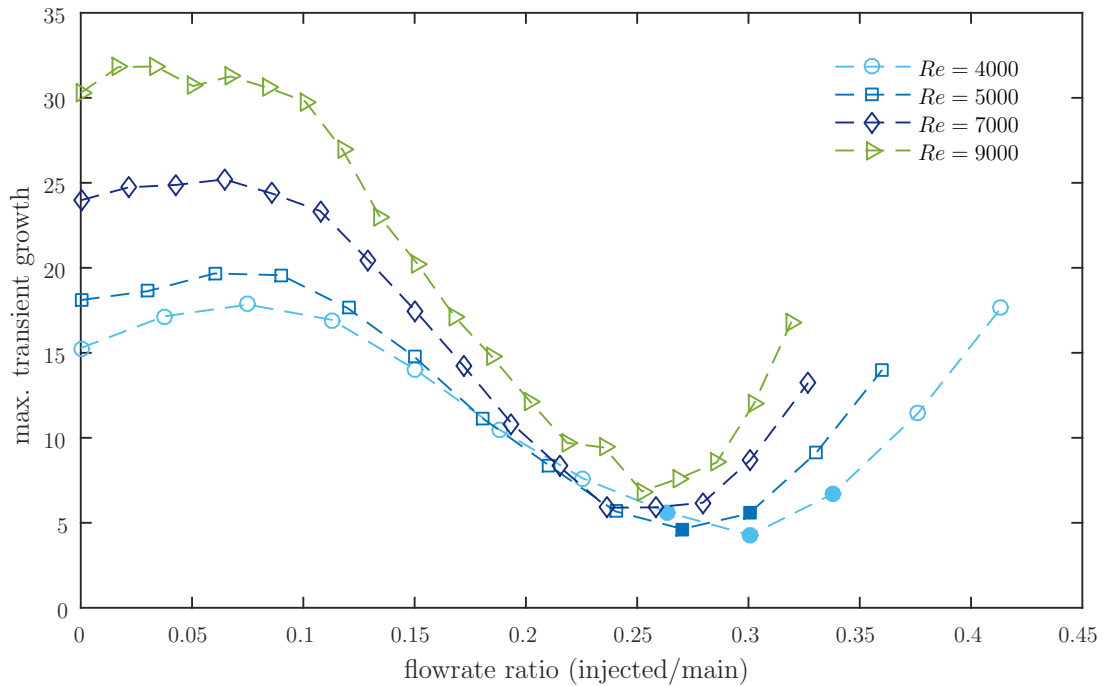
Figure 4.17: Variation of the transient growth with different injection flow rates, measured right behind (at $z = 2.5$) the 2 mm–FMD. Filled symbols indicate full relaminarization further downstream.

total relaminarization of the flow downstream and by that reduce skin friction by large amounts. As laminar pipe flow is linearly stable it will stay laminar for the remainder of a smooth straight pipe. Although both devices cause an initial cost in terms of an increased pressure drag either by the pipe blockage or by the required injection for full relaminarization, it is only a question of how long the unperturbed (straight and smooth) downstream pipe section is until a net energy gain can be realized. In the present context both devices are used solely for demonstration and proof-of-principle purposes. A lot of optimization regarding the added pressure drag of the methods could be done. Detailed considerations on energy savings and a possible net energy gain achievable with the present devices are beyond the scope of the present manuscript.

4.5   Summary and conclusion

Initially, relaminarization due to flow acceleration close to the wall may seem counterintuitive. However, in this work (see also Kühnen *et al.* [2018c]) we demonstrate

that fully turbulent flows in pipes can be completely relaminarized by rather simple means. An open–loop forcing of the streamwise velocity profile, either actively or passively, is sufficient to trigger turbulence breakdown. The present experiments demonstrate that the onset of relaminarization in a fully developed turbulent pipe flow occurs as a direct result of a particular shear stress distribution in the wall region. The underlying physical mechanism of relaminarization is attributed to a weakening of the near–wall turbulence production cycle.

Two different devices, a stationary obstacle (inset) and a device to inject additional fluid through an annular gap close to the wall, are used to control the flow. Both devices modify the streamwise velocity profile such that the flow in the center of the pipe is decelerated and the flow in the near wall region is accelerated. Visualization, pressure drop measurements and stereoscopic PIV measurements have been employed to determine both practice–oriented and fundamental information for relaminarizing turbulent flows in a circular pipe in the presence of devices which accelerate the near wall region. Downstream of the devices a fully developed laminar flow is established. The fluctuations are greatest just beyond the devices and die away with increasing downstream distance.

High amounts of energy (pumping power due to frictional drag) can be saved if the flow is laminar instead of turbulent. At $Re = 6000$, the highest Reynolds number were we achieve full relaminarization with the present devices, the pressure drop in the downstream distance is reduced by a factor of 3.4 due to relaminarization. At *e.g. Re* = 13 000, where we find transient relaminarization in a spatially confined region right downstream the devices, the drag reduction is still higher than 10%.

Future research should focus on the possible net energy gain and an optimization of the specific design in terms of pressure loss, such that an energetic break even point can be reached in a close downstream distance of the devices. Furthermore, a smarter design may allow relaminarization at much higher Reynolds numbers. In order to establish a possible cost saving potential of the presented control technique it is also necessary to determine over which distances the relaminarized flow persists under less perfect pipeline conditions.

5 Relaminarising pipe flow by wall movement

Following the recent observation that turbulent pipe flow can be relaminarised by a relatively simple modification of the mean velocity profile, we here carry out a quantitative experimental investigation of this phenomenon. Our study confirms that a flat velocity profile leads to a collapse of turbulence and in order to achieve the blunted profile shape, we employ a moving pipe segment that is briefly and rapidly shifted in the streamwise direction. The relaminarisation threshold and the minimum shift length and speeds are determined as a function of Reynolds number. Although turbulence is still active after the acceleration phase, the modulated profile possesses a severely decreased lift–up potential as measured by transient growth. As shown, this results in an exponential decay of fluctuations and the flow relaminarises. While this method can be easily applied at low to moderate flow speeds, the minimum streamwise length over which the acceleration needs to act increases linearly with the Reynolds number.

5.1 Introduction

Techniques for relaminarisation of turbulent pipe flow are alluring mainly for two reasons. Firstly, from a technological point of view, laminar pipe flow is optimal in terms of net driving power in a controlled scenario [Fukagata *et al.*, 2009], thus allowing in theory huge energy savings in pipeline systems. Secondly, a successful control of turbulence may provide better understanding and shed light on the dynamics of the phenomena involving production and dissipation of turbulence.

Several experimental investigations of relaminarising pipe and channel flows have been reviewed by Sreenivasan [1982]. However, the general experimental arrangement in the examples given involves a decrease in Reynolds number [Sibulkin, 1962; Narayanan, 1968; Selvam *et al.*, 2015]. Occasional evidence of relaminarisation not determined by dissipation and the Reynolds number has been found when a turbulent flow is subject to effects of acceleration, suction, blowing, magnetic fields, stratification, rotation, curvature or heating [Sreenivasan, 1982]. In accelerated pipe flow, *i.e.* during and subsequent to a rapid increase of the flow rate of an initially turbulent flow, the flow has been observed to transiently visit a quasi–laminar state and undergo a process of transition that resembles the laminar–turbulent transition [Lefebvre and White, 1989; Greenblatt and Moss, 1999; Greenblatt and Moss, 2004; He and Seddighi, 2013; He and Seddighi, 2015]. Temporary relaminarisation has also been reported for fluid injection through a porous wall segment in a pipe [Pennell *et al.*, 1972] .

Hof *et al.* [2010] introduced an alternative approach to suppressing localised turbulent spots by reducing the inflection points in the mean axial velocity and more recently Kühnen *et al.* [2018a; 2018b; 2018c] have shown that a suitable modification of the mean velocity profile can lead to a complete collapse of turbulence, causing a turbulent flow to fully relaminarise. With the aid of numerical simulations and different experimental devices, the authors demonstrated that a plug–like, mean streamwise velocity profile has a reduced lift–up potential and leads to a complete collapse of turbulence. In particular, one technique was shown to laminarise the flow up to a Reynolds number of 40 000 by strongly increasing the fluid velocity in

the wall region. In these experiments, an initially turbulent pipe flow is perturbed by impulsively shifting a pipe segment that moves coaxially and relatively to the rest of the pipe. As a consequence, the fluid in contact with the moving segment is subject to a temporary modification of the boundary condition and experiences an injection of momentum into the near–wall region. After the wall stops, the perturbed flow undergoes a progressive laminarisation while being advected downstream.

In the present investigation we want to further explore the effect and possibilities of such a moving wall strategy in order to modify the streamwise velocity profile and control turbulent pipe flow. Different from Kühnen *et al.* [2018c], we assess the circumstances under which turbulence fully decays by varying the wall velocity and shift length and we study the flow properties during and right after the wall movement up to a Reynolds number of 22 000.

The idea of controlling the flow by a change of the boundary condition shares some aspects with drag reduction approaches in which a partial slip boundary condition is obtained by (super)hydrophobic walls and surfaces [Watanabe *et al.*, 1999; Joseph and Tabeling, 2005; Neto *et al.*, 2005; Ou and Rothstein, 2005; Daniello *et al.*, 2009; Rothstein, 2010; Yao *et al.*, 2011; Lee *et al.*, 2014; Saranadhi *et al.*, 2016]. Slip on water repellent walls is usually realised in the range of nanometres. Only Saranadhi *et al.* [2016] report slip lengths of approximately 1 mm by using active heating on a superhydrophobic surface to establish a stable vapour layer (Leidenfrost state), which is already two orders of magnitude larger than that achieved by the aforementioned authors. In the present study, however, during the perturbation phase we move the wall by amounts that range from centimetres to meters, of the order of tens of pipe diameters. The method used has also common features with the moving surface boundary–layer control used to delay flow separation through momentum injection [Modi, 1997; Munshi *et al.*, 1999]. In contrast to the more common ways of separation control in boundary layers (suction, blowing, vortex generators, turbulence promoters, etc.), these authors use moving surfaces such as a rotating cylinder at the leading edge of a flat plate or bluff bodies as momentum injecting elements.

The outline of the paper is as follows. In Section 5.2 we describe the experimental

facility and the measurement techniques employed. In Section 5.3 we show the results of our investigation and in Section 5.4 we put them in perspective by discussing the physics and the mechanisms at play during and after the wall shift. Finally, in Section 5.5 we summarise our findings.

5.2 Experiments

5.2.1 Wall movement apparatus

The set–up consists of two consecutive straight stainless steel pipes (outer diameter $d_o = 25.4 \pm 0.13$ mm, length 2 m, wall thickness 0.4 ± 0.04 mm) which are connected by a coaxial Perspex pipe with a slightly larger diameter ($D = 26 \pm 0.1$ mm, length $L_{\text{total}} = 230D$). This segment can be shifted back and forth along the axial direction at an adjustable speed for a prescribed distance. Fig. 5.1 shows a sketch of the facility and indicates the arrangement of the measuring devices. The flow is driven by a constant pressure head. The movable Perspex segment is partially slipped over the upstream and downstream steel pipes (respectively labelled 1 and 2 in Fig. 5.1). The steel pipes are fixed to the base of the set–up and support the Perspex pipe that is free to slide along the axial direction. Four polymer sleeve bearings (Igus) provide additional support to the moving section and help to prevent bending and vibrations during the movement. Two radial shaft seals are placed in the gap between the inner wall of the moving section and the outer one of the steel pipes to avoid leakage. The actual length of pipe that can be moved to modify the pipe wall velocity is $L_{\text{control}} = 182 D$. Since the steel pipes have a smaller diameter than the control section, the flow experiences a small backward facing step at the end of the control section ($h = 0.7$ mm, $h/D = 0.027$). We employ a linear actuator (toothed belt axis with roller guide driven by a servomotor, ELGA-TB-RF-70-1500-100H-P0, Festo; not shown in the figure) mounted beneath the pipe and clamped to the Perspex pipe to actuate the control. The actuator can move the Perspex pipe for an adjustable distance (traverse path) $s \leq s_{\text{max}} = 1.5$ m at an adjustable velocity $U_w \leq U_{\text{w,max}} = 5.5$ m/s. The maximum possible acceleration is $a = 50$ m/s^2. Throughout the results presented
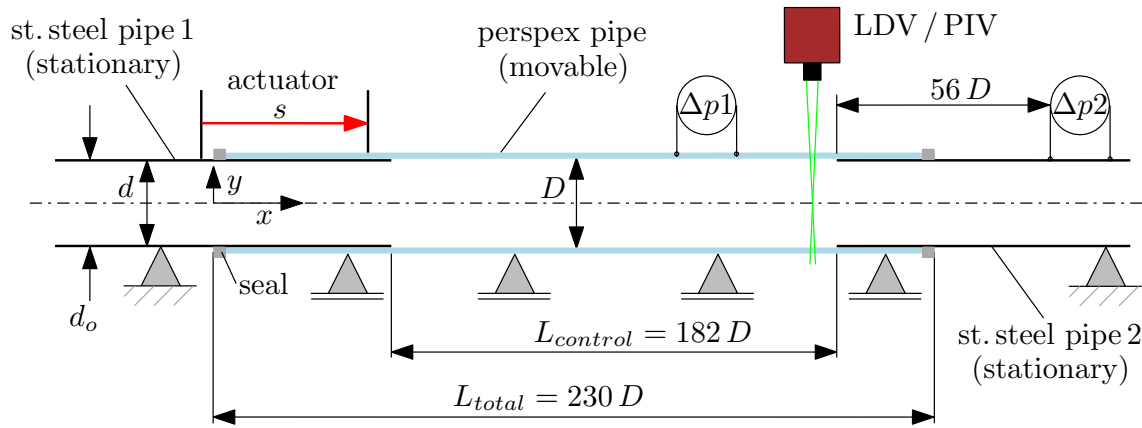
Figure 5.1: Sketch of the experimental set–up with a movable pipe segment. The movable pipe (perspex) is partly slipped over two stationary, very thin walled stainless steel pipes such that the perspex pipe overlaps the steel pipes at the upstream and downstream end. The perspex pipe is movable back and forth in the streamwise direction z for an adjustable distance s by means of a linear actuator. Drawing not to scale.

in the present work the acceleration and deceleration ramps were kept constant to $|a| = 10\,\text{m/s}^2$, unless otherwise specified.

In order to adjust the Reynolds number ($Re = U_b D / \nu$, where ν is the kinematic viscosity of the fluid and U_b the bulk velocity) we regulate a valve located upstream of the test section in the supply pipe (not shown). The flow rate is monitored with an electromagnetic flow meter (ProcessMaster FXE4000, ABB) and the fluid temperature with a Pt–100 resistance thermometer, both located in the feeding line. It is worth noticing that a change in the flow state (laminar or turbulent) in the test section does not appreciably affect Re, as the pressure drop difference along the main pipe (corresponding to ≈ 15 mm of water at $Re = 5000$) is negligible with respect to the total pressure head of ≈ 20 m. Hence, most of the pressure drop occurs across the regulation valve, which effectively keeps the mass flux (almost) constant throughout the measurements and in particular also during the wall acceleration. The overall measurement accuracy is $\pm 1\%$ for Re.

5.2.2   Measurement techniques

In order to investigate the flow behaviour during and after the wall shift we employ pressure drop measurements, particle image velocimetry (PIV) and laser Doppler

velocimetry (LDV). Pressure drop measurements can easily detect the flow status (turbulent or laminar) after the wall stops and allow for a precise assessment of the skin friction. However, they fail to accurately capture the fast dynamics during the wall movement and immediately afterwards because of set–up vibrations and the sensors slow response. The LDV system instead allows a more accurate description of the flow development throughout the experiment, although it does not provide information about the wall friction. The two–dimensional (2–D) PIV system offers a greater amount of data, but it is less suitable for investigations of a wide parameter space and it is hence used to study selected cases.

A first differential pressure sensor (DP 45, Validyne) is mounted onto the movable Perspex pipe $128\,D$ downstream of the beginning of the control section (distance measured when the actuator is not extended, $s = 0$). The transducer is connected to two pressure taps of diameter $0.5\,\text{mm}$, axial spacing $260\,\text{mm}$ and measures the pressure drop Δp_1. A second sensor (DP 45, Validyne) is mounted on the steel pipe 2, $56\,D$ downstream the end of the control section. The taps have a diameter of $0.5\,\text{mm}$ and an axial spacing of $197\,\text{mm}$ and are associated with the pressure drop Δp_2. A great deal of care has been taken to stabilise the sensor housings and related wiring and piping during the impulsive pipe movement, especially to ensure repeatability. Overall, the measurement accuracy is $\pm 1.2\,\text{Pa}$.

At the downstream end of the movable Perspex section, $5\,D$ upstream of steel pipe 2, the centreline velocity U_c is measured by means of a one–component LDV system (TSI). Water is seeded with neutrally buoyant, hollow glass spheres of diameter $13\,\mu\text{m}$ (Sphericel, Potter Industries). The resulting average measurement rate is 20 Hz.

A 2–D PIV system is set to monitor the flow along a longitudinal section of the movable pipe segment. The window is $1.5\,D$ long, centred in the same location as the LDV and passes through the centreline of the pipe. In order to decrease the distortion caused by refraction we enclose the aforementioned pipe segment in a rectangular, water filled Perspex box. A continuous laser (Fingco 532H-2W) illuminates the measurement plane with a sheet of light of nominal thickness $\approx 1\,\text{mm}$. PIV images are recorded with a high–speed camera (PhantomV10) mounted vertically above

the water filled box. The flow is seeded with the same hollow glass spheres used for the LDV measurement. The system is used to produce a 2D velocity field over a domain $1.5D \times D$ of resolution 87×56 vectors at a frequency of 50 Hz. The image post–processing is carried out with the software Davis 8 (LaVision).

We also employ neutrally buoyant anisotropic particles (Mearlmaid Pearlessence) for visualising the flow state during and after the wall movement and for coarsely exploring the experimental parameter space. The particles have the form of elongated platelets that align with the local shear and possess high reflectivity allowing to observe flow structures [Matisse and Gorman, 1984]. An LED string is placed along the whole length of the movable Perspex pipe and illuminates the flow, enabling an easy detection of laminar and turbulent states both by the naked eye and camera.

In the following we refer to a coordinate system as indicated in Fig. 5.1, where x measures the axial direction along the flow and y the wall–normal direction starting at the centreline. The respective Cartesian velocity components are U and V.

5.3   Results

In an initial set of experiments we set $Re = 5000$ and progressively increase the wall shift length s while the wall velocity U_w is kept equal to the bulk velocity U_b. The flow is monitored at the downstream end of the transparent pipe. As the shift length s is increased, relaminarisation events begin to occur up to the point when at each actuation the flow consistently and repeatedly relaminarises for $s \gtrsim 8D$. It is important to note that the turbulence decay process takes place after the wall stops, so that the controlled patch of fluid is advected downstream while relaminarising. Fig. 5.2 shows still pictures from a typical run (video available online). An initially fully turbulent flow at $Re = 5000$ ($t < 5\,\mathrm{s}$) is subjected to an abrupt wall shift ($5 < t < 7\,\mathrm{s}$) for a length $s = 9D$ and wall speed $U_w = U_b$. After the wall stops, turbulent structures are still visible through the pipe (second panel in Fig. 5.2). Nevertheless, they gradually decay and the flow reverts to the laminar state. Since laminarisation only occurs in the moved section, finally the laminarised flow patch is advected past and replaced by the upstream turbulent flow ($t > 30\,\mathrm{s}$).
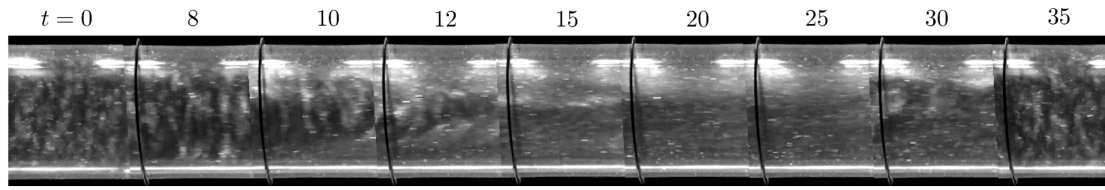
Figure 5.2: Still pictures from the supplementary video. Each frame shows a $1\,D$ long section of the movable Perspex pipe at $Re = 5000$, $s = 9D$ and $U_w = U_b$. Time t is measured in seconds. The wall is moved for $t = 5 - 7$ s. The black ring around the pipe is used to highlight the movement of the wall. Video available online at https://doi.org/10.1017/jfm.2019.191.

Fig. 5.3 shows the complete relaminarisation of a $Re = 8000$ turbulent flow in terms of (a), average centreline velocity measured with PIV, (b) and (c), pressure drop Δp_1 and Δp_2, respectively. The wall shift is $s = 12D$ at $U_w = U_c \approx 1.3U_b$, where U_c is the average centreline velocity of the turbulent flow. The vertical dashed lines represent the first and last instant of wall motion. The dotted line marks the theoretical laminar pressure drop. During the wall shift the centreline velocity decreases steeply from $\approx 1.3U_b$ to $\approx 1.1U_b$ (Fig. 5.3 (a), $-10 < t < 0$). This reduction of the flow speed at the pipe centre is a direct consequence of the acceleration of the near–wall fluid in conjunction with the effectively constant mass flux condition. During the wall motion no reliable information is available from the pressure sensors (the signal goes off scale in Fig. 5.4 (b)), as a consequence of a rapid wall shear change and vibrations induced by the impulsive motion. Immediately after the wall stops the flow is steadily developing towards a parabolic profile, until it is advected past the measurement point. This is well captured in Fig. 5.3 (c), where at a slightly later time the downstream pressure taps record the passage of a short patch where the flow has fully relaminarised. The large overshoots visible in the pressure signals indicate the passage of the turbulent–laminar interface across the taps. It is worth noticing at this point that the laminarising patch stayed laminar even after passing over the step between the Perspex and steel pipes.

A more precise insight into the dynamics during the wall motion is provided by Fig. 5.4 (a). Here we show the temporal evolution of the axial velocity measured by 2–D PIV. Each profile is averaged along the x–axis of the PIV window and is labelled with the number of advective time units elapsed since the end of the wall
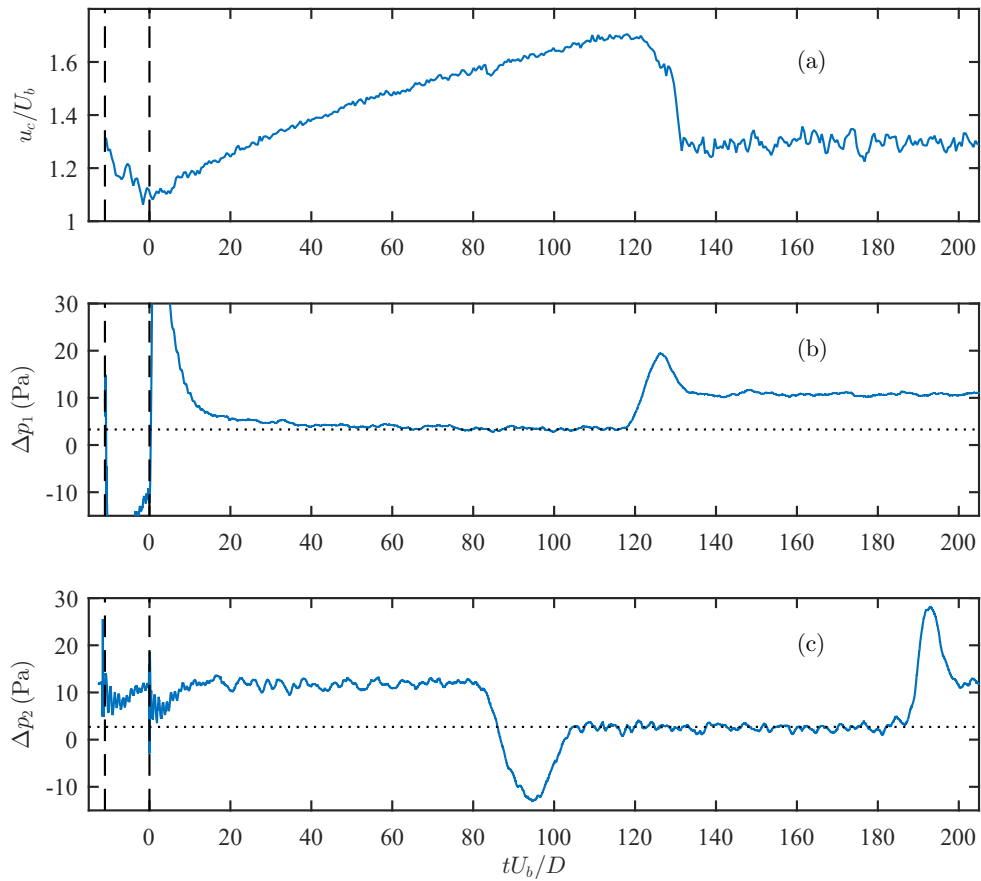
Figure 5.3: Relaminarisation of a turbulent flow at $Re = 8000$ with wall shift $s = 12D$ and wall velocity $U_w = U_c$. (a) Centreline velocity over time measured by 2–D PIV. Each point is obtained by averaging the measured centreline velocity over $1.5D$ for each frame. (b) Pressure drop Δp_1 over time read by the transducer mounted on the moving section. The off–scale portion of the signal reaches approximately -30 and 50 Pa. (c) Pressure drop Δp_2 over time read by the second transducer mounted downstream the moving section. The vertical dashed lines represent the first and last instant of wall motion. The dotted line marks the theoretical laminar pressure drop.
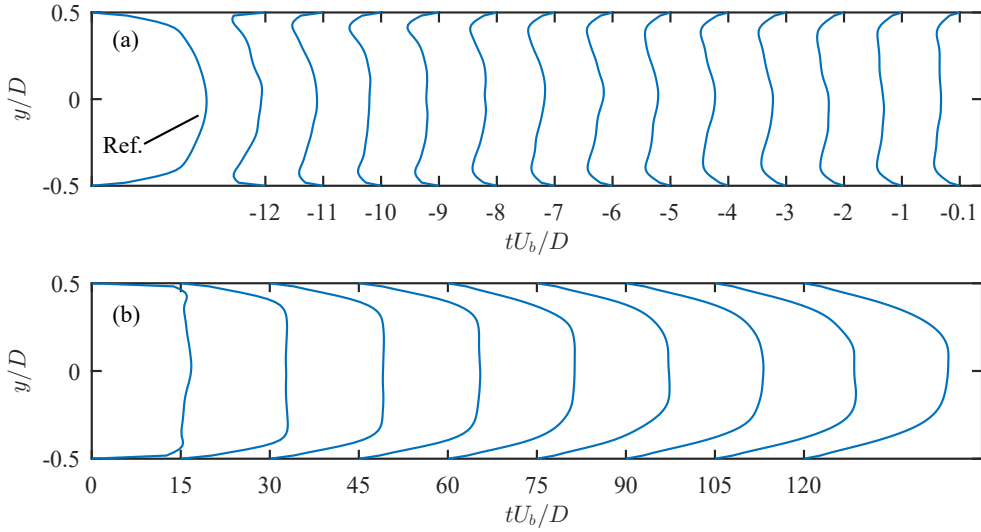
Figure 5.4: Temporal evolution of the mean axial velocity during (a), the wall movement and (b), after it. The Reynolds number, wall shift length and velocity are $Re = 8000$, $s = 12D$ and $U_w = 1.3U_b$, respectively. Time is measured in advective units starting from the end of the wall motion.

movement. The profile marked as Ref. represents the undisturbed turbulent flow. At the beginning of the wall motion ($tU_b/D = -12$) the effect of the moving wall is confined to a region close to the wall. As time proceeds further, also the flow in the core region becomes progressively affected by the new boundary condition and the mean velocity assumes a flatter distribution. The flow development afterwards is shown in Fig. 5.4 (b). Immediately after the wall has stopped, the no–slip velocity boundary condition is restored and the flows assumes a plug–like profile. From hereafter the flow develops towards parabolic, culminating in a centreline speed $U_c/U_b \approx 1.7$ before the laminar patch is advected downstream the observation window.

The fate of the flow appears to depend only on the steady wall velocity and on the shift length during the wall motion phase. The acceleration ramp before and the deceleration ramp after do not appear to affect the results in the range of accelerations investigated, as shown in Fig. 5.5. Here we compare the pressure signal Δp_1 for three relaminarising cases at $Re = 10\,000$ with accelerations values of $|a| = 2, 5, 10$ m/s^2 in solid (blue online), dashed (red online) and dot–dashed line (yellow online), respectively. Each signal is obtained by averaging three different
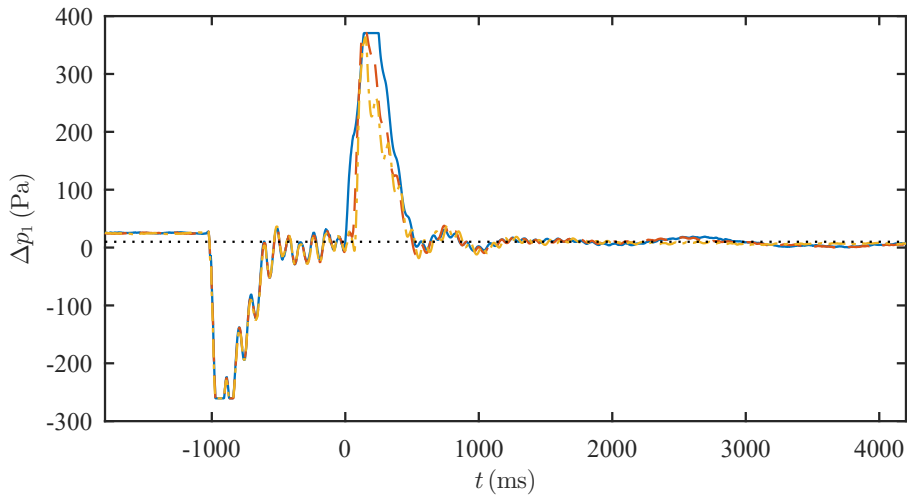
Figure 5.5: Pressure signal Δp_1 of relaminarizing experiments at $Re = 10\,000$, for $s = 16D$ and $U_w = U_c \approx 1.3U_b$. Solid (blue online), dashed (red online) and dot–dashed (yellow online) lines correspond to accelerations $|a| = 2, 5, 10$ m/s^2. Each line is obtained by averaging three different runs. The dotted line represents the laminar pressure drop.

runs to highlight coherent oscillations due to physical vibrations. Wall shift and wall velocity are $s = 16D$ and $U_w = U_c \approx 1.3U_b$, respectively. The dotted line represents the laminar pressure drop.

We next explore how the shift length affects the laminarisation process. In these runs the flow status is monitored with LDV to detect laminar patches and measure their lengths. Fig. 5.6 shows the minimum shift length required for laminarisation (hereafter referred to as the critical shift length s_c) versus Reynolds number for two wall velocities, $U_w = U_b$ (squares, blue online) and $U_w = U_c$ (circles, red online). The dashed lines are a linear fit to the data. For $Re \lesssim 5000$ we do not observe any difference between the two velocities. Each point of the plot corresponds to a set of measurements where we increase s and we keep the wall velocity constant. The inset of Fig. 5.6 shows one such dataset, where the mean length of the laminar patch Δt is plotted versus s, for $U_w = U_b$ (squares, blue online) and $U_w = U_c$ (circles, red online). Error bars represent the standard deviation. The Reynolds number is $Re = 10\,000$. As the shift s is increased, the duration of the laminar flow increases. While for small s only a fraction of the flow in the moving section laminarises, for increasing shift length the laminar fraction grows swiftly until at $s = s_c$, where
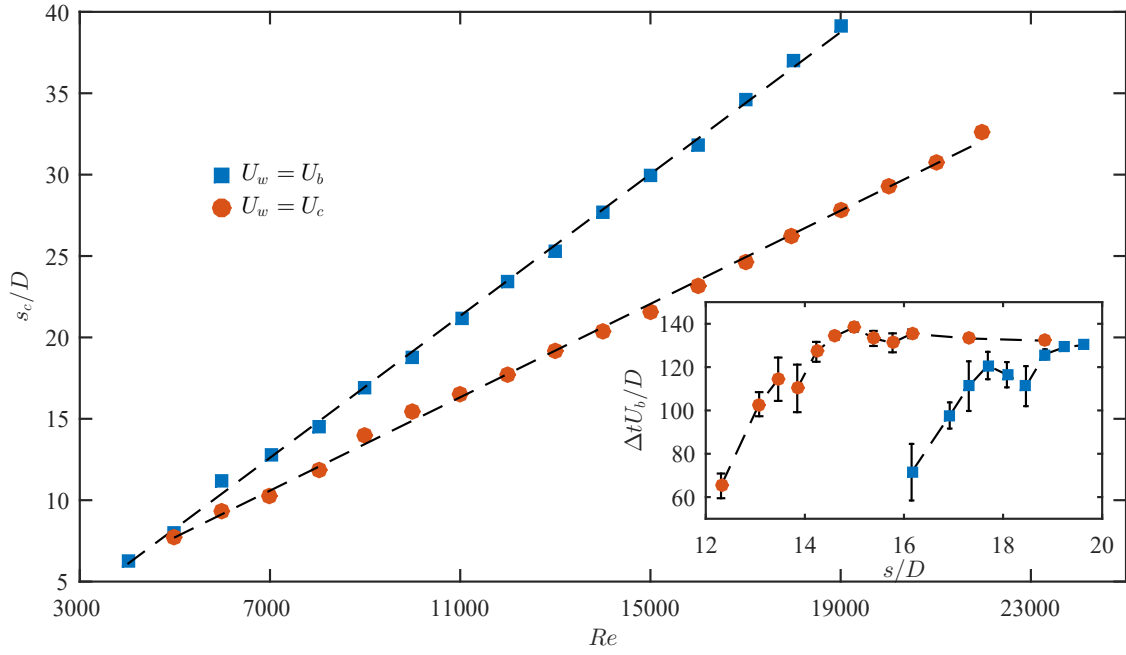
Figure 5.6: Critical shift length s_c for relaminarisation versus Re. Squares (blue online) and circles (red online) are datasets for $U_w = U_b$ and $U_w = U_c$, respectively. Dashed lines are a linear fit to the data. The inset shows the datasets used to assign the critical shift length for $Re = 10\,000$. The average laminar patch duration Δt is plotted against s. Error bars represent the standard deviation.

approximately the entire fluid in the moving segment laminarises. After this steep increase of the laminarising section with s, for even larger shifts the laminar patch only grows at a far slower rate (by $s - s_c$). This slow linear growth is not visible in the inset of Fig. 5.6 inset and hence the laminar patch size appears to reach a plateau.

Next, we explore the influence of the wall velocity as the shift length is held constant. For each Re we pick the critical shift length s_c for $U_w = U_b$ from Fig. 5.6. For this shift length and Re we then vary the wall speed and determine the speed range over which relaminarisation occurs. The minimum and maximum speed required is given respectively by the open and full symbols in Fig. 5.7. Each data point is found analogously to the search for the critical shift length. As the Reynolds number increases, the allowable shift velocity range decreases rapidly while the minimum velocity seems to be independent of Re. Interestingly, at low Reynolds numbers ($Re < 6000$) arbitrary large wall velocities lead to relaminarisation, for a shift equal to the critical value obtained with $U_w = U_b$. The maximum velocity
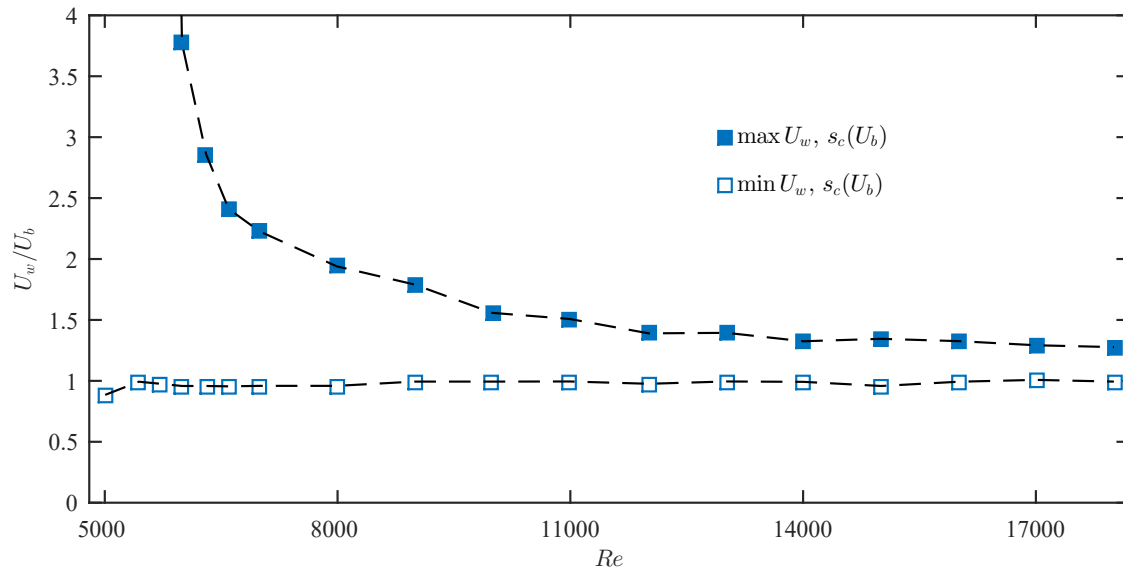
Figure 5.7: Admissible values of wall velocity U_w as a function of Reynolds number Re. The empty and full symbols represent respectively the minimum and maximum wall velocity necessary to relaminarise the flow with a critical shift length s_c obtained from the data of Fig. 5.6 for $U_w = U_b$. At $Re = 5000$ laminarisation was achieved up to $U_w = 40U_b$ (point not shown in the figure).

tested was $U_w = 40U_b$ at $Re = 5000$ (point not shown in the figure) and the flow fully relaminarised. Here we had to increase the acceleration to the maximum allowable value to reach the prescribed velocity.

5.4   Discussion

The control strategy presented is effective in suppressing turbulence in the flow region perturbed by the wall and it allows us to study the flow development to the laminar state for a wide range of Reynolds numbers. In Fig. 5.8 we compare the temporal evolution of the centreline velocity measured by LDV (left column) and the average friction factor $f = 2\Delta p_1 D/(\rho U_b^2 L_{\text{taps}})$ (right column), where ρ is the water density and L_{taps} is the distance between the two pressure taps. The corresponding Reynolds numbers are $Re = 10\,000$ (top row), $Re = 15\,000$ (central row) and $Re = 20\,000$ (bottom row). In this set of experiments we increased the length of the movable Perspex pipe to $L_{\text{control}} = 385D$ to extended the duration of laminar flow. The evolution of U_c and f is compared with the development of a
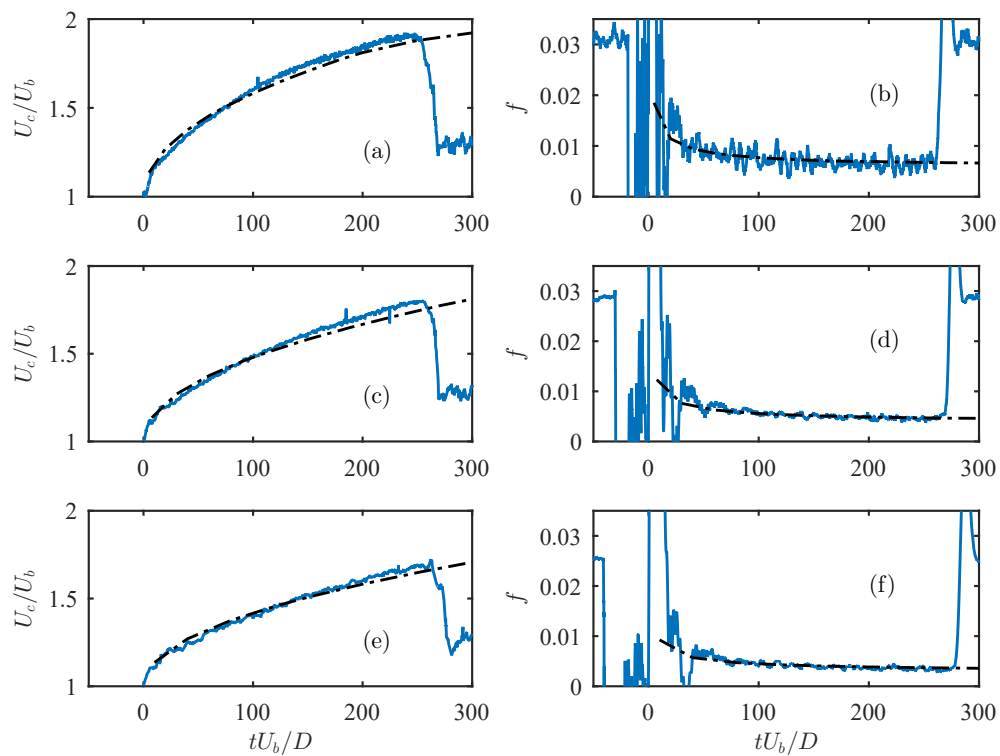
Figure 5.8: Centreline velocity U_c (left column) and friction factor f (right column) as a function of time for relaminarising flow at $Re = 10\,000$ (top row), $Re = 15\,000$ (central row) and $Re = 20\,000$ (bottom row). The wall stops at $t = 0$. For the three cases $U_w = U_b$ and $s = s_c$. The dash–dotted line represents the development of a plug–like flow from a pipe entrance according to Mohanty and Asthana [1979].

plug–like flow from a pipe entrance (dash–dotted line) according to the findings of Mohanty and Asthana [1979] and our data are in very good agreement with their prediction. To allow the comparison, we make the end of the wall motion ($t = 0$) coincide with the entrance of the pipe and express the development in terms of advective time units. The friction factor adjusts rapidly to the one computed with the entrance problem model, thus suggesting that the transition from turbulent to laminar might happen rather quickly ($\lesssim 20D/U_b$), and then the mean flow is nearly indistinguishable from a plug velocity profile evolving into parabolic form. In addition, since the profile develops gradually from the wall, the friction factor approaches the laminar value much faster than the centreline velocity (cf. also Fig. 5.4 (b)). Hence, a substantial drag decrease is obtained long before the laminar profile is fully developed.

The time available to observe the flow laminarising is constrained by the length of the control section and the shrinking of the laminar stretch which is being entrained by the surrounding turbulent flow (for entrainment rates of the turbulent fronts see *e.g* Wygnanski and Champagne [1973], Nishi *et al.* [2008] and Barkley *et al.* [2015]). In particular, the turbulent front upstream of the laminar flow aggressively entrains it at rate that increases with Reynolds number.

We next focus on the physical mechanism responsible for the collapse of turbulence. As shown by Kühnen *et al.* [2018c], flatter, more plug–like velocity profiles can induce the flow to laminarise as a consequence of a reduced creation of velocity streaks by streamwise vortices (lift–up mechanism). To quantify the lift–up potential the authors analysed the maximum level of the transient growth (TG) function, defined as

$$G(t) = \max_{q_0 \neq 0} \frac{||q(t)||^2}{||q_0||^2}, \tag{5.1}$$

where $q(t)$ is the evolution of an initial disturbance q_0 of the base flow about which the Navier–Stokes equations are linearised, and $|| \cdot ||$ is an energy norm. We refer the reader to Schmid and Henningson [2001] and Meseguer and Trefethen [2003] for further details and the numerical procedure to compute TG. In the present investigation we compute the transient growth by taking the measured mean velocity profile as base flow. Streamwise vortices become inefficient if the velocity profile is
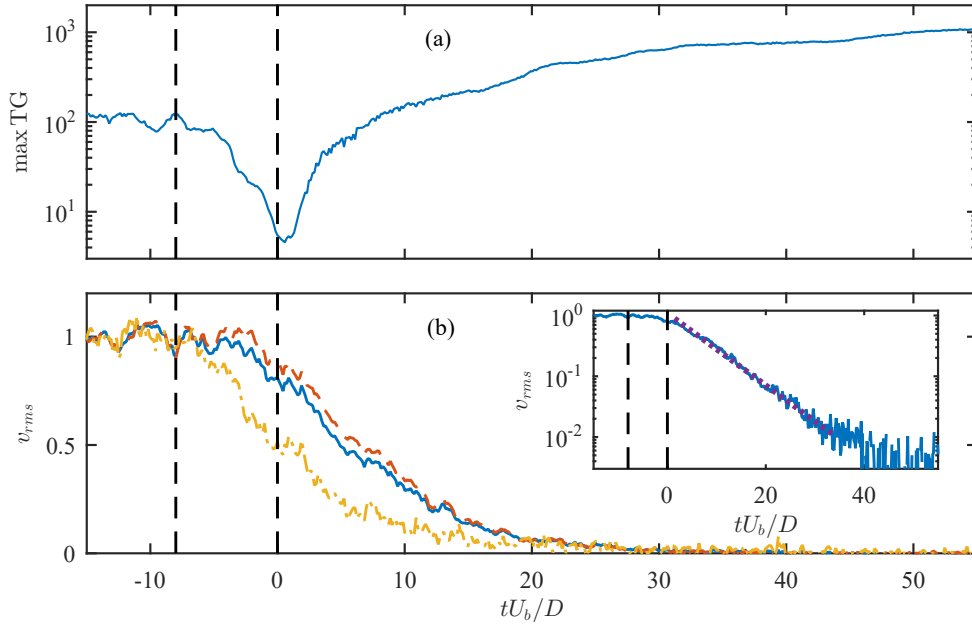
Figure 5.9: Time evolution of (a), transient growth of the mean axial velocity and (b), mean wall–normal fluctuations over $0 \leq y \leq D/2$ (solid line, blue online), $0.35D \leq y \leq D$ (dash–dotted line, yellow online), and $0 \leq y \leq 0.35D$ (dashed line, red online). The vertical dashed lines indicate the beginning and the end of the wall movement. The data is obtained by averaging 10 runs at $Re = 5000$, with $U_w = U_b$ and $s = 9D$. Inset, log–lin plot of the mean wall–normal fluctuations averaged for $0 \leq y \leq D/2$ (solid line, blue online) and exponential fit (dotted line, purple online).

flat and only very weak streaks can be created (*i.e.* the lift–up mechanism breaks down, see *e.g.* Brandt [2014]). As shown by Kühnen *et al.* [2018c], the maximum value of TG provides a measure of the reduction of the lift–up process. While Kühnen *et al.* [2018c] demonstrated that several diverse relaminarising flows had lower levels of maximum TG, we here consider the temporal evolution of the relaminarisation process in order to test the validity of this argument. As shown in Fig. 5.9 (a), after the wall is set into motion, the maximum TG starts to reduce and it does so at an increasing rate until the wall motion stops, which coincides with the minimum TG value reached. This sequence is in line with the development of the velocity profile (shown in Fig. 5.4 (a) for a different Re). The profile is not immediately flattened after the wall motion starts, but it first needs to adjust. As shown in Fig. 5.9 (a), during the interval of wall motion TG drops by approximately a factor of 20. We would expect that the fluctuation levels in the near–wall region (*i.e.* where

production takes place) react first and this is indeed the case, as demonstrated in Fig. 5.9 (b), where we show the time evolution of the wall–normal velocity fluctuations

$$v_{rms} = \sqrt{\langle (V - \langle V \rangle)^2 \rangle},$$ (5.2)

where $\langle . \rangle$ denotes averaging across the axial coordinate of the PIV window. The mean fluctuations in the wall region ($0.35D \leq y \leq D/2$, dash–dotted line, yellow online) closely follow the drop in TG while the average fluctuation level in the core region ($0 \leq y \leq 0.35D$, dashed line, red online) lags behind. In particular the strongest drop in the overall fluctuations (solid line, blue online) is assumed only somewhat after the minimum in TG has been reached, *i.e.* after the wall has stopped. While afterwards the TG level begins to rise, the value remains considerably lower than that of the average turbulent profile at this Re. Hence fluctuation levels keep decreasing. Eventually, when TG has regained its initial level ($tU_b/D \approx 10$), the fluctuations, in particular in the near wall region, are very low and turbulence does not recover. Instead the profile becomes increasingly parabolic (cf. Fig. 5.4 (b)) and TG consequently continues to grow.

As shown in the inset of Fig. 5.9 (b), the decrease of the mean v_{rms} that occurs after the wall motion is stopped can be approximated by an exponential. In this regime fluctuations drop by more than an order of magnitude in 20 advective time units. The exponential decay is also consistent with the findings of Kühnen *et al.* [2018b] in the case of the relaminarising flow past an orifice plate obstacle. Qualitatively, above findings also agree with the recent work by Marensi *et al.* [2019], who investigated numerically the robustness of optimal turbulence seeds in presence of a flat profile. In particular, the authors observed that a flatter base flow requires a greater initial disturbance energy and at the same time induces a smaller energy growth of the disturbances.

Revisiting the data shown in Fig. 5.6, it appears that the shift length, and hence the time required to flatten the profile, scales linearly with the Reynolds number. In order to explain this trend, we look into the mechanism by which the axial velocity is progressively modified starting from the wall until it becomes flatter in the core region (see Fig. 5.4 (b)). To realise a plug profile, the new boundary condition

established at the wall has to affect the entire flow up to the pipe centre. While at the beginning of the wall motion turbulent stresses are present and may contribute to diffusing the wall velocity, their effect quickly dampens out as the profile gets flatter and turbulent kinetic energy production is reduced. This is also reflected in lower values of the velocity fluctuations in the wall region with respect to the core (cf. fig 5.9 (b)). Thus, we assume that the necessary profile modification occurs in viscous time scales and we propose that the adjustment up a to a distance δ from the wall requires a time

$$t \sim \frac{\delta^2}{\nu}. \tag{5.3}$$

Substituting $\nu = U_b D / Re$ gives

$$t \sim \frac{\delta^2}{U_b D} Re, \tag{5.4}$$

and hence, for a spread to the pipe centre $\delta \sim D/2$ we have

$$t \sim \frac{D}{U_b} Re. \tag{5.5}$$

The dimensionless time in advective time units $t U_b / D$ is then proportional to Re. Owing to the advective nature of the flow, the linear growth of the necessary time for which the wall motion is active translates to a minimum streamwise length that needs to be exposed to the changed boundary conditions. This observation also explains why a related control strategy where the flow is accelerated by streamwise fluid injection at a fixed location only works for a finite Reynolds number range [Kühnen *et al.*, 2018b].

Finally, we discuss the possibility of using the moving wall mechanism to laminarise the flow for saving energy. To this end, we introduce an integral measure that accounts for the energy dissipated by the flow over the control length as

$$E = \int_0^T Q \Delta p(t) dt, \tag{5.6}$$

where $\Delta p(t)$ is the instantaneous pressure drop across L_{control}, $Q = U_b \pi D^2 / 4$ is the constant flow rate and T is the time when the laminarised flow patch exits the control section, measured with respect the end of the wall motion ($t = 0$). We conservatively did not account for the flow during the wall shift, as the actuator

moves along the flow direction, thus resulting in a transfer of kinetic energy from the flow to the actuator (Δp_1 is mostly negative during the wall motion). The power dissipated by the actuator in the real experiment is not modelled in our estimate. To measure $\Delta p(t)$ we divide the control section into a shrinking laminarising patch and an expanding fully turbulent region. The friction factor of the laminarising region is the one measured and reported in the plots of Fig. 5.8. The advection speed of the turbulent–laminar front is assumed to be $\approx 1.6 U_b$, consistently with the observations of Wygnanski and Champagne [1973]. The amount of energy saved is expressed by the ratio

$$R = \frac{E_0 - E_c}{E_0},\tag{5.7}$$

where E_0 and E_c are computed with equation (5.6) in case of fully developed turbulent flow and the moving wall case, respectively. For a control length $L_{\text{control}} = 182D$ and a wall velocity $U_w = U_b$ we obtain a net energy saving of $R = 0.31$ and $R = 0.35$ for Reynolds numbers $Re = 10\,000$ and $Re = 20\,000$, respectively.

5.5   Conclusions

We demonstrated that upon an abrupt acceleration of the near–wall fluid, the transient growth level of the overall flow is strongly suppressed and subsequently turbulent (wall–normal) fluctuation levels drop exponentially. While at low Re (≈ 5000) arbitrarily large wall speeds lead to relaminarisation, at higher Re only wall speeds close to the bulk flow speed lead to a decay of turbulence. Moreover the wall motion required to accelerate the near–wall fluid has to act for a minimum time in order to create the desired plug flow, because the velocity profile adjusts viscously from the boundaries. This requirement severely limits the applicability of such relaminarisation schemes that affect the flow only at the boundaries, since due to the advective nature of the flow it effectively means that the control has to act over a minimum distance in the streamwise direction which increases linearly with Re. It should be noted that such limitations do not apply if the profile can be adjusted via a volume force as shown by a numerical forcing scheme by Kühnen *et al.* [2018c]. As those authors demonstrated relaminarisation under such conditions

can even be achieved at *Re* as large as 100 000.

---

6 Relaminarization of pipe flow by means of 3D–printed shaped honeycombs

Based on a novel control scheme, where a steady modification of the streamwise velocity profile leads to complete relaminarization of initially fully turbulent pipe flow, we investigate the applicability and usefulness of custom–shaped honeycombs for such control. The custom–shaped honeycombs are used as stationary flow management devices which generate specific modifications of the streamwise velocity profile. Stereoscopic particle image velocimetry and pressure drop measurements are used to investigate and capture the development of the relaminarizing flow downstream these devices. We compare the performance of straight (constant length across the radius of the pipe) honeycombs with custom–shaped ones (variable length across the radius) and try to determine the optimal shape for maximal relaminarization at minimal pressure loss. The optimally modified streamwise velocity profile is found to be M–shaped, and the maximum attainable Reynolds number for total relaminarization is found to be of the order of 10 000. Consequently, the respective reduction in skin friction downstream of the device is almost by a factor of 5. The break–even point, where the additional pressure drop caused by the device is balanced by the savings due to relaminarization and a net gain is obtained, corresponds to a downstream stretch of distances as low as approximately 100 pipe diameters of laminar flow.

6.1 Introduction

A variety of methods to reduce skin friction in pipes has been proposed over the years. Amongst the most popular ones are engineered surfaces (*e.g.* riblets [Garcia-Mayoral and Jiménez, 2011] and superhydrophobic surfaces [Rothstein, 2010; Geraldi *et al.*, 2017]) and the addition of polymers [Jovanović *et al.*, 2005; Campolo *et al.*, 2015]. Up to now only the latter seems to have been successfully implemented in practical applications. Polymers directly interact with the dynamics of turbulence [White and Mungal, 2008; Choueiri *et al.*, 2018] and can hence considerably reduce the turbulent skin friction drag in pipes.

As recently shown by Kühnen *et al.* [2018c], a suitable steady modification of the streamwise velocity profile in a pipe can lead to a total collapse of turbulence and the flow completely relaminarizes, representing the optimum in terms of friction and energy saving. The required alteration of the profile was shown to be such that the controlled streamwise velocity profile was (more) flat or even dented in the center of the pipe, requiring that the flow close to the wall is accelerated and the flow in the center of the pipe is decelerated as compared to the uncontrolled flow. In their numerical simulations Kühnen *et al.* [2018c] added an appropriate radially dependent body force term to the equation of motion, modifying the streamwise velocity profile to a more plug–like one. In experiments, several practical techniques to modify the mean velocity profile of turbulent flow were shown to be feasible. One technique was by stirring the flow with four rotors. Another approach, elaborated in Scarselli *et al.* [2019], was by means of a shiftable segment of the pipe used to locally accelerate the flow near the wall. A further approach, elaborated in Kühnen *et al.* [2018b], was by injecting fluid through an annular gap at the wall to accelerate the flow close to the wall or by inserting an obstacle partially blocking the pipe. All approaches act on the velocity profile in a comparable way and can modify the streamwise velocity profile appropriately to achieve relaminarization. The experiments demonstrated that relaminarization happened as a direct result of a specific streamwise velocity profile which exhibited a severely decreased lift–up potential that can not sustain turbulence. A related phenomenon exists for laminar

pipe flow profiles. Marensi *et al.* [2019] have shown that the non–linear stability of the laminar state is enhanced as the initially parabolic profile becomes more flattened.

In the present investigation we want to explore a further possibility of specifically modifying the streamwise velocity profile employing passive [Perlin *et al.*, 2016] flow management devices. The aim is to modify the streamwise velocity profile in a pipe similar to Kühenen *et al.* [2018b] by solely passive means to achieve complete relaminarization of initially fully turbulent pipe flow.

To homogeneously force the streamwise velocity profile in a pipe a very fine meshed screen with radially varying mesh size may seem the simplest choice; however unwanted apart from modifications of the streamwise velocity, such screens also cause cross stream components which can prevent relaminarization. It is clear that any physical body inserted into the flow, be it as small as technically feasible, can reduce the level of existing turbulence and control the flow profile — but it can at the same time also produce flow inhomogeneities and turbulent structures.

Screens have been used for decades to reduce or suppress turbulence, to break down incoming large–scale structures and to make the flow more uniform in all kinds of applications such as wind and water tunnels. The various types of screens are commonly referred to as grid, mesh, sieve, woven wire, gauze or, if the device is markedly extended in the streamwise direction, honeycomb. A further distinction can then be made between real honeycombs (regular hexagonal cells) and other types of cells, *e.g.* square cells or circular cells like in devices made of drinking straw [Mikhailova *et al.*, 1994]. Screens can be generally seen as flow conditioners which damp or even extinguish the incoming, upstream turbulence and largely diminish velocity or pressure nonuniformities. The suppression of turbulence is mostly either due to the inhibition of lateral (transverse) components of the flow or the breaking up of large–scale turbulence into smaller, isotropic, more rapidly decaying turbulence, both obtained at the cost of an additional pressure drop across the screen. In any application this penalty is to be weighed against the positive effect of turbulence reduction. Since screens can also generate, primarily through documented instabilities, new turbulence with scales characteristic of the shear

layers present in their near wake downstream, the control of turbulence by means of screens and honeycombs is always a balance between suppression and generation [Loehrke and Nagib, 1976].

Concise discussions concerning suppression of turbulence by screens can be found in *e.g.* Bradshaw and Pankhurst [1964], Laws and Livesey [1978], Groth and Johansson [1988] and Oshinowo and Kuhn [2000] and references therein. The honeycomb type of screens, which are generally useful for turbulence reduction if swirl or initially high transverse velocities are present, is discussed in *e.g.* Loehrke and Nagib [1976], Lumley and McMahon [1967], Farrel and Youssef [1996] and Kulkarni *et al.* [2011]. However, the data available on honeycombs is rather limited and mainly given as best practice and empirical laws from experiments. The usage of screens to increase turbulence levels or to generate quasi–isotropic turbulence [Roach, 1987; Liu *et al.*, 2007], often used to investigate dissipation and naturally decaying free–stream turbulence downstream the screen [Oshinowo and Kuhn, 2000; Valente and Vassilicos, 2011; Vassilicos, 2015], is an operational mode which will not be considered further in the present context.

Kotansky [1966], Livesey and Laws [1973], Sajben *et al.* [1975] and Ahmed and Lee [1997] have successfully used screens and honeycombs to produce artificial, more or less well controlled velocity profiles in free–stream turbulence. They demonstrated that the velocity profile downstream of screens or honeycombs can be controlled via a variation of the mesh size or the cell length. Since in the present investigation the variation of the mesh size is limited by the capabilities of the 3D–printer (see the section on the flow management device), the present work is confined to varying the cell length of regular hexagonal honeycombs across the cross section of the pipe. *I.e.*, we employ shaped honeycombs to generate a particular profile of the streamwise velocity. The success of the relaminarization devices in our study predominantly appears to depend on the shape of the generated streamwise velocity profile. The suppression of turbulence due to the inhibition of transverse components certainly also plays a role but to a lesser extend. As an attempt to distinguish the effect of the forcing on the streamwise profile from normal turbulence suppression through the annihilation of transverse fluctuations we also present results of unshaped

honeycombs, where all cell lengths are equal.

The paper is structured as follows: in the next section we describe the experimental setup, the method and the custom 3D–printed honeycomb–devices which were used to generate velocity profiles. Then we describe the examination procedure and the steps to systematically find the optimal flow profile and produce a specified profile with the least effort in terms of pressure drop. The results are finally presented and discussed in the last section.

6.2 Experimental setup and method

The test facility consists mainly of a straight long glass pipe with turbulent flow. 3D–printed honeycomb devices act as flow management devices (FMDs) which can be mounted within the pipe between two pipe sections. The FMDs form a targeted obstruction representing a spatially extended volume forcing on the flow. The facility allows to investigate the effect of the FMDs on the flow. In the following section the facility and the FMDs are described in detail.

Facility

Fig. 6.1 shows a sketch of the test facility used to test different FMDs. The facility consists of a pipe made of glass with inner diameter $D = 30 \pm 0.01$ mm. The total length of the pipe is 9 m (300 D). Water driven by gravity enters the pipe from a
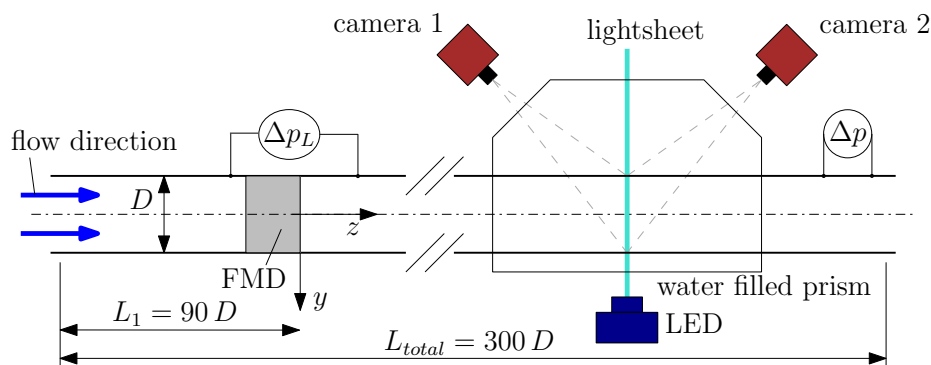
Figure 6.1: Sketch of the test facility. Different flow management devices (see Fig. 6.2 for details) can be mounted inside a glass pipe. The flow direction is from left to right. Drawing not to scale.

reservoir located 20 m above the pipe. The flow rate and hence the Reynolds number ($Re = UD/\nu$, where U is the mean velocity, D the diameter of the pipe and ν the kinematic viscosity of the fluid) can be adjusted by means of a control valve (located in the supplying pipe). The Reynolds number is held constant within ±1.14% with 95% confidence throughout all the measurements.

We measure the velocity field with a stereoscopic particle image velocimetry (PIV) system, where the measurement plane is perpendicular to the streamwise flow ($z-$axis of the pipe). The system consists of a pulsed LED (IL-106X LED Illuminator, HARDsoft Microprocessor Systems) and 2 Phantom V10 cameras (Vision Research Inc.) with a resolution of 2400×1900 px. The cameras are arranged in a backward backward–scattering configuration and calibration is performed by using a two–sided, two–level calibration plate (LaVision GmbH). Images are processed in Davis 8.1.3 (LaVision GmbH) by using two passes with 64×64 pixels interrogation windows and 2 passes with 48×48 pixels interrogation windows. The overlapping ratio is set to 50%. The resulting vector fields are further post–processed to remove vectors with a peak ratio $Q < 1.3$ and fill up empty spaces with linear interpolation. Vestosint particles (mean diameter 45 μm, $\rho = 1.016$ g/cm^3, Evonik Degussa GmbH) are used as seeding particles. We use a local non–dimensional Cartesian coordinate system $(x, y, z) = (\tilde{x}/D, \tilde{y}/D, \tilde{z}/D)$ as indicated in Fig. 6.1, where the downstream end of the FMD is always located at the origin. The respective Cartesian velocity components $(\tilde{u}, \tilde{v}, \tilde{w})$ are made non–dimensional by dividing them by the mean velocity U, yielding (u, v, w). Around the position of the light sheet the pipe is encased by a prism filled with water to make sure that the optical axes of the cameras are orthogonal to the air–water interface to reduce distortion and refraction. By placing the FMD 90 D downstream the inlet of the pipe we make sure to have fully developed turbulence right upstream the FMD [Zagarola and Smits, 1998].

To measure the pressure drop Δp between two pressure taps we use a differential pressure sensor (DP 103, Validyne). As turbulent flows experience a skin drag much higher than the laminar one and in addition, the difference becomes larger as the Reynolds number increases, we use Δp for a straightforward detection of the flow state based on the huge difference between the respective friction factors (f_{turb} and

f_{lam}). For this purpose the sensor is placed at the downstream end of the pipe as indicated in Fig. 6.1, and the pressure taps are separated by $30\,D$ in the streamwise direction. For $Re \lesssim 80\,000$ the ratio of f_{turb} and f_{lam} can be expressed with the aid of Blasius correlation [Pope, 2000]

$$\frac{f_{\mathrm{lam}}}{f_{\mathrm{turb}}} = \frac{64/Re}{0.316/Re^{0.25}} \sim Re^{-0.75}, \tag{6.1}$$

which also shows that even at low Reynolds numbers relaminarizing a turbulent flow can produce a large drag reduction.

Furthermore, we measure Δp_L across the FMDs to compute their pressure drop coefficients K according to

$$K = \frac{2\Delta p_L}{\rho U^2}. \tag{6.2}$$

where ρ is the fluid density. For this purpose the pressure taps are separated by $12\,D$ in the streamwise direction and the FMD is placed $2\,D$ downstream the upper tap.

6.2.1   Flow management device

In order to control the flow in a way that the streamwise velocity profile becomes more flat a stationary FMD must redirect the flow such that the velocity is decelerated in the center of the pipe and accelerated close to the wall as compared to the uncontrolled velocity profile. We employ shaped honeycombs with variable length across the cross section of the pipe to generate a particular profile of the streamwise velocity.

Rapid prototyping by means of a 3D–printer (ProJet 3510 HD, 3D Systems, Inc.) is used to produce the FMDs as shown in Fig. 6.2. These FMDs consist of regular hexagonal honeycombs. The support (retaining ring) is used to keep the FMD between two pipe sections within a flange connector of the pipe. The cells of the honeycomb have a side length of $l = 0.45\,\mathrm{mm}$ and a wall thickness of $0.14\,\mathrm{mm}$ as shown in the detail of the figure on the left. The equivalent (hydraulic) diameter of a single cell is $d_h = 4A/P = 0.78\,\mathrm{mm}$, where A is the cross sectional area and P the perimeter of the cell. The porosity of the honeycomb, *i.e.* the ratio of open to blocked area, is $\beta = 71.8\%$.
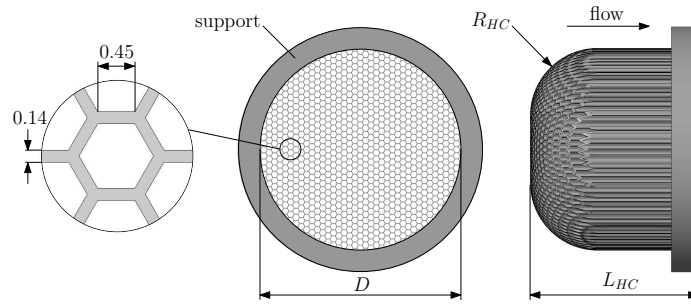
Figure 6.2: Front view and side view of the FMD. The support is mounted within a flange to fix the FMD within the pipe. All dimensions in mm.

The FMDs are printed with different total lengths (L_{HC}) and different overall shapes, *i.e.* with radially varying cell length. The cell length is varied in the radial direction by beveling the FMD with a varying radius R_{HC} from 0 to 14 mm in the maximum case. The flow direction through the shaped FMDs is as indicated in Fig. 6.2, *i.e.* the straight side facing downstream. Furthermore, several unshaped honeycombs (where $R_{HC} = 0$) with $L_{HC} = 1, 3, 5, 7, 10, 15$ and 20 mm, yielding relative lengths $L_{HC}/d_h = 1.3 - 25.6$, were investigated for comparison. For reference in the text each particular FMD is assigned a shortcut following the naming convention FMD-L_{HC}-R_{HC}.

The whole device including the support is printed in one piece as a precise, durable plastic part. The production drawing of the FMD and a .stl–file which can be used to print the FMDs with a 3D–printer is provided in the online supporting material. All tested FMDs are printed in UHD mode (resolution $750 \times 750 \times 890$ DPI, specified accuracy of 0.025–0.05 mm per 25.4 mm) using the material VisiJet Crystal. Fig. 6.3 (left) shows a magnified image of the front side of a printed honeycomb. The overall dimensional precision can be considered very high, although small deviances are visible especially in the corners of the cells. Pretests have shown that wall thicknesses < 0.14 mm, although desirable in the present context, could not be reproduced reliably. Due to the printing process the first layer of the print, *i.e.* where the printer starts to print the device, is slightly rougher and contaminated with wax which is used as support material in the printing process. This side, which was usually the flat side of the print and hence the backside of the FMD, needed to be sanded after printing. Fig. 6.3 (right) shows that even sanding with very fine
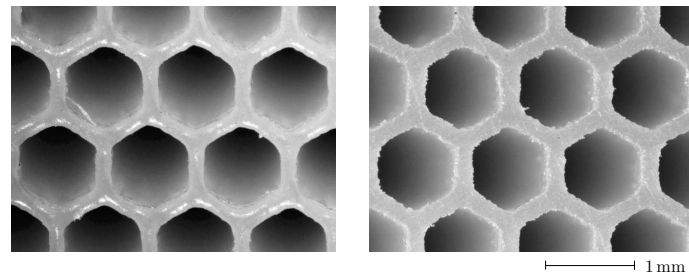
Figure 6.3: Magnified images of the frontside (left) and backside (right) of the printed honeycomb. The backside had to be sanded after printing. The length of the arrow indicates the scale.
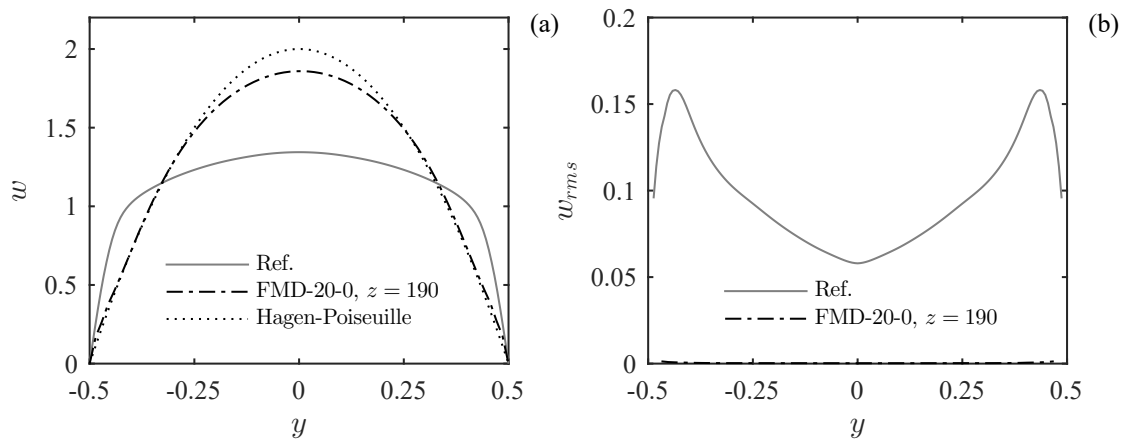
Figure 6.4: (a) Azimuthally averaged, mean streamwise velocity profile for relaminarized flow measured at $z = 190$ compared to the Hagen–Poiseuille laminar solution and the measured uncontrolled turbulent flow (Ref.). (b) Azimuthally averaged streamwise root–mean–square velocity for relaminarized flow measured at $z = 190$ compared to the measured uncontrolled turbulent flow (Ref.).

sand paper left tiny burrs at the front edges of the honeycomb.

To investigate the consequences of a modified streamwise velocity profile we characterize the effect of the FMDs by measuring the modification of the mean velocity distribution and the flow development downstream of the screen as well as the pressure drop across the FMDs. Determining the success of the modification is quite simple. If at $z = 190$ we observe a laminar pressure drop (f_{lam}) and a parabolic profile with significantly reduced turbulence intensity (as shown in Fig. 6.4), then the modification of the velocity profile is regarded effective. After identification of the optimal profile for maximum relaminarization, *i.e.* at the highest Reynolds number possible, we try to optimize the device so that the pressure drop is minimized.

In a number of references the importance of having tight tolerances has been pointed out [Roach, 1987]. Deviations in dimensional accuracy cause variations of the pressure drop coefficient from point to point and can produce large uncontrolled variations in the downstream velocity profile. From our measurements we can confirm that slight imperfections can have a profound influence on the downstream flow characteristics. Already a single cell being partially blocked by an air bubble or dirt can prevent relaminarization.

6.3   Results and discussion

In the current section we present the stereo PIV and pressure drop measurements and discuss the outcome. However, to get a quick overview all FMDs were first investigated by optical observation. To this end, neutrally buoyant anisotropic particles [Matisse and Gorman, 1984; Borrero-Echeverry *et al.*, 2018] were added as tracer particles for visualization and the flow in the pipe was illuminated employing LED string lights along the pipe. This allowed us to observe the development of the flow field up and downstream the flow management device (similar to Kühnen *et al.* [2015b; 2017]).

We varied the Reynolds number in increments of 100 and observed either laminar or turbulent flow downstream the FMDs. Fig. 6.5 (a) displays the maximum values for which laminar flow was found (*i.e.* we measured f_{lam}) for straight ($R_{HC} = 0\,\text{mm}$) honeycombs with lengths from $L_{HC} = 1$ to $20\,\text{mm}$. Already the shortest honeycomb with $L_{HC} = 1\,\text{mm}$ exhibits an unexpectedly high capability of relaminarizing the flow. Up to $Re = 6400$ the flow downstream this honeycomb is found to be laminar and stays laminar for the remainder of the pipe. By increasing the length of the FMD up to $10\,\text{mm}$ the flow can be made laminar even up to $Re = 8400$. A further increase in length does not seem beneficial anymore, as the maximum values for relaminarization decrease. In a next step we added a radial shape to the FMDs and tested the devices again in increments of 100. Fig. 6.5 (b) depicts the relaminarizing capability for two selected examples ($L_{HC} = 10\,\text{mm}$ and $L_{HC} = 20\,\text{mm}$) of radially shaped FMDs (as a function of R_{HC}). The radial shaping
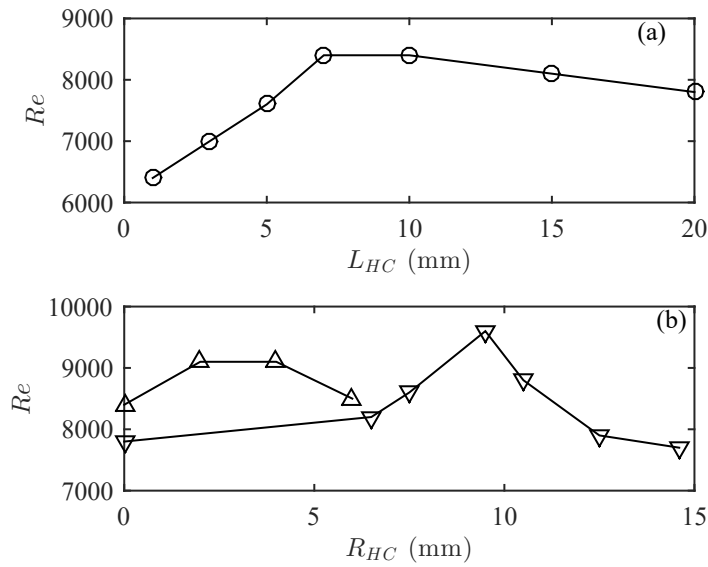
Figure 6.5: Maximum values of Re at which full relaminarization is observed for (a), straight FMDs ($R_{HC} = 0$ mm) as a function of L_{HC} and (b), two selected examples of radially shaped FMDs ($\triangle$, $L_{HC} = 10$ mm and $\triangledown$, $L_{HC} = 20$ mm) as a function of R_{HC}.

can improve the relaminarizing capability of the FMDs even further. The FMD with $L_{HC} = 10$ mm reaches $Re = 9100$ with $R_{HC} = 2 - 4$ mm, the FMD with $L_{HC} = 20$ mm even reaches $Re = 9600$ with $R_{HC} = 9.5$ mm. Again, a further increase in R_{HC} does not seem beneficial anymore, as the maximum values for relaminarization decreases with further increasing R_{HC}.

To characterize the flow downstream the FMDs we took PIV measurements at several locations along z, with $z = 3$ being the closest possible downstream location. Fig. 6.6 (a) and (b) exemplary show the appearance and evolution of the azimuthally averaged, mean streamwise velocity profile downstream a straight FMD ($L_{HC} = 20$ mm) and one with an additional radial shape ($R_{HC} = 9.5$ mm). In both of the two representative cases the FMDs similarly relaminarize the flow at the given Reynolds number, verified by the evolution of the profiles towards a parabolic shape, clearly manifest for the profiles at $z = 190$ (Hagen–Poiseuille solution drawn for comparison in dotted line). However, there is a particularly noteworthy difference in the time–averaged velocity profiles right downstream the FMDs, visible for the profiles at $z = 3$. While the profile for the straight FMD is
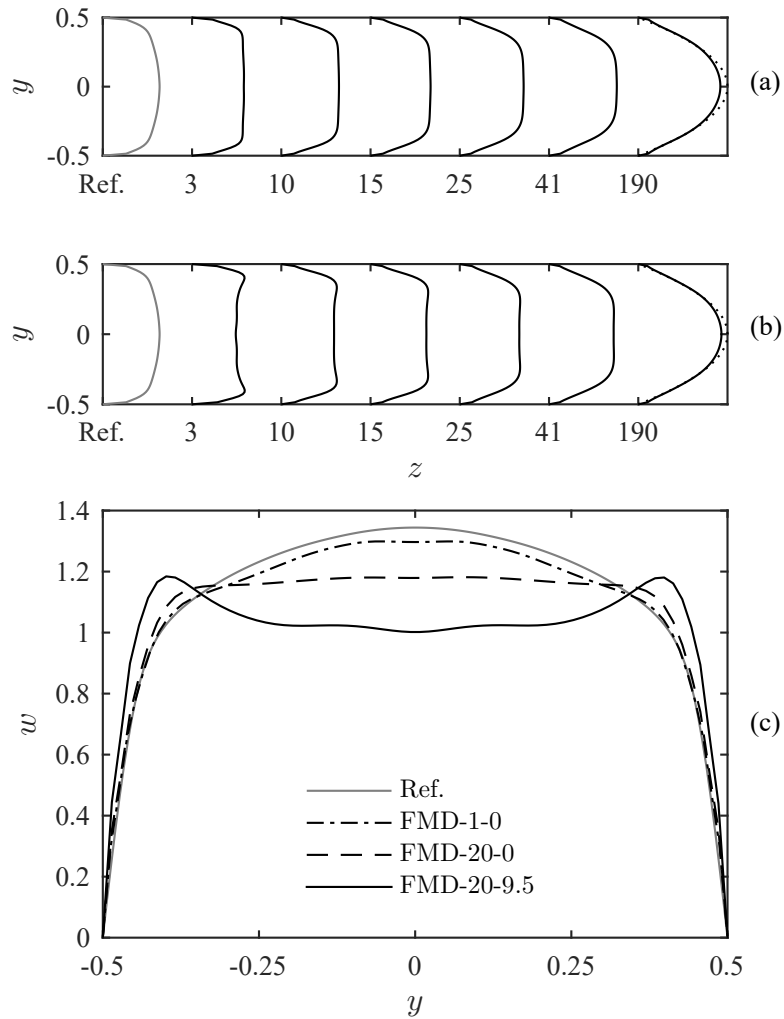
Figure 6.6: Azimuthally averaged, mean streamwise velocity profiles measured downstream the FMD at $Re = 6000$. (a) and (b), evolution of the velocity profile for FMD-20-0 and FMD-20-9.5, respectively. (c) Comparison of selected velocity profiles measured at $z = 3$. For reference and comparison the Hagen–Poiseuille laminar solution (dotted line in Fig. (a) and (b)) and the measured uncontrolled turbulent flow (Ref. in Fig. (a), (b) and (c)) are also shown.

clearly flattened as compared to the reference flow, the profiles for the shaped FMD exhibit an M–shaped appearance.

To enable a quantitative comparison of the flattening due to the straight FMD and the M–shape due to the shaped FMD Fig. 6.6 (c) depicts four different velocity profiles at $z = 3$. The reference profile is measured in uncontrolled turbulent flow. The velocity profile for FMD-1-0 ($L_{HC} = 1\,\mathrm{mm}$, $R_{HC} = 0\,\mathrm{mm}$) exhibits a slight, yet not very pronounced, flattening in comparison. For the much longer FMD-20-0 the velocity profile is almost perfectly flat in the central area of the cross section. The radially shaped FMD-20-9.5 produces an M–shaped appearance. The M–shaped appearance is caused by overshoots of faster fluid near the wall (peak at $y = \pm 0.4$) and a reduced velocity in the center (note the pronounced plateau where $w \approx 1$).

Interestingly, this M–shaped streamwise velocity profile is the one that provides the best relaminarizing capability we observed. According to Fig. 6.5 (b), FMD-20-9.5 can relaminarize a flow up to $Re = 9600$, which is 23% above the unshaped FMD-20-0 and 14% above the best working, unshaped FMD-10-0. Although those absolute values should be treated with caution and might vary for different FMDs (with differently sized honeycombs etc.) and different pipe diameters, the trend that the M–shape is advantageous compared to a mere flattening of the profile is consistent with observations of Scarselli *et al.* [2019] and Kühnen *et al.* [2018b]. Moreover, it is also qualitatively consistent with earlier observations of laminarization in buoyancy aided flows [Steiner, 1971; Jackson *et al.*, 1989] and in flows driven by body forces [He *et al.*, 2016a].

According to the findings reported in Kühnen *et al.* [2018c], a flattened streamwise velocity profile relaminarizes because it exhibits a severely decreased lift–up potential [Brandt, 2014] and thus can not sustain the turbulence regeneration cycle. As a measure for the reduced amplification mechanism of the regeneration cycle they consider the linearized Navier–Stokes equations and perform a transient growth (TG) analysis (following the algorithm given by Butler and Farrel [1993], for further details see also Kühnen *et al.* [2018c] and Meseguer and Trefethen [2003]). The velocity profiles of all successfully controlled, *i.e.* relaminarizing flows considered by Kühnen *et al.* [2018c; 2018b] and Scarselli *et al.* [2019] are shown to have a

134
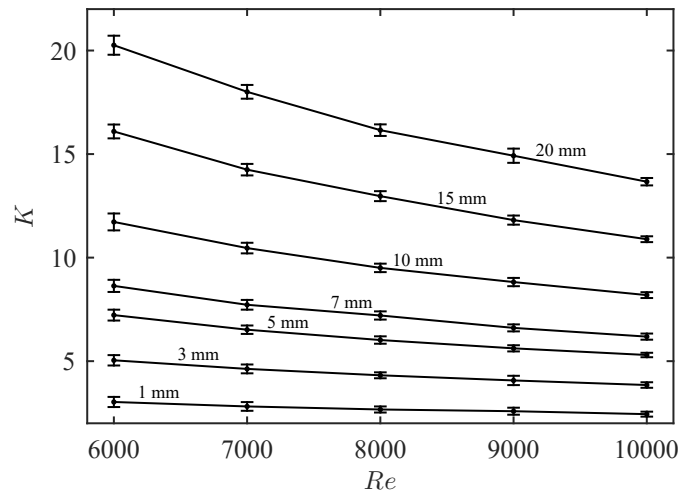
Figure 6.7: Pressure drop coefficient K as a function of Re for different straight FMDs ($R_{HC} = 0$ mm). Each curve is labelled by the corresponding value of L_{HC}. The error bars represent the 95% confidence interval.

substantially reduced TG. We applied the same procedure here to the exemplary velocity profiles shown in Fig. 6.6 (c). We find a value of 160 for the uncontrolled reference flow, 121 for FMD-1-0, 68.8 for FMD-20-0 and 39.4 for FMD-20-9.5. In other words, the profiles consistently show a considerably decreasing TG with increasing length of the FMDs and even more for the shaped FMDs. The mere flatting of the velocity profile due to FMD-20-0 is inferior to FMD-20-9.5, which produces an M–shaped streamwise velocity profile with the best relaminarizing capability and the lowest transient growth.

In a next step we measure the pressure drop Δp across the FMDs with length $1, 3, 5, 7, 10, 15$ and 20 mm and compute the pressure drop coefficient K according to Eq. (6.2). Fig. 6.7 shows K in the range $6000 \leq Re \leq 10\,000$. As to be expected, longer FMDs result in a larger normalized pressure drop and overall this decreases with the Reynolds number. Our results show a trend in good agreement with the data reported in Loehrke and Nagib [1976], although here the authors used honeycombs made of plastic straws at considerably higher Reynolds numbers.

Modifying the flow by means of a passive obstacle such as the FMDs comes with the additional cost of a concentrated pressure loss. Thus, the actual realization of a net energy saving for transporting the fluid can be achieved only when the gain
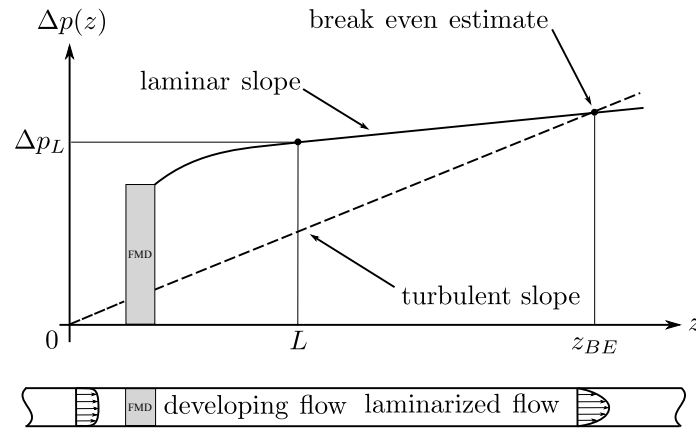
Figure 6.8: Sketch of the qualitative evolution of the pressure drop $\Delta p(z)$ along the pipe. In the undisturbed flow $\Delta p(z)$ increases linearly with z with a slope given by the turbulent friction factor (dashed line). The presence of relaminarizing honeycomb–FMD (grey rectangle) introduces an abrupt increase of $\Delta p(z)$. Further downstream the flow develops to laminar and $\Delta p(z)$ grows linearly with a slope proportional to the laminar friction factor (solid line). The intersection between the two curves defines the break–even point and represents the minimum length of pipe necessary to realize an energy gain.

due to the laminar pressure drop exceeds the concentrated loss. Fig. 6.8 shows the qualitative behavior of the pressure drop $\Delta p(z)$ with respect to the pressure tap located $2D$ upstream the honeycomb–FMD. The solid and dashed lines qualitatively represent the flow with and without the FMD, respectively. The presence of the obstacle results in an abrupt jump of the pressure. However, if relaminarization actually takes place, then at some point downstream the two lines intersect each other.

The distance of such an energetic break–even point from the FMD is a suitable measure for characterizing the performance of the FMDs. Generally, it depends on both the Reynolds number and on the concentrated pressure loss introduced by the FMD. To estimate the distance of the break–even point z_{BE} we look for the intersection between $\Delta p(z)$ without FMD (dashed line, Fig. 6.8) and $\Delta p(z)$ with the FMD (solid line). The distance is thus given by

$$z_{BE} = \frac{\Delta p_L - L f_{\text{lam}}}{f_{\text{turb}} - f_{\text{lam}}} \tag{6.3}$$

The results are presented in Fig. 6.9 together with the curve which describes the maximum Reynolds number for which an FMD outputs a stable laminar flow.
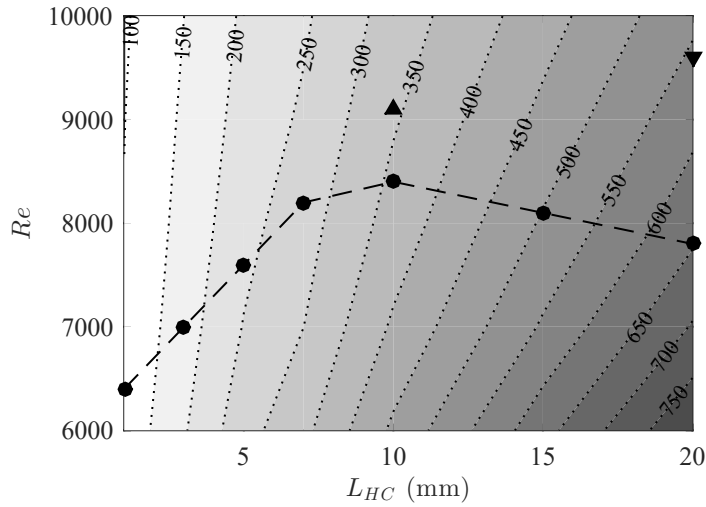
Figure 6.9: Contour levels of the break–even location z_{BE} computed for straight FMDs ($R_{HC} = 0$ mm). In addition, we marked the maximum value of Re at which relaminarization is observed for straight FMDs (●), FMD-10-2 (▲) and FMD-20-9.5 (▼).

Notice that the estimate of z_{BE} for $R_{HC} = 0$ mm is also a conservative estimate in case $R_{HC} \neq 0$ mm. As can be seen, FMD-1-0 can reach the energetic break–even point within almost $100\,D$ downstream. FMD-10-0 provides a considerably increased relaminarization capability, however, also z_{BE} is shifted downstream to $\approx 360\,D$. FMD-10-2, which relaminarizes the flow up to $Re = 9100$, needs slightly less than $350\,D$ to reach z_{BE}. In other words, only if the pipe is longer than $350\,D$ a net energy gain can be achieved. FMD-20-9.5, which relaminarizes the flow up to the highest Reynolds number of 9600, needs ≈ 550 pipe diameter to reach z_{BE}.

To put these results in perspective, we estimate the pipe length to reach an energetic break–even with another drag reduction technique. To this end, we assume riblets providing a drag reduction of 10% and hence we replace f_{turb} in equation (6.3) with $0.9 f_{turb}$. As a result, for FMD-20-9.5 at $Re = 9600$ we estimate a pipe length of $\approx 630\,D$ to equate the effect of such riblets over the same distance, as for this pipe length both the FMD and the supposed riblets offer a drag reduction of 10%. The main difference is, that the riblets would offer 10% drag reduction right from the beginning of the pipe, while for the FMD this length is required to reach 10%, and the FMD will outperform such riblets significantly for every pipe longer than $\approx 630\,D$.

6.4 Conclusions

By employing 3D–printed honeycombs to control the flow, we can not clearly distinguish between several parameters acting on the flow, as the suppression of transverse components and fluctuations in the flow through the honeycombs can annihilate turbulence without any further measures up to Reynolds numbers considerably higher than the critical Reynolds number of ≈ 2040 [Avila *et al.*, 2011] for sustained turbulence. However, our investigation has shown that custom–shaped honeycombs with variable length across the cross section can be used to produce optimized streamwise velocity profiles for maximal relaminarization in a pipe. The maximally achievable Reynolds number for complete relaminarization we found is of the order of 10 000. Although this is still a relatively low Reynolds number in terms of industrial applications, the achievable drag reduction is already of a factor of five according to Eq. (6.1). Our lower bound estimate for the distance, where a net energy gain can be achieved, is $100\,D$ for the shortest FMD-1-0 and ≈ 550 for the FMD-20-9.5 exhibiting the highest relaminarizing capability. The ideal streamwise velocity profile for relaminarization is shown to be not just a flattened profile, but to exhibit a specific M–shape, *i.e.* with velocity overshoots close to the wall and a plateau in the center of the pipe.

Several further geometries, in particular a radial variation of the cell size, could be very interesting targets for future investigations and improvements in terms of pressure drop and maximal relaminarization. After all, pipe flow exhibits a feature that makes it particularly attractive for relaminarization methods: the laminar state is stable to infinitesimal perturbations at all flow speeds [Drazin and Reid, 2004]. Consequently, once relaminarization is achieved, the flow remains laminar as long as the pipe is straight and smooth. Turbulence can only return if a sufficiently strong disturbance is encountered. However, in practice such a "sufficient" disturbance can be quite small [Hof *et al.*, 2003], especially at higher Reynolds numbers.

---

7   Heart pulse inspired drag reduction

Flow rates in the aorta periodically surpass the transition threshold to turbulence, yet no turbulence arises and flows remain predominantly laminar. Intense turbulent flow conditions would indeed be unfavourable and potentially damage the highly shear responsive inner layer of blood vessels, the endothelium. We here show that the pulsation cycle of the heart delays transition and minimizes the amount of turbulence encountered in a given flow. Applying the same principle to fully turbulent pipe flows at much higher Reynolds numbers, we find that pulsatile driving decreases the drag by more than 25%. This operation mode is considerably more efficient when compared to steady driving which is the status quo for virtually all fluid transport processes ranging from heating circuits to water, gas and oil pipelines.

7.1   Letter

Turbulent flows occur in several applications and are associated with large shear stresses and friction with respect to laminar conditions. Available estimates show that around 20% of the global electric power is consumed by pumping systems to overcome the drag caused by friction [Frenning, 2001]. Turbulence is also believed to appear in cardiovascular flows and it is cause of concern as intense flow fluctuations and varying shear stresses have been attributed to endothelium cell dysfunctions and arteriosclerosis [Davies *et al.*, 1986; DePaola *et al.*, 1992; Davies, 2009; Gimbrone and García–Cardeña, 2016]. Finding the key to reducing the effects of turbulence would have profound implications on the environment and heath care. Yet a viable and scalable solution to tame turbulence is still missing despite decades of extensive research.

A number of active drag reduction methods which promise significant energy savings have been proposed [Karniadakis and Choi, 2003; Quadrio *et al.*, 2009; Nakanishi *et al.*, 2012], however their practical implementation is hindered by very complicated actuators [Auteri *et al.*, 2010] or technological limitations [Kasagi *et al.*, 2009b]. On the other hand, passive techniques such as the addition of polymer additives [Virk *et al.*, 1970; Choueiri *et al.*, 2018] and the use of bio–inspired wall textures [Garcia-Mayoral and Jiménez, 2011] suffer from high costs and degradation and are limited to very specific applications. More recently, a series of experiments showed that it is possible to relaminarize a turbulent flow by interfering with the turbulence regeneration cycle [Kühnen *et al.*, 2018c]. While this method results in large energy savings, it is limited in practice by the need of smooth and straight pipelines to avoid transition back to turbulence.

Here we present a new approach to pumping a turbulent flow inspired by the stabilizing effect of the pulsatile flow in the human aorta. By mimicking the heart pulse but at higher Reynolds numbers, we show how a suitable modulation of the flow rate can induce a severe departure of turbulence from statistical equilibrium which results in lower friction and energy savings.

Unsteady turbulent flows have been extensively investigated over the last two

decades with experiments and numerical simulations [He and Jackson, 2000; Greenblatt and Moss, 2004; He *et al.*, 2011; He and Seddighi, 2013; He *et al.*, 2016a; Mathur *et al.*, 2018]. In these studies an initially steady turbulent flow undergoes a rapid change in fluid speed and the statistical properties of the evolving flow are investigated. Rapid flow acceleration typically delays turbulence kinetic energy production and decreases the wall shear stress with respect to the quasi–steady value. Contrarily, flow deceleration enhances friction, while at higher deceleration rates there is evidence of friction reduction [Ariyaratne *et al.*, 2010]. Despite the friction reduction observed during an increase of Reynolds number, to the best of our knowledge there are no examples of control strategies based on the frictional properties of an unsteady turbulent flow.

The idea of a pulsating turbulent flow to reduce friction comes from the naturally occurring heart–driven blood flow through the cardiovascular system. Natural transition from laminar to turbulence occurs, in steady pipe flows, at Reynolds number $Re \approx 2000$ [Avila *et al.*, 2011] (here $Re = U_m D / \nu$, where U_m is the mean velocity, D is the duct diameter and ν the medium kinematic viscosity). Remarkably, in the aorta flow velocities can reach values well into the turbulent regime (peak Reynolds number $Re \approx 4000$ [Bürk *et al.*, 2012]). Consequently, the endothelium experiences varying shear stress in this fluctuating flow environment, which may have an adverse effect on the cell layer. Thus it is natural to ask whether the cardiovascular cycle has evolved to reduce the effects of turbulence.

In a first series of experiments we investigate a pulsatile flow similar to the one observed in the descending part of a human aorta. Here, a servo–driven syringe pump is used to pump water through a 1.2 m long pipe (inner diameter $D = 10$ mm) into a reservoir at a flow rate modeled after available experimental data [Bürk *et al.*, 2012], see Fig. 7.1 (a). For further details of the experimental setup we refer the reader to the supplemenatry information, section 7.2.2. A shorter pulse period (0.7s) and smaller pipe diameter have been chosen to compensate for the different viscosity of blood and the larger aorta diameter (≈ 20 mm). Visualization particles are added to the flow to monitor a region $30D$ long which is located $60D$ downstream the pipe inlet. Under these conditions, the heavy perturbations introduced by the pipe
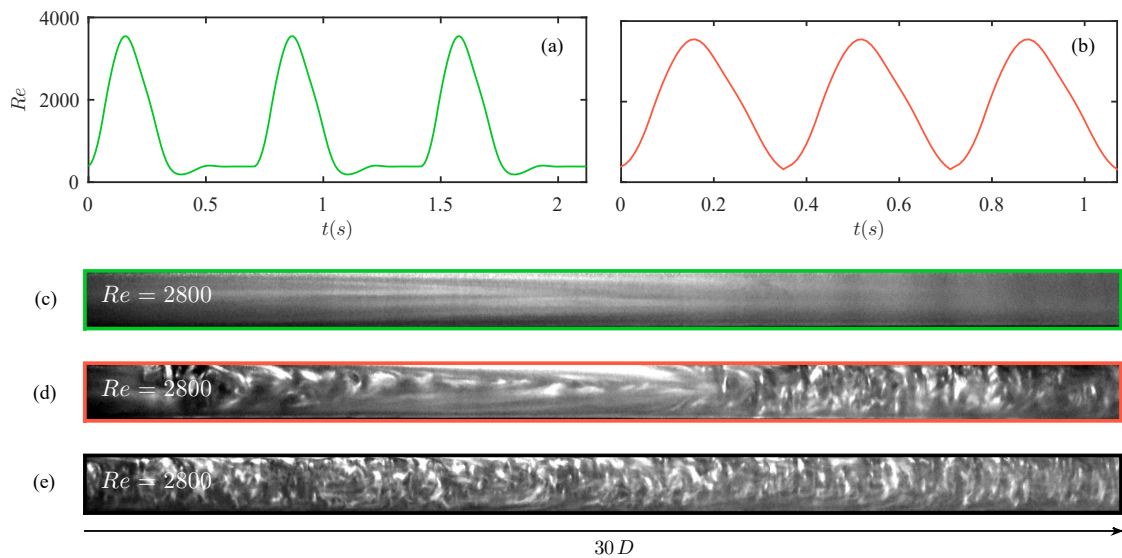
Figure 7.1: Decay of turbulence in aortic flow. Temporal variation of the Reynolds number in case of normal cardiac pulse (a) and for a modified signal lacking the diastolic phase (b). (c) and (d), flow structures at $Re = 2800$ in a region $30D$ long located $60D$ downstream of the pipe inlet for the case (a) and (b), respectively. (e) fully developed turbulent flow at $Re = 2800$ for comparison.

entrance decay further downstream and the flow appears consistently laminar across several cycles (a flow snapshot at $Re = 2800$ is shown in Fig. 7.1 (c)), even though the flow rate exceeds the transition Reynolds number (*i.e. Re* > 2040, [Avila *et al.*, 2011]). On the contrary, when the pulse lacks the diastolic phase (nearly time–independent phase of the cycle) and consists only in acceleration and deceleration ramps (Fig. 7.1 (b)), localized turbulence patches can be seen actively spreading from the inlet and entraining laminar flow all over the pipe (a flow snapshot at $Re = 2800$ is shown in Fig. 7.1 (d)). For comparison Fig. 7.1 (e) shows developed turbulence at the same Reynolds number ($Re = 2800$) under steady conditions.

From the simple experiment of Fig. 7.1 we learn that Re alone, usually governing the stability properties of the flow, is not adequate to predict the evolution of perturbations under unsteady conditions. Perturbations might decay or evolve into turbulence at a given Re depending also on the previous flow history. In this view, the diastole effectively decouples the acceleration from the deceleration, allowing turbulence to decay before Re increases again.

Next, we apply a pulsatile operation mode on a fully turbulent flow and inves-

tigate the frictional properties. To this end, we pump water through a 7 m long pipe (inner diameter $D = 30$ mm) into a reservoir by means of the same syringe setup described above. The pressure drop Δp is measured across a length $L = 120\,D$ after a development length of $60\,D$ from the pipe inlet. Subsequently, the wall shear stress τ_w is reconstructed by using the force balance in the streamwise direction

$$\rho \frac{dU_m}{dt} = -\frac{\Delta p}{L} - \frac{4\tau_w}{D}, \tag{7.1}$$

where ρ is the water density and U_m is the time varying mean flow velocity. In addition, we run direct numerical simulations (DNS) of the Navier–Stokes equations with an imposed time–varying Reynolds number matching with the experiments. The DNS code employed is the highly scalable parallel solver *NSPipeFlow* and assumes a $5\,D$ long periodic pipe domain (see Supplemenatry Information, section 7.2.1 for further details).

We begin our study by testing a cycle consisting of a series of linear flow rate ramps smoothly joined together, corresponding to *Re* oscillating between 3200 and 18 800 with a period $T = 4.5$ s, see Fig. 7.2 (a). The parameters have been chosen to ensure accuracy of the measured signals and a precise flow rate control. Fig. 7.2 (d) shows the computed friction coefficient (here defined as $C_{f,0} = 2\tau_w/(\rho U_0^2)$, where U_0 is minimum velocity during the cycle and τ_w is estimated with Eq. (7.1)) from experiments and DNS. For comparison, the friction coefficient associated with a quasi–steady turbulent flow (defined using the Blasius scaling as $C_{f,0} = 0.079 Re^{-0.25} U_m^2/U_0^2$) is represent in black–dotted line. With respect to the quasi–steady value, an increase of $C_{f,0}$ (on average $\approx 60\%$) at the beginning of the acceleration phase is punctuated by a subsequent reduction that ends when *Re* reaches its maximum value. During the deceleration phase $C_{f,0}$ follows closely the quasi–steady value and terminates at a higher value that provides the initial condition for the next cycle. The results obtained from DNS are in good agreement with the experimental observations.

We proceed quantifying the extent of frictional (drag) reduction as

$$R = \frac{C_f^* - \overline{C_{f,0}}}{C_f^*}, \tag{7.2}$$
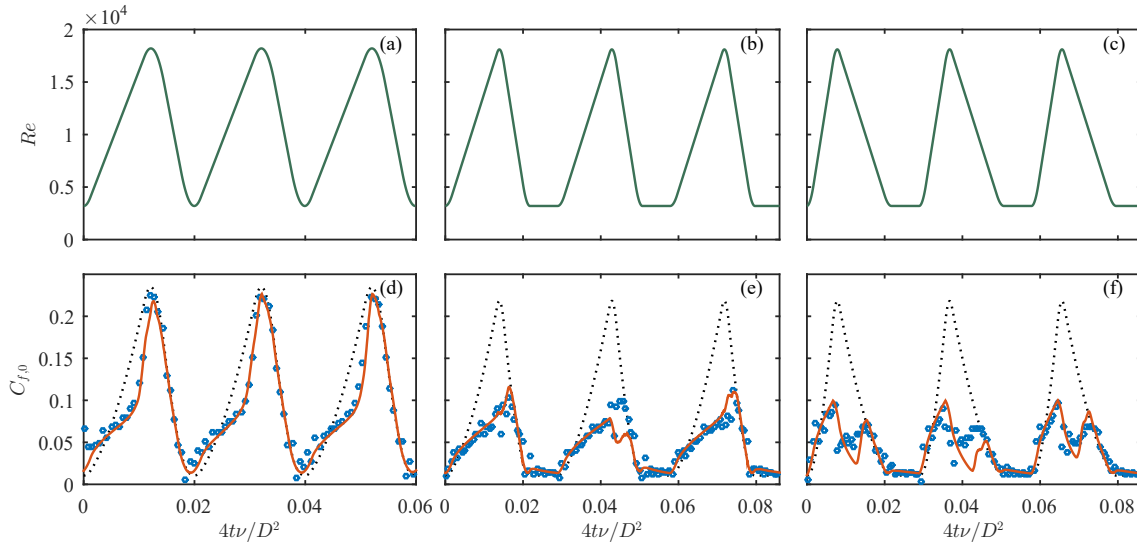
Figure 7.2: Friction reduction in pulsating flow. Effect of three different cycles on the friction coefficient $C_{f,0}$. (a), (b) and (c), Reynolds number modulation imposed in experiments and DNS. (d), (e) and (f), corresponding friction coefficient $C_{f,0}$ for experiments (blue circles) and DNS (red line). For comparison, the friction associated with the quasi–steady flow is shown in the black dotted line.

where the overline denotes an average over several cycles and C_f^* is the friction coefficient of the reference flow (steady, uncontrolled flow at $\overline{Re}$). The cycle shown in Fig. 7.2 (a) yields surprisingly a drag increase ($R = -3.1\%$), notwithstanding friction levels lower than the corresponding quasi–steady values. This seemingly contradictory fact can be understood by observing that the quasi–steady flow itself (the black–dotted line of Fig. 7.2 (d)) is associated with a much higher drag increase ($R = -14\%$).

Inspired by the diastolic phase found in the aortic flow and its role in limiting turbulence growth, we design a new cycle where a region of constant Re (rest phase) is inserted before the acceleration with the purpose to decouple it from the preceding deceleration (Fig. 7.2 (b)). Remarkably, the flow now responds with considerably lower values of $C_{f,0}$ during the acceleration (the maximum $C_{f,0}$ is reduced by half) and part of the deceleration, resulting in a drag reduction rate $R = 22\%$ (Fig. 7.2 (e)). Key to the effectiveness of the rest phase is the relaxation of $C_{f,0}$ to a lower value and hence a favorable initial condition for the acceleration.

From an energetic point of view, in unsteady flows a reduction of the mean

friction $C_{f,0}$ is not sufficient to ensure that the power dissipation per unit length ($P = Q\Delta p/L$, where Q is the volume flow rate) is lower with respect to steady conditions . To quantify this aspect we introduce the power savings

$$S = \frac{P^* - \overline{P}}{P^*}, \tag{7.3}$$

where P^* is the power dissipated by the reference flow. Computing the power savings for the cycle of Fig. 7.2 (b) yields a loss ($S = -5.3\%$), notwithstanding the large drag reduction. The poor performance of this operation mode can be rationalized by observing that the beneficial effect of flow acceleration is energetically expensive, since an increase of flow rate requires the pressure gradient and hence the power to grow (cf. Eq. (7.1)).

In order to find a compromise between the power required during the acceleration and its beneficial effect, we test the cycle of Fig. 7.2 (c), where the acceleration phase is now shorter than the deceleration phase and the rest phase left unvaried. The more rapid increase of Re induces a sudden drop of friction at the beginning of the deceleration (Fig. 7.2 (f)). Here, friction reaches levels comparable to the ones assumed during the rest phase, albeit at very high Re. This effect is highly beneficial to drag reduction ($R = 27\%$) and even allows for power savings ($S = 8.1\%$).

Finally, we investigate how changing the acceleration and rest phase affects drag reduction and power savings. To this end, we carry out a total of 540 experiments spanning different rest phase and acceleration durations (denoted respectively by T_r and T_a), while keeping constant the minimum and maximum Re and T (cf. Fig. 7.5 in the Supplementary Information). The resulting map of S is shown in Fig. 7.3 (a). The white, dashed line separates the regions of positive and negative S and the cycles of Fig. 7.2 (a), (b) and (c) are denoted respectively with a circle, star and square. Interestingly, shorter acceleration times consistently lead to higher power savings, hence suggesting the importance of a brief, intense acceleration followed up by a longer, gentle deceleration. The rest phase is necessary for obtaining power savings, however, an exceedingly long one has the opposite effect. The optimal value of T_r depends weakly on T_a and it is approximately equal to half the period $T = 0.024\nu/D^2$. The same parameter space can be mapped to the usual $C_{f,0}$–Re
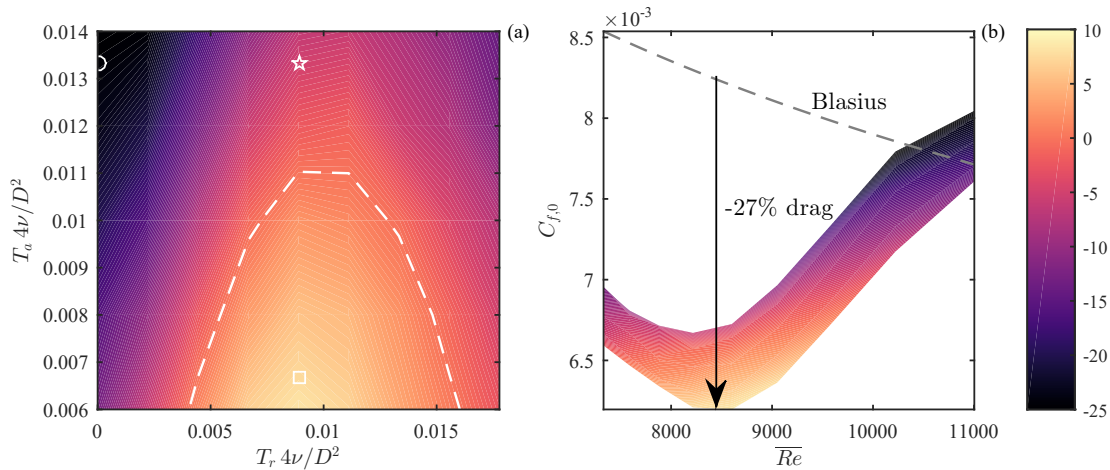
Figure 7.3: Optimization of power savings. (a) Percentage of the power savings S as a function of the duration of the acceleration T_a and rest phase T_r. The white, dashed line separates the region of positive and negative S. The circle, star and square represent the parameters for the cycles of Fig. 7.2 (a), (b) and (c), respectively. (b) corresponding values of S represented in the $C_{f,0}$–Re plane. The gray dashed line is the friction level of a steady turbulent flow (Blasius correlation).

plane (Fig. 7.3 (b)) to highlight the effect of the cycles on the drag reduction R and the dependence from $\overline{Re}$. For comparison, we plot the Blasius relation for turbulent friction. The largest reduction in $C_{f,0}$ (-27%) is found for $\overline{Re} \approx 8600$ and it is close to the region of maximum S. Higher $C_{f,0}$ are found for lower and higher values of $\overline{Re}$.

Inspired by the turbulence reducing capability of the flow in the human aorta, we investigated the frictional properties of a large set of turbulent pulsatile flow conditions in which we varied accelerations and the duration of the rest phase. For the first time, we showed numerically and experimentally the existence of cycles characterized by lower drag and energy dissipation with respect to steady conditions. Surprisingly, a rest phase analogous to the heart diastole is necessary to enhance the effect of the flow acceleration and reduce friction during the remainder of the cycle. Our findings show a novel way to reduce turbulent friction with a great potential for further exploration and optimization, with numerous implications in medical science and industry.

7.2 Supplementary Information

7.2.1 Direct numerical simulations

We solve the incompressible Navier–Stokes equations in cylindrical coordinates in a pipe of length $5D$ with periodic boundary conditions at the extremities. The equations are written in non–dimensional viscous units by using the density ρ, kinematic viscosity ν and pipe diameter D and take the following form

$$\partial_t \boldsymbol{u} + (\boldsymbol{u} \cdot \boldsymbol{\nabla} \boldsymbol{u}) = -\nabla p + \nabla^2 \boldsymbol{u}, \tag{7.4}$$

$$\boldsymbol{\nabla} \cdot \boldsymbol{u} = \boldsymbol{0}, \tag{7.5}$$

To impose a time–varying Reynolds number the mean velocity is updated at every time step, namely

$$U_{m,\text{new}} = U_{m,\text{old}} + \alpha(t)\delta t, \tag{7.6}$$

where δt is the time step and $\alpha(t)$ is a prescribed acceleration rate. An axial forcing term is then added to the mode zero of Eq. (7.4) to enforce that the integral of the velocity profile yields the mean flow, *i.e.*

$$U_m = \int_0^1 2u(r)r\,dr. \tag{7.7}$$

Simulations were carried out by using the custom, high–scalable, pseudo–spectral solver *NSPipeFlow*. The codes employs Fourier–Galerkin expansions along the axial and azimuthal directions, and eighth–order, finite central differences for the radial dimension collocated on a Gauss–Lobatto–Chebyshev grid. The equations evolve in time with a second–order, predictor–corrector algorithm and a time step dynamically adjusted to satisfy the Courant–Friedrich–Lewy condition. For further details about the code implementation we refer the reader to Shi *et al.* [2015] and Lopez *et al.* [2019]. As the Reynolds number changes over time by more than an order of magnitude, the code can adaptively change the grid spacing to match the required spatial resolution needs. Typical values found at the minimum and maximum Reynolds numbers are given in Table 7.1.

Re	$\min \Delta_r^+$	$\max \Delta_r^+$	$\Delta_{(R\theta)}^+$	Δ_z^+	δ_t
3 200	0.053	2.44	7.06	5.62	$4.80 \cdot 10^{-3}$
18 800	0.016	2.70	7.23	7.20	$1.91 \cdot 10^{-3}$

Table 7.1: From left to right: Reynolds number Re based on the mean velocity, minimum and maximum radial resolution (in inner units), azimuthal resolution (in inner units), axial resolution (in inner units) and average time step size δ_t.

7.2.2 Experimental set–up

We employ a large scale, customized syringe pump (sketched in Fig. 7.4) to control precisely the flow rate and hence impose an arbitrary modulation of the Reynolds number. The test section consists in a 7 m long, precision bore glass pipe (Duran, KPG, internal diameter $D = 30 \pm 0.01$ mm) made by joining 1 m long segments with custom PMMA flanges (in the experiments of Fig. 7.1 the test section consists of a single pipe segment with $D = 10 \pm 0.01$ mm and length 1.2 m). Water flows through the pipe into a reservoir as the syringe pump is displaced by a linear actuator driven by a servomotor (Festo, ESBF-BS-80-1500-15P and Festo, EMMS-AS-70-M-LS-RS, not shown in Fig. 7.4). A pc is used to control the motor and thus the plunger speed within an accuracy of ±0.01 mm/s. The syringe has an internal diameter of $D_p = 125 \pm 0.11$ mm and total length $L_p = 1500 \pm 0.1$ mm, corresponding to a maximum run time of ≈ 870 advective time units (D/U) for the chosen pipe diameter. Turbulence development is ensured by perturbing the flow at the pipe inlet with a pin and letting the flow develop for $60\,D$. Differential pressure is measured over the subsequent $120\,D$ with a carefully calibrated pressure transducer, full scale 2.5 kPa. The wall taps (diameter $d = 0.5$ mm) are drilled through the PMMA flanges and have been polished to remove any burr. Water temperature is monitored at the outlet of the pipe with a Pt–100 probe (indicated as T in Fig. 7.4) and typically is held constant within ±0.05 °C. In a typical measurement run the desired flow rate wave form is repeated cyclically while traversing the available stroke length. Temperature is measured in real–time in order to compute the correct motor speed and hence imposing the correct Reynolds number. The control and acquisition frequency are
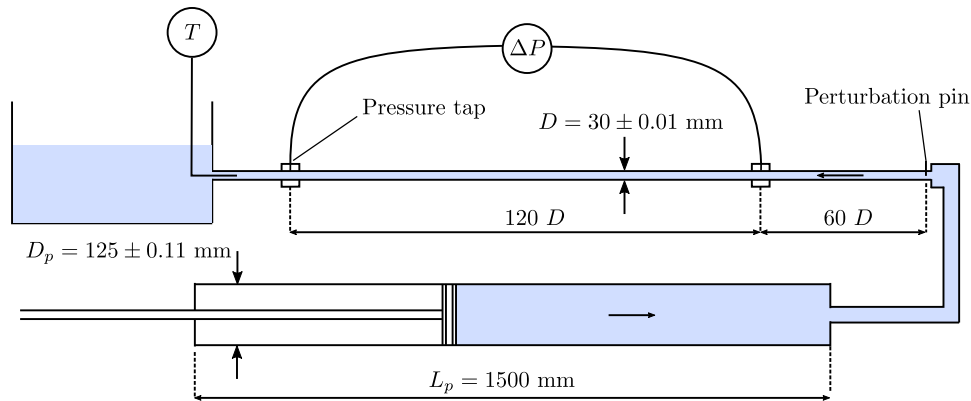
Figure 7.4: Sketch of the experimental setup. Drawing not to scale.

set to 50 Hz. Depending on the period duration there are from a minimum of 10 to a maximum of 15 cycles per run. To ensure a proper statistical representation of the unsteady friction each run is then repeated several times (> 150) and the results averaged. The first cycle is found to be systematically different from the others it has been excluded from the averaging process. Overall, the drag reduction R and the power savings S are estimated with an accuracy of $\pm 1.2\%$.

7.2.3 Cycle parameters

We consider cycles consisting of linear ramps of Re and periods of constant flow rate. Throughout the experiments the minimum and maximum Re are held constant and equal to 3200 and 18 800, respectively. The combined duration of acceleration and deceleration T is always fixed to 4.5 s, while the duration of the acceleration and rest phase are respectively varied in the intervals $T_a \in [1.35, 3.15]$ s and $T_r \in [0, 4]$ s. To avoid abrupt change in the piston acceleration the cuspids have been locally smoothed with a moving average filter of width 0.8 s (cf. Fig. 7.2 (a), (b) and (c)).
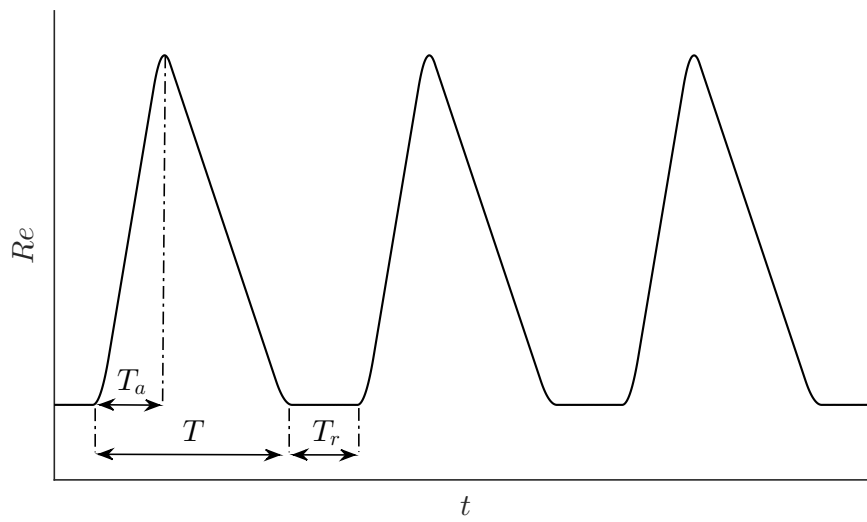
Figure 7.5: Definition of the flow rate cycle.

8 Conclusions

We started this work with an historical perspective on the nature of friction in turbulent flows in cylindrical pipes and investigated how turbulence affects friction when Re becomes large. Over the last century, scientists have tried to decode the expression of a universal law capable of predicting friction for the turbulent regime. Very little progress has been made since von Kármán and Prandtl proposed a scaling capable of predicting the deviation observed from the power law first introduced by Blasius, with the exception of Barenblatt's alternative friction law which however was not met with widespread consensus. Differently from previous studies, the research presented in Chapter 2 focused instead on the moderate Re turbulent regime and showed that friction appears to be better described by the Blasius scaling instead of the Prandtl–von Kármán formula (up to $Re < 70\,000$). In addition, the scaling exponent was rationalized with a simple argument based on dimensional analysis. Furthermore, the results showed evidence suggesting that large scale motions are implicated in the deviation of friction from the simple power law scaling, and that their contribution becomes dominating as Re increases. In the light of these results, what was considered as a mere empirical correlation can now be regarded as a well defined turbulence regime where the near–wall structures generated by the turbulence regeneration cycle are predominant and large scale motions do not contribute to friction significantly. Although Chapter 2 showed a strong connection between large scale motions and the deviation of friction from the Blasius scaling, the underlying physical mechanism responsible for such a deviation needs further investigation. Future work should address precisely how features of large scale motions, such as steak meandering and the separation between inner and outer layer dynamics can affect friction. In addition, a better understanding of

the role of large scale motions on friction might also contribute to studies aiming at reducing drag at high Re.

In Chapters 3 to 6 different relaminarization methods were presented and the underlying mechanisms were discussed. Flows in pipes are practically turbulent for $Re > 2800$ and spontaneous relaminarization is never observed despite the stability of the laminar solution with respect to infinitesimal perturbations. However, thanks to numerical simulations and several experimental devices, a new general strategy to initiate relaminarization was shown to be effective in experiments up to $Re = 40\,000$. Key to the success of the method is a flatter velocity profile that disrupts the turbulence regeneration cycle by reducing the lift–up effect. The work presented here focused mostly on the physics behind the process and the implications in terms of friction reduction and several open questions are still unanswered. While the picture of turbulence transition is becoming gradually clearer, very little is known about relaminarization. Future work could address the identification of close visits to known invariant solution of the Navier–Stokes equations and the role of the edge state (a special chaotic solution that neither evolves to turbulence nor to the laminar state) during turbulence collapse. In addition, while it has been observed that similar flattened velocity profiles are equivalently successful at suppressing lift–up, it is not yet clear whether the flow actually relaminarize in the same way across different experiments. The possibility of reducing friction dramatically is also appealing for technical applications involving long straight sections of pipelines. Future research could focus on designing more efficient devices capable of relaminarizing the flow at even higher Re or optimizing the existing strategies to minimize the energy input or the pressure losses introduced by flow obstacles.

Finally, Chapter 7 considered a turbulent flow under pulsating conditions and its frictional properties. The study showed experimentally that at values of Re well beyond transition, localized turbulence can not be sustained in a pulsatile flow with a wave form analogous to the one found in the human aorta. The technique is then extended to a fully turbulent flow and the effect of different flow rate modulations were tested. It was found that on average friction decreases considerably and energy savings are possible when a rest phase similar to the heart diastole is inserted right

after a reduction of Re. The findings constitute novel evidence of a flow regime that consumes on average less energy with respect to a steady turbulent flow at the mean Re of the cycle. The question whether the solution is optimal is however not addressed and opens several research possibilities. Future work should investigate the effects of different wave forms and further explore the parameter space. Medical research might also benefit from additional studies on unsteady turbulent flows. As the inner layer of blood vessels, the endothelium, can be damaged by exposure to a high turbulent shear stress, a better understanding of the cause of unsteady turbulence could improve the design of devices for artificial blood circulation or surgical implants in blood vessels.

Bibliography

[Ahmed and Lee, 1997] F. Ahmed and B. E. Lee, "The Production of Shear Flow Profiles in a Wind Tunnel by a Shaped Honeycomb Technique," *J. Fluids Eng.*, 119(3):713–715, 1997.

[Ariyaratne *et al.*, 2010] C. Ariyaratne, S. He, and A. E. Vardy, "Wall Friction and Turbulence Dynamics in Decelerating Pipe Flows," *J. Hydraul. Res.*, 48(6):810–821, 2010.

[Auteri *et al.*, 2010] F. Auteri, A. Baron, M. Belan, G. Campanardi, and M. Quadrio, "Experimental Assessment of Drag Reduction by Traveling Waves in a Turbulent Pipe Flow," *Phys. Fluids*, 22(11):115103, 2010.

[Avila *et al.*, 2011] K. Avila, D. Moxey, A. de Lozar, M. Avila, D. Barkley, and B. Hof, "The Onset of Turbulence in Pipe Flow," *Science*, 333(6039):192–196, 2011.

[Avila and Hof, 2013] M. Avila and B. Hof, "Nature of Laminar–Turbulence Intermittency in Shear Flows," *Phys. Rev. E*, 87(6):063012, 2013.

[Avila *et al.*, 2010] M. Avila, A. P. Willis, and B. Hof, "On the Transient Nature of Localized Pipe Flow Turbulence," *J. Fluid Mech.*, 646:127–136, 2010.

[Barbin and Jones, 1963] A. R. Barbin and J. B. Jones, "Turbulent Flow in the Inlet Region of a Smooth Pipe," *J. Basic Eng.*, 85(1):29–33, 1963.

[Barenblatt, 1993] G. I. Barenblatt, "Scaling Laws for Fully Developed Turbulent Shear Flows. Part 1. Basic Hypotheses and Analysis," *J. Fluid Mech.*, 248:513–520, 1993.

[Barenblatt and Prostokishin, 1993] G. I. Barenblatt and V. M. Prostokishin, "Scaling Laws for Fully Developed Turbulent Shear Flows. Part 2. Processing of Experimental Data," *J. Fluid Mech.*, 248:521–529, 1993.

[Barkley *et al.*, 2015] D. Barkley, B. Song, V. Mukund, G. Lemoult, M. Avila, and B. Hof, "The Rise of Fully Turbulent Flow," *Nature*, 526(7574):550–553, 2015.

[Bechert *et al.*, 2000] D. W. Bechert, M. Bruse, and W. Hage, "Experiments with Three–Dimensional Riblets as an Idealized Model of Shark Skin," *Experiments in Fluids*, 28(5):403–412, 2000.

[Bewley, 2009] T. R. Bewley, "A Fundamental Limit on the Balance of Power in a Transpiration–Controlled Channel Flow," *J. Fluid Mech.*, 632:443–446, 2009.

[Bewley *et al.*, 2001] T. R. Bewley, P. Moin, and R. Temam, "DNS–Based Predictive Control of Turbulence: An Optimal Benchmark for Feedback Algorithms," *J. Fluid Mech.*, 447:179–225, 2001.

[Blackwelder and Kovasznay, 1972] R. F. Blackwelder and L. S. G. Kovasznay, "Large–Scale Motion of a Turbulent Boundary Layer during Relaminarization," *J. Fluid Mech.*, 53(01):61–83, 1972.

[Blasius, 1913] H. Blasius, "Das Ähnlichkeitsgesetz Bei Reibungsvorgängen in Flüssigkeiten," *Mitteilungen Über Forschungsarbeiten Auf Dem Geb. Ingenieurwesens*, 131, 1913.

[Bodenschatz and Eckert, 2011] E. Bodenschatz and M. Eckert, "Prandtl and the Göttingen School," In P. A. Davidson, Y. Kaneda, K. Moffatt, and K. R. Sreenivasan, editors, *A Voyage Through Turbulence*, pages 40–100. Cambridge University Press, Cambridge, 2011.

[Borrero-Echeverry *et al.*, 2018] D. Borrero-Echeverry, C. J. Crowley, and T. P. Riddick, "Rheoscopic Fluids in a Post-Kalliroscope World," *Phys. Fluids*, 30(8):087103, 2018.

[Bourassa and Thomas, 2009] C. Bourassa and F. O. Thomas, "An Experimental Investigation of a Highly Accelerated Turbulent Boundary Layer," *J. Fluid Mech.*, 634:359–404, 2009.

[Bradshaw and Pankhurst, 1964] P. Bradshaw and R. Pankhurst, "The Design of Low–Speed Wind Tunnels," *Progress in Aerospace Sciences*, 5:1–69, 1964.

[Brandt, 2014] L. Brandt, "The Lift–up Effect: The Linear Mechanism behind Transition and Turbulence in Shear Flows," *Eur. J. Mech. - BFluids*, 47:80–96, 2014.

[Brunton and Noack, 2015] S. L. Brunton and B. R. Noack, "Closed–Loop Turbulence Control: Progress and Challenges," *Appl. Mech. Rev.*, 67(5):050801, 2015.

[Burger *et al.*, 1982] E. Burger, W. Munk, and H. Wahl, "Flow Increase in the Trans Alaska Pipeline Through Use of a Polymeric Drag–Reducing Additive," *J. Pet. Technol.*, 34(02):377–386, 1982.

[Bürk *et al.*, 2012] J. Bürk, P. Blanke, Z. Stankovic, A. Barker, M. Russe, J. Geiger, A. Frydrychowicz, M. Langer, and M. Markl, "Evaluation of 3D Blood Flow Patterns and Wall Shear Stress in the Normal and Dilated Thoracic Aorta Using Flow–Sensitive 4D CMR," *J Cardiovasc Magn Reson*, 14(1):84, 2012.

[Butler and Farrell, 1993] K. M. Butler and B. F. Farrell, "Optimal Perturbations and Streak Spacing in Wall–Bounded Turbulent Shear Flow," *Phys. Fluids Fluid Dyn. 1989-1993*, 5(3):774–777, 1993.

[Campolo *et al.*, 2015] M. Campolo, M. Simeoni, R. Lapasin, and A. Soldati, "Turbulent Drag Reduction by Biopolymers in Large Scale Pipes," *J. Fluids Eng.*, 137(4):041102, 2015.

[Choueiri *et al.*, 2017] G. H. Choueiri, J. M. Lopez, and B. Hof, "Exceeding the Asymptotic Limit of Polymer Drag Reduction," arXiv:1703.06271v2 [physics.flu-dyn], 2017.

[Choueiri *et al.*, 2018] G. H. Choueiri, J. M. Lopez, and B. Hof, "Exceeding the

158

Asymptotic Limit of Polymer Drag Reduction," *Phys. Rev. Lett.*, 120(12):124501, 2018.

[Corbett and Bottaro, 2000] P. Corbett and A. Bottaro, "Optimal Perturbations for Boundary Layers Subject to Stream–Wise Pressure Gradient," *Phys. Fluids*, 12(1):120–130, 2000.

[Daniello et al., 2009] R. J. Daniello, N. E. Waterhouse, and J. P. Rothstein, "Drag Reduction in Turbulent Flows over Superhydrophobic Surfaces," *Phys. Fluids*, 21(8):085103, 2009.

[Davies et al., 1986] P. F. Davies, A. Remuzzi, E. J. Gordon, C. F. Dewey, and M. A. Gimbrone, "Turbulent Fluid Shear Stress Induces Vascular Endothelial Cell Turnover in Vitro.," *Proc. Natl Acad. Sci. USA*, 83(7):2114–2117, 1986.

[Davies, 2009] P. F. Davies, "Hemodynamic Shear Stress and the Endothelium in Cardiovascular Pathophysiology," *Nat. Clin. Pract. Cardiovasc. Med.*, 6(1):16–26, 2009.

[Dean and Bhushan, 2010] B. Dean and B. Bhushan, "Shark–Skin Surfaces for Fluid-Drag Reduction in Turbulent Flow: A Review," *Philos. Trans. R. Soc. Math. Phys. Eng. Sci.*, 368(1929):4775–4806, 2010.

[del Álamo and Jiménez, 2006] J. C. del Álamo and J. Jiménez, "Linear Energy Amplification in Turbulent Channels," *J. Fluid Mech.*, 559:205–213, 2006.

[DePaola et al., 1992] N. DePaola, M. A. Gimbrone, P. F. Davies, and C. F. Dewey, "Vascular Endothelium Responds to Fluid Shear Stress Gradients.," *Arterioscler. Thromb. J. Vasc. Biol.*, 12(11):1254–1257, 1992.

[Doherty et al., 2007] J. Doherty, P. Ngan, J. Monty, and M. Chong, "The Development of Turbulent Pipe Flow," In *16th Australasian Fluid Mechanics Conference (AFMC)*, pages 266–270. School of Engineering, The University of Queensland, 2007.

[Drazin and Reid, 2004] P. G. Drazin and W. H. Reid, *Hydrodynamic Stability*, Cambridge University Press, Cambridge, 2nd edition, 2004.

[Du and Karniadakis, 2000] Y. Du and G. E. Karniadakis, "Suppressing Wall Turbulence by Means of a Transverse Traveling Wave," *Science*, 288(5469):1230–1234, 2000.

[Durst *et al.*, 2005] F. Durst, S. Ray, B. Ünsal, and O. A. Bayoumi, "The Development Lengths of Laminar Pipe and Channel Flows," *J. Fluids Eng.*, 127(6):1154–1160, 2005.

[Durst and Ünsal, 2006] F. Durst and B. Ünsal, "Forced Laminar–to–Turbulent Transition of Pipe Flows," *J. Fluid Mech.*, 560:449–464, 2006.

[Eggels *et al.*, 1994] J. G. M. Eggels, F. Unger, M. H. Weiss, J. Westerweel, R. J. Adrian, R. Friedrich, and F. T. M. Nieuwstadt, "Fully Developed Turbulent Pipe Flow: A Comparison between Direct Numerical Simulation and Experiment," *J. Fluid Mech.*, 268:175–210, 1994.

[Ellingsen and Palm, 1975] T. Ellingsen and E. Palm, "Stability of Linear Flow," *Phys. Fluids*, 18(4):487–488, 1975.

[Farell and Youssef, 1996] C. Farell and S. Youssef, "Experiments on Turbulence Management Using Screens and Honeycombs," *J. Fluids Eng.*, 118(1):26–32, 1996.

[Fransson and Alfredsson, 2003] J. H. M. Fransson and P. H. Alfredsson, "On the Disturbance Growth in an Asymptotic Suction Boundary Layer," *J. Fluid Mech.*, 482:51–90, 2003.

[Fransson *et al.*, 2006] J. H. M. Fransson, A. Talamelli, L. Brandt, and C. Cossu, "Delaying Transition to Turbulence by a Passive Mechanism," *Phys. Rev. Lett.*, 96(6):064501, 2006.

[Frenning, 2001] L. Frenning, *Pump Life Cycle Costs: A Guide to LCC Analysis for Pumping Systems*, Hydraulic Institute, 2001.

[Frohnapfel *et al.*, 2007] B. Frohnapfel, J. Jovanović, and A. Delgado, "Experimental Investigations of Turbulent Drag Reduction by Surface–Embedded Grooves," *J. Fluid Mech.*, 590:107–116, 2007.

[Fukagata *et al.*, 2002] K. Fukagata, K. Iwamoto, and N. Kasagi, "Contribution of Reynolds Stress Distribution to the Skin Friction in Wall–Bounded Flows," *Phys. Fluids*, 14(11):L73–L76, 2002.

[Fukagata *et al.*, 2009] K. Fukagata, K. Sugiyama, and N. Kasagi, "On the Lower Bound of Net Driving Power in Controlled Duct Flows," *Phys. Nonlinear Phenom.*, 238(13):1082–1086, 2009.

[Furuichi *et al.*, 2015] N. Furuichi, Y. Terao, Y. Wada, and Y. Tsuji, "Friction Factor and Mean Velocity Profile for Pipe Flow at High Reynolds Numbers," *Phys. Fluids*, 27(9):095108, 2015.

[Gad-el-Hak, 1994] M. Gad-el-Hak, "Interactive Control of Turbulent Boundary Layers – A Futuristic Overview," *AIAA Journal*, 32(9):1753–1765, 1994.

[Gad-el-Hak, 2000] M. Gad-el-Hak, *Flow Control: Passive, Active, and Reactive Flow Management*, Cambridge University Press, Cambridge, 2000.

[Garcia-Mayoral and Jiménez, 2011] R. Garcia-Mayoral and J. Jiménez, "Drag Reduction by Riblets," *Philos. Trans. R. Soc. Math. Phys. Eng. Sci.*, 369(1940):1412–1427, 2011.

[Geraldi *et al.*, 2017] N. R. Geraldi, L. E. Dodd, B. B. Xu, G. G. Wells, D. Wood, M. I. Newton, and G. McHale, "Drag Reduction Properties of Superhydrophobic Mesh Pipes," *Surf. Topogr.: Metrol. Prop.*, 5(3):034001, 2017.

[Gimbrone and García–Cardeña, 2016] M. A. Gimbrone and G. García–Cardeña, "Endothelial Cell Dysfunction and the Pathobiology of Atherosclerosis," *Circ. Res.*, 118(4):620–636, 2016.

[Gioia and Chakraborty, 2006] G. Gioia and P. Chakraborty, "Turbulent Friction in Rough Pipes and the Energy Spectrum of the Phenomenological Theory," *Phys. Rev. Lett.*, 96(4), 2006.

[Greenblatt and Moss, 1999] D. Greenblatt and E. A. Moss, "Pipe–Flow Relaminarization by Temporal Acceleration," *Phys. Fluids*, 11(11):3478–3481, 1999.

[Greenblatt and Moss, 2004] D. Greenblatt and E. A. Moss, "Rapid Temporal Acceleration of a Turbulent Pipe Flow," *J. Fluid Mech.*, 514:65–75, 2004.

[Groth and Johansson, 1988] J. Groth and A. V. Johansson, "Turbulence Reduction by Screens," *J. Fluid Mech.*, 197:139–155, 1988.

[Guala *et al.*, 2006] M. Guala, S. E. Hommema, and R. J. Adrian, "Large–Scale and Very–Large–Scale Motions in Turbulent Pipe Flow," *J. Fluid Mech.*, 554:521–542, 2006.

[Hamilton *et al.*, 1995] J. M. Hamilton, J. Kim, and F. Waleffe, "Regeneration Mechanisms of Near–Wall Turbulence Structures," *J. Fluid Mech.*, 287:317–348, 1995.

[He *et al.*, 2016a] K. He, M. Seddighi, and S. He, "DNS Study of a Pipe Flow Following a Step Increase in Flow Rate," *Int. J. Heat Fluid Flow*, 57:130–141, 2016.

[He *et al.*, 2011] S. He, C. Ariyaratne, and A. E. Vardy, "Wall Shear Stress in Accelerating Turbulent Pipe Flow," *J. Fluid Mech.*, 685:440–460, 2011.

[He *et al.*, 2016b] S. He, K. He, and M. Seddighi, "Laminarisation of Flow at Low Reynolds Number Due to Streamwise Body Force," *J. Fluid Mech.*, 809:31–71, 2016.

[He and Jackson, 2000] S. He and J. D. Jackson, "A Study of Turbulence under Conditions of Transient Flow in a Pipe," *J. Fluid Mech.*, 408:1–38, 2000.

[He and Seddighi, 2013] S. He and M. Seddighi, "Turbulence in Transient Channel Flow," *J. Fluid Mech.*, 715:60–102, 2013.

[He and Seddighi, 2015] S. He and M. Seddighi, "Transition of Transient Channel Flow after a Change in Reynolds Number," *J. Fluid Mech.*, 764:395–427, 2015.

[Hellsten, 2002] M. Hellsten, "Drag–Reducing Surfactants," *J. Surfactants Deterg.*, 5(1):65–70, 2002.

[Hœpffner and Fukagata, 2009] J. Hœpffner and K. Fukagata, "Pumping or Drag Reduction?," *J. Fluid Mech.*, 635:171–187, 2009.

162

[Hof *et al.*, 2010] B. Hof, A. de Lozar, M. Avila, X. Tu, and T. M. Schneider, "Eliminating Turbulence in Spatially Intermittent Flows," *Science*, 327(5972):1491–1494, 2010.

[Hof *et al.*, 2003] B. Hof, A. Juel, and T. Mullin, "Scaling of the Turbulence Transition Threshold in a Pipe," *Phys. Rev. Lett.*, 91(24):244502, 2003.

[Högberg *et al.*, 2003] M. Högberg, T. R. Bewley, and D. S. Henningson, "Relaminarization of Reτ=100 Turbulence Using Gain Scheduling and Linear State–Feedback Control," *Phys. Fluids*, 15(11):3572–3575, 2003.

[Hultmark *et al.*, 2012] M. Hultmark, M. Vallikivi, S. C. C. Bailey, and A. J. Smits, "Turbulent Pipe Flow at Extreme Reynolds Numbers," *Phys. Rev. Lett.*, 108(9), 2012.

[Hutchins and Marusic, 2007a] H. Hutchins and I. Marusic, "Large–Scale Influences in near–Wall Turbulence," *Philos. Trans. R. Soc. Math. Phys. Eng. Sci.*, 365(1852):647–664, 2007.

[Hutchins and Marusic, 2007b] N. Hutchins and I. Marusic, "Evidence of Very Long Meandering Features in the Logarithmic Region of Turbulent Boundary Layers," *J. Fluid Mech.*, 579:1–28, 2007.

[Ichimiya *et al.*, 1998] M. Ichimiya, I. Nakamura, and S. Yamashita, "Properties of a Relaminarizing Turbulent Boundary Layer under a Favorable Pressure Gradient," *Exp. Therm. Fluid Sci.*, 17(1-2):37–48, 1998.

[Jackson *et al.*, 1989] J. Jackson, M. Cotton, and B. Axcell, "Studies of Mixed Convection in Vertical Tubes," *Int. J. Heat Fluid Flow*, 10(1):2–15, 1989.

[Jiménez, 1994] J. Jiménez, "On the Structure and Control of near Wall Turbulence," *Physics of Fluids*, 6(2):944–953, 1994.

[Jiménez, 2013] J. Jiménez, "Near–Wall Turbulence," *Physics of Fluids*, 25(10):101302, 2013.

[Jiménez and Pinelli, 1999] J. Jiménez and A. Pinelli, "The Autonomous Cycle of Near–Wall Turbulence," *J. Fluid Mech.*, 389:335–359, 1999.

[Joseph and Tabeling, 2005] P. Joseph and P. Tabeling, "Direct Measurement of the Apparent Slip Length," *Phys. Rev. E*, 71(3):035303, 2005.

[Jovanović *et al.*, 2005] J. Jovanović, M. Pashtrapanska, B. Frohnapfel, F. Durst, J. Koskinen, and K. Koskinen, "On the Mechanism Responsible for Turbulent Drag Reduction by Dilute Addition of High Polymers: Theory, Experiments, Simulations, and Predictions," *J. Fluids Eng.*, 128(1):118–130, 2005.

[Jung *et al.*, 1992] W. J. Jung, N. Mangiavacchi, and R. Akhavan, "Suppression of Turbulence in Wall–Bounded Flows by High–Frequency Spanwise Oscillations," *Physics of Fluids A: Fluid Dynamics*, 4(8):1605–1607, 1992.

[Kármán, von, 1930] T. Kármán, von, "Mechanische Ähnlichkeit Und Turbulenz," *Nachrichten Von Ges. Wiss. Zu Gött. Math Phys Kl.*, pages 58–76, 1930.

[Karniadakis and Choi, 2003] G. Karniadakis and K.-S. Choi, "Mechanisms on Transverse Motions in Turbulent Wall Flows," *Annu. Rev. Fluid Mech.*, 35(1):45–62, 2003.

[Karnik and Tavoularis, 1987] U. Karnik and S. Tavoularis, "Generation and Manipulation of Uniform Shear with the Use of Screens," *Exp. Fluids*, 5(4):247–254, 1987.

[Kasagi *et al.*, 2009a] N. Kasagi, Y. Hasegawa, and K. Fukagata, "Toward Cost–Effective Control of Wall Turbulence for Skin Friction Drag Reduction," In B. Eckhardt, editor, *Advances in Turbulence XII*, volume 132, pages 189–200. Springer Berlin Heidelberg, Berlin, Heidelberg, 2009.

[Kasagi *et al.*, 2009b] N. Kasagi, Y. Suzuki, and K. Fukagata, "Microelectromechanical Systems–Based Feedback Control of Turbulence for Skin Friction Reduction," *Annu. Rev. Fluid Mech.*, 41(1):231–251, 2009.

[Kim and Bewley, 2007] J. Kim and T. R. Bewley, "A Linear Systems Approach to Flow Control," *Annu. Rev. Fluid Mech.*, 39(1):383–417, 2007.

[Kim *et al.*, 1987] J. Kim, P. Moin, and R. Moser, "Turbulence Statistics in Fully Developed Channel Flow at Low Reynolds Number," *J. Fluid Mech.*, 177:133–166, 1987.

[Kim and Adrian, 1999] K. C. Kim and R. J. Adrian, "Very Large–Scale Motion in the Outer Layer," *Phys. Fluids*, 11(2):417–422, 1999.

[Kline *et al.*, 1967] S. J. Kline, W. C. Reynolds, F. A. Schraub, and P. W. Runstadler, "The Structure of Turbulent Boundary Layers," *J. Fluid Mech.*, 30(4):741–773, 1967.

[Kotansky, 1966] D. R. Kotansky, "The Use of Honeycomb for Shear Flow Generation." *AIAA Journal*, 4(8):1490–1491, 1966.

[Kühnen *et al.*, 2015a] J. Kühnen, P. Braunshier, M. Schwegel, H. C. Kuhlmann, and B. Hof, "Subcritical versus Supercritical Transition to Turbulence in Curved Pipes," *J. Fluid Mech.*, 770:R3, 2015.

[Kühnen *et al.*, 2015b] J. Kühnen, P. Maier, and B. Hof, "Forced Relaminarisation in a Pipe," *Gallery Fluid Motion*, https://doi.org/10.1103/APS.DFD.2015.GFM.V0055, 2015.

[Kühnen *et al.*, 2017] J. Kühnen, M. Riedl, D. Scarselli, and B. Hof, "Like Cures like: How to Destroy Turbulence with Turbulence," *Gallery Fluid Motion*, https://doi.org/10.1103/APS.DFD.2017.GFM.V0013, 2017.

[Kühnen *et al.*, 2018a] J. Kühnen, D. Scarselli, and B. Hof, "Relaminarization of Pipe Flow by Means of 3D–Printed Shaped Honeycombs," arXiv:1809.07625v1 [physics.flu-dyn], 2018.

[Kühnen *et al.*, 2018b] J. Kühnen, D. Scarselli, M. Schaner, and B. Hof, "Relaminarization by Steady Modification of the Streamwise Velocity Profile in a Pipe," *Flow Turbul. Combust.*, 100(4):919–943, 2018.

[Kühnen *et al.*, 2018c] J. Kühnen, B. Song, D. Scarselli, N. B. Budanur, M. Riedl, A. P. Willis, M. Avila, and B. Hof, "Destabilizing Turbulence in Pipe Flow," *Nat. Phys.*, 14(4):386–390, 2018.

[Kulkarni *et al.*, 2011] V. Kulkarni, N. Sahoo, and S. D. Chavan, "Simulation of Honeycomb–Screen Combinations for Turbulence Management in a Subsonic Wind Tunnel," *J. Wind Eng. Ind. Aerodyn.*, 99(1):37–45, 2011.

[Landahl, 1980] M. T. Landahl, "A Note on an Algebraic Instability of Inviscid Parallel Shear Flows," *J. Fluid Mech.*, 98(2):243–251, 1980.

[Landahl, 1975] M. T. Landahl, "Wave Breakdown and Turbulence," *SIAM J. Appl. Math.*, 28(4):735–756, 1975.

[Launder, 1964] B. E. Launder, "Laminarization of the Turbulent Boundary Layer in a Severe Acceleration," *J. Appl. Mech.*, 31(4):707–708, 1964.

[Laws and Livesey, 1978] E. M. Laws and J. L. Livesey, "Flow Through Screens," *Annu. Rev. Fluid Mech.*, 10(1):247–266, 1978.

[Lee *et al.*, 2014] J. Lee, J. H. Lee, J.-I. Choi, and H. J. Sung, "Spatial Organization of Large– and Very–Large–Scale Motions in a Turbulent Channel Flow," *J. Fluid Mech.*, 749:818–840, 2014.

[Lefebvre and White, 1989] P. J. Lefebvre and F. M. White, "Experiments on Transition to Turbulence in a Constant–Acceleration Pipe Flow," *J. Fluids Eng.*, 111(4):428–432, 1989.

[Lieu *et al.*, 2010] B. K. Lieu, R. Moarref, and M. R. Jovanović, "Controlling the Onset of Turbulence by Streamwise Travelling Waves. Part 2. Direct Numerical Simulation," *J. Fluid Mech.*, 663:100–119, 2010.

[Liu *et al.*, 2007] R. Liu, D. S.-K. Ting, and M. David Checkel, "Constant Reynolds Number Turbulence Downstream of an Orificed Perforated Plate," *Exp. Therm. Fluid Sci.*, 31(8):897–908, 2007.

[Livesey and Laws, 1973] J. L. Livesey and E. M. Laws, "Simulation of Velocity Profiles by Shaped Gauze Screens.," *AIAA Journal*, 11(2):184–188, 1973.

[Lodahl *et al.*, 1998] C. R. Lodahl, B. M. Sumer, and J. Fredsøe, "Turbulent Combined Oscillatory Flow and Current in a Pipe," *J. Fluid Mech.*, 373:313–348, 1998.

[Loehrke and Nagib, 1976] R. I. Loehrke and H. M. Nagib, "Control of Free–Stream Turbulence by Means of Honeycombs: A Balance Between Suppression and Generation," *J. Fluids Eng.*, 98(3):342–351, 1976.

[Lopez *et al.*, 2019] J. M. Lopez, D. Feldmann, M. Rampp, A. Vela-Martin, L. Shi, and M. Avila, "nsCouette – A High–Performance Code for Direct Numerical Simulations of Turbulent Taylor–Couette Flow," arXiv:1908.00587v2 [physics.flu-dyn], 2019.

[Luchini, 2017] P. Luchini, "Universality of the Turbulent Velocity Profile," *Phys. Rev. Lett.*, 118(22), 2017.

[Lumley and McMahon, 1967] J. L. Lumley and J. F. McMahon, "Reducing Water Tunnel Turbulence by Means of a Honeycomb," *J. Basic Eng.*, 89(4):764, 1967.

[Lumley and Blossey, 1998] J. Lumley and P. Blossey, "Control of Turbulence," *Annu. Rev. Fluid Mech.*, 30(1):311–327, 1998.

[Manna *et al.*, 2012] M. Manna, A. Vacca, and R. Verzicco, "Pulsating Pipe Flow with Large–Amplitude Oscillations in the Very High Frequency Regime. Part 1. Time–Averaged Analysis," *J. Fluid Mech.*, 700:246–282, 2012.

[Mao and Hanratty, 1986] Z.-X. Mao and T. J. Hanratty, "Studies of the Wall Shear Stress in a Turbulent Pulsating Pipe Flow," *J. Fluid Mech.*, 170:545–564, 1986.

[Marensi *et al.*, 2019] E. Marensi, A. P. Willis, and R. R. Kerswell, "Stabilisation and Drag Reduction of Pipe Flows by Flattening the Base Profile," *J. Fluid Mech.*, 863:850–875, 2019.

[Mathur *et al.*, 2018] A. Mathur, S. Gorji, S. He, M. Seddighi, A. E. Vardy, T. O'Donoghue, and D. Pokrajac, "Temporal Acceleration of a Turbulent Channel Flow," *J. Fluid Mech.*, 835:471–490, 2018.

[Matisse and Gorman, 1984] P. Matisse and M. Gorman, "Neutrally Buoyant Anisotropic Particles for Flow Visualization," *Phys. Fluids*, 27(4):759–760, 1984.

[McKeon *et al.*, 2013] B. J. McKeon, A. S. Sharma, and I. Jacobi, "Experimental Manipulation of Wall Turbulence: A Systems Approach," *Phys. Fluids*, 25(3):031301, 2013.

[McKeon *et al.*, 2005] B. J. McKeon, M. V. Zagarola, and A. J. Smits, "A New Friction Factor Relationship for Fully Developed Pipe Flow," *J. Fluid Mech.*, 538:429–443, 2005.

[Meseguer and Trefethen, 2003] Á. Meseguer and L. Trefethen, "Linearized Pipe Flow to Reynolds Number 10 7," *J. Comput. Phys.*, 186(1):178–197, 2003.

[Mikhailova *et al.*, 1994] N. P. Mikhailova, E. U. Repik, and Y. P. Sosedko, "Optimal Control of Free–Stream Turbulence Intensity by Means of Honeycombs," *Fluid Dyn*, 29(3):429–437, 1994.

[Min *et al.*, 2006] T. Min, S. M. Kang, J. L. Speyer, and J. Kim, "Sustained Sub–Laminar Drag in a Fully Developed Channel Flow," *J. Fluid Mech.*, 558:309–318, 2006.

[Moarref and Jovanović, 2010] R. Moarref and M. R. Jovanović, "Controlling the Onset of Turbulence by Streamwise Travelling Waves. Part 1. Receptivity Analysis," *J. Fluid Mech.*, 663:70–99, 2010.

[Mochizuki and Nieuwstadt, 1996] S. Mochizuki and F. T. M. Nieuwstadt, "Reynolds–Number–Dependence of the Maximum in the Streamwise Velocity Fluctuations in Wall Turbulence," *Experiments in Fluids*, 21(3):218–226, 1996.

[Modi, 1997] V. Modi, "Moving Surface Boundary Layer Control: A Review," *J. Fluids Struct.*, 11(6):627–663, 1997.

[Mohanty and Asthana, 1979] A. K. Mohanty and S. B. L. Asthana, "Laminar Flow in the Entrance Region of a Smooth Pipe," *J. Fluid Mech.*, 90(03):433–447, 1979.

[Moin and Bewley, 1994] P. Moin and T. Bewley, "Feedback Control of Turbulence," *Appl. Mech. Rev.*, 47(6S):S3–S13, 1994.

[Monty et al., 2007] J. P. Monty, J. A. Stewart, R. C. Williams, and M. S. Chong, "Large–Scale Features in Turbulent Pipe and Channel Flows," *J. Fluid Mech.*, 589:147–156, 2007.

[Moretti and Kays, 1965] P. Moretti and W. Kays, "Heat Transfer to a Turbulent Boundary Layer with Varying Free-Stream Velocity and Varying Surface Temperature - an Experimental Study," *Int. J. Heat Mass Transf.*, 8(9):1187–1202, 1965.

[Mukund et al., 2006] R. Mukund, P. R. Viswanath, R. Narasimha, A. Prabhu, and J. D. Crouch, "Relaminarization in Highly Favourable Pressure Gradients on a Convex Surface," *J. Fluid Mech.*, 566:97–115, 2006.

[Mukund and Hof, 2018] V. Mukund and B. Hof, "The Critical Point of the Transition to Turbulence in Pipe Flow," *J. Fluid Mech.*, 839:76–94, 2018.

[Munshi et al., 1999] S. Munshi, V. Modi, and T. Yokomizo, "Fluid Dynamics of Flat Plates and Rectangular Prisms in the Presence of Moving Surface Boundary Layer Control," *J. Wind Eng. Ind. Aerodyn.*, 79(1-2):37–60, 1999.

[Nakanishi et al., 2012] R. Nakanishi, H. Mamori, and K. Fukagata, "Relaminarization of Turbulent Channel Flow Using Traveling Wave–like Wall Deformation," *Int. J. Heat Fluid Flow*, 35:152–159, 2012.

[Narasimha and Sreenivasan, 1973] R. Narasimha and K. R. Sreenivasan, "Relaminarization in Highly Accelerated Turbulent Boundary Layers," *J. Fluid Mech.*, 61(3):417–447, 1973.

[Narayanan, 1968] M. A. B. Narayanan, "An Experimental Study of Reverse Transition in Two–Dimensional Channel Flow," *J. Fluid Mech.*, 31(3):609–623, 1968.

[Neto *et al.*, 2005] C. Neto, D. R. Evans, E. Bonaccurso, H.-J. Butt, and V. S. J. Craig, "Boundary Slip in Newtonian Liquids: A Review of Experimental Studies," *Rep. Prog. Phys.*, 68(12):2859–2897, 2005.

[Nikuradse, 1933] J. Nikuradse, "Gesetzmäßigkeiten der turbulenten Strömung in glatten Rohren (Nachtrag)," *Forsch. Auf Dem Geb. Ingenieurwesens*, 4(1):44–44, 1933.

[Nishi *et al.*, 2008] M. Nishi, B. Ünsal, F. Durst, and G. Biswas, "Laminar–to–Turbulent Transition of Pipe Flows through Puffs and Slugs," *J. Fluid Mech.*, 614:425–446, 2008.

[Oshinowo and Kuhn, 2000] L. Oshinowo and D. C. S. Kuhn, "Turbulence Decay behind Expanded Metal Screens," *Can. J. Chem. Eng.*, 78(6):1032–1039, 2000.

[Ou and Rothstein, 2005] J. Ou and J. P. Rothstein, "Direct Velocity Measurements of the Flow Past Drag–Reducing Ultrahydrophobic Surfaces," *Phys. Fluids*, 17(10):103606, 2005.

[Park and Choi, 1999] J. Park and H. Choi, "Effects of Uniform Blowing or Suction from a Spanwise Slot on a Turbulent Boundary Layer Flow," *Phys. Fluids*, 11(10):3095–3105, 1999.

[Patel and Head, 1968] V. C. Patel and M. R. Head, "Reversion of Turbulent to Laminar Flow," *J. Fluid Mech.*, 34(02):371–392, 1968.

[Peet *et al.*, 2008] Y. Peet, P. Sagaut, and Y. Charron, "Turbulent Drag Reduction Using Sinusoidal Riblets with Triangular Cross–Section," *38th Fluid Dyn. Conf. Exhib.*, 2008.

[Pennell *et al.*, 1972] W. T. Pennell, E. R. G. Eckert, and E. M. Sparrow, "Laminarization of Turbulent Pipe Flow by Fluid Injection," *J. Fluid Mech.*, 52(3):451–464, 1972.

[Perlin *et al.*, 2016] M. Perlin, D. R. Dowling, and S. L. Ceccio, "Freeman Scholar

Review: Passive and Active Skin–Friction Drag Reduction in Turbulent Boundary Layers," *J. Fluids Eng.*, 138(9):091104, 2016.

[Pope, 2000] S. B. Pope, *Turbulent Flows*, Cambridge University Press, 2000.

[Prandtl, 1932] L. Prandtl, "Zur Turbulenten Strömung in Rohren Und Längs Platten," *Ergeb. Aerodyn Vers. Zu Gött.*, 4:18–29, 1932.

[Pujals *et al.*, 2009] G. Pujals, M. García–Villalba, C. Cossu, and S. Depardon, "A Note on Optimal Transient Growth in Turbulent Channel Flows," *Phys. Fluids*, 21(1):015109, 2009.

[Quadrio, 2011] M. Quadrio, "Drag Reduction in Turbulent Boundary Layers by In–Plane Wall Motion," *Philos. Trans. R. Soc. Math. Phys. Eng. Sci.*, 369(1940):1428–1442, 2011.

[Quadrio *et al.*, 2009] M. Quadrio, P. Ricco, and C. Viotti, "Streamwise–Travelling Waves of Spanwise Wall Velocity for Turbulent Drag Reduction," *J. Fluid Mech.*, 627:161, 2009.

[Rabin *et al.*, 2014] S. M. E. Rabin, C. P. Caulfield, and R. R. Kerswell, "Designing a More Nonlinearly Stable Laminar Flow via Boundary Manipulation," *J. Fluid Mech.*, 738:R1, 2014.

[Rathnasingham and Breuer, 2003] R. Rathnasingham and K. S. Breuer, "Active Control of Turbulent Boundary Layers," *J. Fluid Mech.*, 495:209–233, 2003.

[Roach, 1987] P. Roach, "The Generation of Nearly Isotropic Turbulence by Means of Grids," *International Journal of Heat and Fluid Flow*, 8(2):82–92, 1987.

[Rothstein, 2010] J. P. Rothstein, "Slip on Superhydrophobic Surfaces," *Annu. Rev. Fluid Mech.*, 42(1):89–109, 2010.

[Sajben *et al.*, 1975] M. Sajben, J. Kroutil, G. Hoffman, and A. Sedrick, "Generation of Velocity Profiles Using Screens of Nonuniform Solidity," *AIAA Journal*, 13(4):417–418, 1975.

[Saranadhi *et al.*, 2016] D. Saranadhi, D. Chen, J. A. Kleingartner, S. Srinivasan, R. E. Cohen, and G. H. McKinley, "Sustained Drag Reduction in a Turbulent Flow Using a Low–Temperature Leidenfrost Surface," *Sci. Adv.*, 2(10):e1600686, 2016.

[Scarselli *et al.*, 2019] D. Scarselli, J. Kühnen, and B. Hof, "Relaminarising Pipe Flow by Wall Movement," *J. Fluid Mech.*, 867:934–948, 2019.

[Schmid and Henningson, 2001] P. J. Schmid and D. S. Henningson, *Stability and Transition in Shear Flows*, volume 142 of *Applied Mathematical Sciences*, Springer New York, New York, NY, 2001.

[Selvam *et al.*, 2015] K. Selvam, J. Peixinho, and A. P. Willis, "Localised Turbulence in a Circular Pipe Flow with Gradual Expansion," *J. Fluid Mech.*, 771:R2, 2015.

[Sharma *et al.*, 2011] A. S. Sharma, J. F. Morrison, B. J. McKeon, D. J. N. Limebeer, W. H. Koberg, and S. J. Sherwin, "Relaminarisation of $Re\tau = 100$ Channel Flow with Globally Stabilising Linear Feedback Control," *Phys. Fluids*, 23(12):125105, 2011.

[Shi *et al.*, 2015] L. Shi, M. Rampp, B. Hof, and M. Avila, "A Hybrid MPI–OpenMP Parallel Implementation for Pseudospectral Simulations with Application to Taylor–Couette Flow," *Comput. Fluids*, 106:1 – 11, 2015.

[Sibulkin, 1962] M. Sibulkin, "Transition from Turbulent to Laminar Pipe Flow," *Phys. Fluids*, 5(3):280, 1962.

[Sirovich and Karlsson, 1997] L. Sirovich and S. Karlsson, "Turbulent Drag Reduction by Passive Mechanisms," *Nature*, 388(6644):753–755, 1997.

[Smits *et al.*, 2011] A. J. Smits, B. J. McKeon, and I. Marusic, "High–Reynolds Number Wall Turbulence," *Annu. Rev. Fluid Mech.*, 43(1):353–375, 2011.

[Song *et al.*, 2017] B. Song, D. Barkley, B. Hof, and M. Avila, "Speed and Structure of Turbulent Fronts in Pipe Flow," *J. Fluid Mech.*, 813:1045–1059, 2017.

[Spalart, 1986] P. R. Spalart, "Numerical Study of Sink–Flow Boundary Layers," *J. Fluid Mech.*, 172:307–328, 1986.

[Sreenivasan, 1982] K. R. Sreenivasan, "Laminarescent, Relaminarizing and Retransitional Flows," *Acta Mech.*, 44(1-2):1–48, 1982.

[Sreenivasan and Strykowski, 1983] K. R. Sreenivasan and P. J. Strykowski, "Stabilization Effects in Flow through Helically Coiled Pipes," *Exp. Fluids*, 1(1):31–36, 1983.

[Steiner, 1971] A. Steiner, "On the Reverse Transition of a Turbulent Flow under the Action of Buoyancy Forces," *J. Fluid Mech.*, 47(3):503–512, 1971.

[Sumitani and Kasagi, 1995] Y. Sumitani and N. Kasagi, "Direct Numerical Simulation of Turbulent Transport with Uniform Wall Injection and Suction," *AIAA Journal*, 33(7):1220–1228, 1995.

[Swanson *et al.*, 2002] C. J. Swanson, B. Julian, G. G. Ihas, and R. J. Donnelly, "Pipe Flow Measurements over a Wide Range of Reynolds Numbers Using Liquid Helium and Various Gases," *J. Fluid Mech.*, 461:51–60, 2002.

[Tomiyama and Fukagata, 2013] N. Tomiyama and K. Fukagata, "Direct Numerical Simulation of Drag Reduction in a Turbulent Channel Flow Using Spanwise Traveling Wave–like Wall Deformation," *Phys. Fluids*, 25(10):105115, 2013.

[Tran *et al.*, 2010] T. Tran, P. Chakraborty, N. Guttenberg, A. Prescott, H. Kellay, W. Goldburg, N. Goldenfeld, and G. Gioia, "Macroscopic Effects of the Spectral Structure in Turbulent Flows," *Nat. Phys.*, 6:438–441, 2010.

[Trefethen *et al.*, 1993] L. N. Trefethen, A. E. Trefethen, S. C. Reddy, and T. A. Driscoll, "Hydrodynamic Stability Without Eigenvalues," *Science*, 261(5121):578–584, 1993.

[Valente and Vassilicos, 2011] P. C. Valente and J. C. Vassilicos, "The Decay of Turbulence Generated by a Class of Multiscale Grids," *J. Fluid Mech.*, 687:300–340, 2011.

[van Doorne and Westerweel, 2007] C. W. H. van Doorne and J. Westerweel, "Measurement of Laminar, Transitional and Turbulent Pipe Flow Using Stereoscopic-PIV," *Exp. Fluids*, 42(2):259–279, 2007.

[Vassilicos, 2015] J. C. Vassilicos, "Dissipation in Turbulent Flows," *Annu. Rev. Fluid Mech.*, 47(1):95–114, 2015.

[Virk *et al.*, 1970] P. S. Virk, H. S. Mickley, and K. A. Smith, "The Ultimate Asymptote and Mean Flow Structure in Toms' Phenomenon," *J. Appl. Mech.*, 37(2):488–493, 1970.

[Vukoslavcevic *et al.*, 1992] P. Vukoslavcevic, J. M. Wallace, and J.-L. Balint, "Viscous Drag Reduction Using Streamwise–Aligned Riblets," *AIAA Journal*, 30(4):1119–1122, 1992.

[Waleffe, 1997] F. Waleffe, "On a Self–Sustaining Process in Shear Flows," *Phys. Fluids*, 9(4):883–900, 1997.

[Walsh, 1983] M. J. Walsh, "Riblets as a Viscous Drag Reduction Technique," *AIAA Journal*, 21(4):485–486, 1983.

[Warnack and Fernholz, 1998] D. Warnack and H. H. Fernholz, "The Effects of a Favourable Pressure Gradient and of the Reynolds Number on an Incompressible Axisymmetric Turbulent Boundary Layer. Part 2. The Boundary Layer with Relaminarization," *J. Fluid Mech.*, 359:357–381, 1998.

[Watanabe *et al.*, 1999] K. Watanabe, Y. Udagawa, and H. Udagawa, "Drag Reduction of Newtonian Fluid in a Circular Pipe with a Highly Water–Repellent Wall," *J. Fluid Mech.*, 381:225–238, 1999.

[White and Mungal, 2008] C. M. White and M. G. Mungal, "Mechanics and Prediction of Turbulent Drag Reduction with Polymer Additives," *Annu. Rev. Fluid Mech.*, 40(1):235–256, 2008.

[Willis, 2017] A. P. Willis, "The Openpipeflow Navier–Stokes Solver," *SoftwareX*, 6:124–127, 2017.

[Willis *et al.*, 2010] A. P. Willis, Y. Hwang, and C. Cossu, "Optimally Amplified Large–Scale Streaks and Drag Reduction in Turbulent Pipe Flow," *Phys. Rev. E*, 82(3), 2010.

[Willis and Kerswell, 2009] A. P. Willis and R. R. Kerswell, "Turbulent Dynamics of Pipe Flow Captured in a Reduced Model: Puff Relaminarization and Localized 'Edge' States," *J. Fluid Mech.*, 619:213–233, 2009.

[Wygnanski and Champagne, 1973] I. J. Wygnanski and F. H. Champagne, "On Transition in a Pipe. Part 1. The Origin of Puffs and Slugs and the Flow in a Turbulent Slug," *J. Fluid Mech.*, 59(02):281–335, 1973.

[Yakhot *et al.*, 2010] V. Yakhot, S. C. C. Bailey, and A. J. Smits, "Scaling of Global Properties of Turbulence and Skin Friction in Pipe and Channel Flows," *J. Fluid Mech.*, 652:65–73, 2010.

[Yao *et al.*, 2011] X. Yao, Y. Song, and L. Jiang, "Applications of Bio–Inspired Special Wettable Surfaces," *Adv. Mater.*, 23(6):719–734, 2011.

[Zagarola and Smits, 1998] M. V. Zagarola and A. J. Smits, "Mean–Flow Scaling of Turbulent Pipe Flow," *J. Fluid Mech.*, 373:33–79, 1998.

[Zakin *et al.*, 1998] J. L. Zakin, B. Lu, and H.-W. Bewersdorff, "Surfactant Drag Reduction," *Rev. Chem. Eng.*, 14(4-5), 1998.